Engineering Graphene Oxide Electrolyte Membranes for Electrochemical Energy Systems

by

Serubbabel Sy

A thesis

presented to the University of Waterloo

In fulfillment of the

thesis requirement for the degree of

Doctor of Philosophy

in

Chemical Engineering

Waterloo, Ontario, Canada, 2021

Examining Committee Membership

The following professors served on the Examining committee for this thesis. The decision of the Examining Committee is by majority vote.

External Examiner	Dr. Guoliang (Greg) Liu Associate Professor, Chemistry Virginia Tech, VA, USA
Supervisor	Prof. Aiping Yu Professor, Chemical Engineering
Internal Members	Prof. Ali Elkamel Professor, Chemical Engineering
	Prof. Jeff Gostick Assoc. Professor, Chemical Engineering
Internal-External Member	Prof. Xiaosong Wang Professor, Chemistry

AUTHOR'S DECLARATION

This thesis consists of material of which I authored or co-authored: See Statement of Contributions included in the thesis. This a true copy of the thesis, including any required final revisions, as accepted by my examiners.

I understand that my thesis may be made electronically available to the public

Statement of Contributions

The body of this thesis is based upon a combination of published and unpublished works. Two chapters were reprinted from the journal paper in adjusted format. The reference to the paper (where applicable) is provided within the related chapters.

Chapter 4 is based on the published work by Zarrin *et al.* entitled “Molecular Functionalization of Graphene Oxide for Next-generation Wearable Electronics” in ACS Applied Materials & Interfaces (2016), 8, 38, 25428-37, and is produced with permission from the American Chemical Society. The thesis author’s specific contributions to this paper were to synthesize the composite electrolyte membranes, conduct the electrochemical impedance spectroscopy measurements, run portions of the physicochemical characterizations including scanning electron microscopy and energy dispersive X-ray spectroscopy, designed and analyzed the data for the supercapacitor application, prepare the final plots, results and write the initial manuscript. Dr. J Fu designed, conducted the experiments and analyzed the data concerning the Zn-air battery application. Mr. K Kang conducted the water contact angle measurements. Dr. YS Jun carried-out the measurements for the mechanical properties. Dr. G Jiang offered advice and insight throughout the process. Dr. H Zarrin aided with the main idea development and performed most of the physicochemical characterization tests. Dr. A Yu, Dr. M Fowler, and Dr. Z Chen supervised the project.

Chapter 5 is based on the published work by Sy *et al.* entitled “Near-Isotropic Proton-Conducting Porous Graphene Oxide Membrane” in ACS Nano (2020), 14, 11, 14947-14959, and is produced with permission from the American Chemical Society. The thesis author’s specific contributions to this paper were to synthesize the proton electrolyte membranes (PEM), conduct the EIS measurements, prepare and analyze all the physicochemical characterizations, prepare all the plots and results, write the final manuscript and respond to the comments of the reviewers. Dr. J. Zhang conducted additional conductivity measurements and provided the associated analysis. Mr. T. Cumberland conducted the alcohol fuel cell sensor testing, Mr. E. Bell carried out and provided us with the dynamic adsorption isotherm data. Dr. G Jiang, Dr. H. Zarrin and Dr. S Abureden offered advice on the process. Dr. A. Yu and Dr. Z. Chen supervised the project.

Chapter 6 is based on an unpublished work by Sy *et al.* The thesis author's specific contributions to this work were to synthesize and fabricate the composite PEMs, conduct EIS measurements, run all of the physicochemical characterizations, prepare all the figures and results, and write the final manuscript. Dr. G Jiang offered advice on the process. The work and manuscript publication were advised by the co-authors on this publication. Mr. T Cumberland conducted the alcohol fuel cell sensor testing. Dr. A. Yu and Dr. Z Chen supervised the project.

Abstract

Graphene oxide (GO) is an atomically-thick, two-dimensional nanomaterial decorated with an abundance of oxygen functional materials on the basal plane and edges. Due to its unique set of properties, it is a material used in many applications including sensors, energy storage and conversion devices, healthcare, optics, *etc.* The tendency to easily self-assemble into large-area, thin-film membranes and to host a defect-rich surface filled with oxygen-containing functional groups, makes GO an excellent membrane candidate material for facile coordination with other materials and molecules. However, in many electrochemical systems, GO membranes lack sufficient ionic conductivity to substitute the current, state-of-the-art perfluorosulfonic acid membranes. Significant efforts have been invested in expanding the unique combination of traits that GO has to offer as a new generation of electrolyte membrane material.

The primary objective of this project was to develop highly efficient, environmentally benign electrolyte membranes for electrochemical devices based on GO. To accomplish this, two different approaches were effectively implemented: (i) the development of a facile, environmentally benign, and scalable method of incrementally enhancing the through-plane proton conductivity of any GO-type membranes that utilizes GO as the base; and (ii) the complementary development of efficient and high performance GO membranes through functionalization. The properties of these new materials were investigated through (i) various physicochemical and electrochemical characterizations; and (ii) the validation of its pragmatic feasibility by prototyping the GO membranes in various electrochemical devices.

The hydroxide-ion conductivity of GO membranes was improved to serviceable levels by functionalizing GO with an ionic liquid, 1-hexyl-3-methylimidazolium (HMIM). HMIM itself possesses considerable ionic conductivity with minimal dependencies on temperature and humid media. Furthermore, HMIM strengthened the mechanical and chemical stability of GO membranes enabling operation in alkaline pHs. To confirm the commercial viability in wearable devices, model supercapacitors and Zn-air batteries were constructed with the HMIM-GO membranes demonstrating improved conductivities and lesser environmental dependencies than commercial membranes.

The through-plane proton conductivity and isotropy of the GO membrane was selectively enhanced by exploiting sonication-assisted (SA)-Fenton's reaction to generate a porous morphology in GO nanosheets. The resulting porous graphene oxide (pGO) was the first

reported near-isotropic proton conducting GO membrane with significant improvements in the through-plane conductivity over GO. Although pGO membranes offer an incremental improvement to GO membranes, they have demonstrated that the proton conductivity remains low due to the basis of their pristine nature. The feasibility of functionalization was evaluated with a plant extract called phytic acid (PA). PA was homogenously distributed throughout the GO membrane anchoring phytate groups onto the surface of the GO nanosheets. PA also removed and deactivated residual metal ions left by previous processes. The functional groups introduced to the material significantly boosted the proton conductivity of the GO membranes. In latter two projects, prototype alcohol fuel cell sensors equipped with all the aforementioned GO-based membranes were developed on the basis of direct ethanol fuel cell principles, exhibiting excellent sensitivity, linearity and stability.

New GO electrolyte membranes were developed by tailoring the surface morphology or by functionalization. Multiple application prototypes equipped with the new electrolyte materials highlight the practicality of the next-generation development in green, high performance electrochemical devices.

Acknowledgements

First and foremost, I would like express my gratitude and appreciation for my supervisor, Prof. Aiping Yu, and collaborator, Prof. Zhongwei Chen, for their continual support and guidance. Both of whom were indispensable sources of knowledge, wisdom and resources that directed my PhD journey.

I would like to give special appreciation to Dr. Gaopeng Jiang, who mentored and taught me a significant amount of what I know now in the research of fuel cell membranes. I would also like to make special mention to Dr. Hadis Zarrin who also mentored me, especially at the beginning of my PhD. Moreover, I would also like to thank the many members (and now alumni) of my lab group who helped and shaped who I am today.

I would also like to acknowledge and thank the examining committee, including Prof. Jeff Gostick, Prof. Ali Elkamel, Prof. Xiaosong Wang and Prof. Guoliang Liu for their valuable feedback.

I would also like to acknowledge my dear wife whom I met in this journey and became my largest supporter thereafter. I would like to extend my heartfelt appreciation to my family and friends for their support, endurance and encouragement, especially through the more challenging times.

Finally, all thanks to the Great *I AM…*

Table of Contents

List of Figures

List of Tables

List of Abbreviations

AC: alternate current

AEM: anion exchange membrane

AFCS: alcohol fuel cell sensor

BAC: blood alcohol content

BWF: Breit-Wigner-Fano

CV: cyclic voltammetry

DDI: double-deionized

DSSC: dye-sensitized solar cell

DVS: dynamic vapor sorption

EASA: evaporation-assisted self-assembly

EDLC: electric double layer capacitor

EDX: energy dispersive x-ray spectroscopy

EIS: electrochemical impedance spectroscopy

EOR: ethanol oxidation reaction

EM: electrolyte membrane

ESCA: electron spectroscopy for chemical analysis

GCD: galvanostatic charge/discharge

GIC: graphite intercalation compound

GO: graphene oxide

FWHM: full width half maximum

FTIR: Fourier-transform infrared

HMIM: 1-hexyl-3-methylimidazolium chloride

HR-TEM: high resolution transmission electron microscopy

IEC: ion exchange capacity

IL: ionic liquid

IR: infrared

LiTFSI: Lithium bis(trifluoromethane-sulfonyl) imide

LSV: linear sweep voltammetry

MEA: membrane electrode assembly

MOF: metal organic framework

NMR: nuclear magnetic resonance

OER: oxygen evolution reaction

ORR: oxygen reduction reaction

PA: phytic acid

PAN: polyacrylonitrile

PASA: pressure-assisted self-assembly

PBI: polybenzimidazole

PEI: poyletherimide

PEMFC: polymer exchange membrane fuel cell

PFSA: perfluorosulfonic acid

PMABS: poly(sulphobetaine)

PTFE: polytetrafluoroethylene

SA: sonication assisted

SEM: scanning electron microscopy

SHE: standard hydrogen electrode

SPEEK: sulfonated poly-(ether ether ketone)

RH: relative humidity

TEM: transmission electron microscopy

TGA: thermal gravimetric analysis

VASA: vacuum-assisted self-assembly

WU: water uptake

XRD: x-ray diffraction

XPS: x-ray photoelectron spectroscopy

ZC: zwitterion-coated

Chapter 1: Introduction

1.1 Challenges and Motivation

By 2050, the world energy usage will increase by 50% from 2019 due to worldwide technological advancement and industrial development.[1] There is an imperative commercial need to leverage alternative energy sources in order to prevent global energy exhaustion. Based on the report from US-EIA, fossil fuels is currently the predominant energy source used globally, whereas renewable energy usage is predicted to surpass all other energy sources by 2050.[1] Tremendous efforts have been invested towards the development of alternative energy storage and conversion systems to capitalize on the increasing renewable energy sources. The development for high performance, yet environmentally friendly and low cost, energy storage and conversion systems is among the most explored research areas around the globe.

The primary approaches to replace traditional energy resources involve fuel cells, batteries, and supercapacitors. Among these seemingly different systems, a commonality lies in their constitution, *i.e.* at the basic level, they're primarily comprised of an electrolyte and separator sandwiched between two electrodes. Customarily, electrochemical reactions transpire at one electrode releasing electrons and generating ions. Subsequently, the electrons travel through the external circuit and an external load, while the ions simultaneously traverse through the electrolyte to complete the reaction at the other electrode. Both the electrode and electrolyte play critical roles in determining the performance of the electrochemical system. Despite the equitable relevance of each component, the amount of research devoted to membrane development is comparatively lacking compared to that of electrode development. A redesign and constant improvement of electrolytes and electrolyte materials are needed in order to match the ever evolving electrodes that are used for energy conversion and storage devices.

The attributes of the electrolyte greatly influences many characteristics of the electrochemical system as a whole, including internal resistance, operational temperature, current response, *etc.* For example, in chemical gas sensors, the ionic conductivity influences the current response, which in turns, affects the detection limits, speed and sensitivity. Apart from the property of the current response, the temperature at which membranes can operate dictates whether the potentially faster response and recovery times can be achieved at lower temperatures and thereby lower the power requirements that would otherwise be needed to maintain the higher temperature.[2] Practically, a higher operating temperature will presumably

require a complementary heating unit to preserve the sensor temperature. The electrolyte membrane should ideally possess properties such as high ionic conductivity at room target temperature, selective permeability, and sufficient chemical, mechanical and thermal stability.

As materials are continuously being redefined in electrolyte membranes, GO membranes have drawn a considerable attention due to their superior properties such as large surface area, mechanical stability, tunable electrical and optical properties, and impermeability towards most gases and liquids. The versatility of GO membranes results in its application in various energy storage conversion and storage devices (*e.g.* fuel cells, supercapacitors, batteries, flow-batteries, solar cells, and sensors), liquid/gas detection/separation, optics, *etc.* In many electrochemical systems, GO membranes have been incorporated into separators or solid-state electrolytes; the function of which is predominantly occupied by commercial ionic polymers, such as Nafion. GO membranes also come with specific undesirable properties; they primarily lack ionic conductivity, risk of aggregation and possess relatively weaker mechanical and thermal stability especially when compared to commercial, established membranes.

1.2 Thesis Objectives and Approaches

The primary objective of this thesis is to enhance the ionic conductivity of GO-based electrolyte membranes (EM) for the impending implementation into commercial energy conversion and storage devices. This process is accomplished by providing incremental advancements or adding alternative methods to augment GO's desirable characteristics. The secondary objective includes preserving, if not improving, the current thermal, mechanical, and chemical stability. To this extent, two different strategies are considered and executed: surface modification and functionalization of GO membranes.

1. Ionic Liquid (IL) Functionalization of GO Membranes

Certain functional groups can be anchored onto the GO surface to greatly enhance hydroxide-ion conduction. More specifically, an IL, 1-hexyl-3-methylimidazolium chloride (HMIM) molecules, was anchored onto the surface of GO *via* esterification reactions and electrostatic π-π stacking. This resulted in a superior hydroxide conductivity, intercalated, bulky HMIM groups to prevent GO aggregation, minimum performance dependency upon environmental conditions (humidity and temperature), and improved mechanical integrity.

Overall, this project demonstrated the possibility of (i) tailoring GO membrane *via* functionalization to significantly improve hydroxide conduction; (ii) a working prototype to highlight the potential in this GO-composite EM to perhaps replace commercial membranes in future hydroxide-based devices.

2. Further oxidation of GO, *via* sonication assisted (SA)-Fenton reaction, to produce near-isotropic porous graphene oxide (pGO) membranes

The initial goal entering this project was (i) to selectively enhance the through-plane proton conductivity (actual pragmatic flow of ions in devices), and thereby decrease anisotropy; (ii) to develop a facile and scalable method to prepare pGO membranes.

The search led to varying the duration of SA-Fenton reaction to control the rate of oxidation in GO. This procedure generated additional pores and enlarged the existing pores. As a result, compared to GO membranes, the through-plane conductivity was increased by faintly compromising on the in-plane conductivity, which also significantly decreased the degree of anisotropy. Secondly, based on various characterizations, we elucidated the pore-formation mechanism, as well as enhanced proton conductivity of pGO.

Overall, this project contributed to: (i) discovering a method of preparing pGO that is environmentally benign, facile, and scalable; (ii) elucidating the mechanism by which pGO is prepared and the fundamental reasons for improving through-plane conductivity; (iii) implementing the material into an alcohol fuel cell sensor as a proof-of-concept for future development. These contributions may at least serve as a complimentary technique to incrementally improve GO membrane technology.

3. Phytic acid (PA) Functionalization of pGO membranes

Specific functional groups can be attached to the surface of pGO to tailor GO's ability to enhance proton conduction. Phytic acid (PA) was anchored onto the surface of pGO *via* epoxide ring opening reactions and subsequent esterification reactions. This modification resulted in an electrolyte membrane that possesses superior proton conductivity, consisting of intercalated and bulky phytate groups to prevent GO aggregation, and having residual iron ions removed or deactivated.

Overall, this project contributed to: (i) discovering a method to functionalize pGO that continues to be environmentally friendly, facile and scalable; (ii) tailoring pGO (and GO) membrane *via* functionalization to significantly improve proton conduction; and (iii) affirming the practicality of this membrane in a prototyped alcohol fuel cell sensor.

1.3 Structure of Thesis

The thesis is organized in six chapters and is structured as follows. Chapter 1 introduces the readers to the motivation, challenges, objectives and scope of the thesis work. Chapter 2 provides a comprehensive review covering the background and alternative solutions in the literature related to the content in this thesis. Chapter 3 briefly summarizes the characterizations that help confirm the thesis work as well as present the key performance measurements that are utilized throughout the thesis. This chapter also includes the associated theories used to explain certain traits and characteristics of the material. The details are provided in chapters 4 to 6. Chapter 4 involves the ionic-liquid functionalization of GO for a hydroxide-conductive, solid-state electrolyte membrane that exhibits superior ionic conductivity and stability. Chapter 5 provides an in-depth information on the reformed strategy of preparing pGO *via* employing the SA-Fenton reaction on GO to enhance the porosity, surface groups and ultimately, the proton conductivity. Chapter 6 describes a synergistic combination achieved *via* functionalization pGO with phytic acid, which to a large extent, enhanced the proton conductivity. Chapter 7 contains the summary and conclusions of the thesis, as well as possible avenues for future development to capitalize on the improvements to existing technology that resulted from this research.

Chapter 2: Background and Literature Review

2.1 Graphene-Oxide and Membranes

2.1.1 Graphene Oxide (GO)

Graphene oxide (GO), the disordered and insulating analogue of graphene, has recently become one of the most active research fields, originally because of its potential as a precursor to graphene, but now, due to its multifarious properties and robust utility in many applications. GO is generally denoted as a single layer of graphite oxide, typically, prepared from oxidation with subsequent dispersion and exfoliation. GO is similar to graphene, but possessing a plethora of oxygen-containing functional groups and structural defects scattered throughout its basal plane and edges. These functional groups include epoxides, alcohols, ketones, carbonyls and carboxylic groups, all of which endow GO its specific properties. In addition, these functional groups disrupt the sp^2 bonding networks causing GO to be electrically insulating, which enables its use in many other applications. As an example, due to its enhanced electrical resistance (compared to graphite and graphene), it can be utilized as a separator/electrolyte, whereas its analogues would short the electric cell.

The first mention of what was described as graphene oxide can be found in Brodie's publication.[3] Brodie, after oxidation, noticed an increase in the overall mass.[3] He also noted that successive oxidation treatments increased the oxygen content; however, the oxygen content reached a plateau after 4 treatments. Unfortunately, he was mistaken in trying to find one discrete molecular formula for graphite and graphite oxide.

In reality, the exact model for GO has been under debate for many years, yet no conclusive model exists.[4] There is a large variability in the types and distribution of the oxygen functional groups depending on the various preparation processes. In general, Anton Lerf and Jacek Klinowski's model has been the most widely accepted model in the graphene oxide community. Lerf *et al.* characterized many GO samples by nuclear magnetic resonance (NMR) spectroscopy.[5]

GO has been widely used when fashioned into a membrane.[6] Apart from its utility as an electrolyte, its application has also been reported in water desalination,[7] filtration, and transport because GO has a very low permeability towards every fluid other than water vapor. It is also used in hydrogen separation,[8] proton exchange,[9] bacterial deactivation and removal,[10] and

many other fields. Although the molecular model remains inconclusive, the lack of molecular clarity has not prevented researchers from integrating it into various technologies; there are still many potential applications for GO.

GO, like graphene, has many favorable attributes. It is generally electronically insulating, but by manipulating the disorder, GO can be fashioned to be insulating, semiconducting or even semi-metallic.[11] GO has very selective permeation and is relatively easy to prepare and process as a membrane, making it a very strong candidate for gas/liquid filtration. As a membrane, it's very customizable: the pore size distribution, membrane thickness, interlayer spacing and surface functionalization can all be easily tweaked. GO also possesses unique optical properties, and a high surface area. One of the biggest advantages of using GO is that it can be processed from inexpensive natural graphite through liquid-phase exfoliation. Yet many challenges still exist for a full exploitation of this material.[11]

There is still a need to better understand the defects and its effects on conductivity and electron transport characteristics. GO is known to be metastable at room temperature due to loss of epoxy groups and gaining hydroxyl groups.[12] Consequently, much research is still needed to mature the design and construction of GO-based devices.

2.1.1.1 Preparation of GO

In the development of GO, early attempts focused on inserting chemical species between the basal planes. Shaffault was credited with successfully intercalating potassium into graphite.[13] Intercalation can expand the interlayer spacing up to 1 nm in graphite intercalation compounds (GICs). This expansion was due to the reduction in van der Waals forces, which eventually led other researchers to subsequently try chemical exfoliation. Shortly after, Brodie developed his method of exfoliating graphite in 1859.[14] He added potassium chlorate ($KClO_3$) to graphite slurry and fuming nitric acid (HNO_3). This process generated toxic gases and $KClO_3$ is very reactive, flammable and combustible. Three decades later, Staudenmaier improved on this method in 1898.[15] Instead of adding $KClO_3$ in one addition, Staudenmaier added $KClO_3$ in multiple aliquots to graphite over fuming HNO_3 and concentrated sulfuric acid (H_2SO_4).[16] This process was very time-consuming because it took over a week for the reaction to cool down; it was also dangerous due to ClO_2 evolution and the large amounts of combustible potassium chlorate that were used. In 1958, Hummer and Offeman built upon Brodie's and Staudenmaier's methods.[17] Hummer instead oxidized graphite using potassium permanganate ($KMnO_4$) with

sodium nitrate ($NaNO_3$) in concentrated sulfuric acid (H_2SO_4). Hummer reported having achieved similar levels of oxidation to that of Staudenmaier. The active species in this oxidation reaction is dimanganese heptoxide, Mn_2O_7, which is known to detonate when heated to temperatures greater than 55 ^oC or when placed in the presence of organic compounds. The advantage of this process was that the oxidation could be completed within two hours. Yet the Hummer process did not resolve the issue of releasing toxic gasses (NO_2 and N_2O_4).[16] Recently, Tour proposed an improved synthesis of GO.[16] In this work, $NaNO_3$ was replaced with phosphoric acid (H_3PO_4). In addition, aliquots of $KMnO_4$ was added to a 9:1 mixture of concentrated H_2SO_4:H_3PO_4. As a result of this improvement, the method mitigated the generation of toxic gasses, and produced higher yields.

Recently, other techniques of preparing GO had been discovered and were constantly undergoing development. These techniques were devised on the basis of optimizing either or a combination of the following criteria: quality (layers of graphene oxide per stack/platelet), yield, safety (human, environmental), potential for automation and scale-up, and cost. For example, recently Hatakeyama *et al.* published a new method of bubbling ozone into an aqueous solution containing graphite.[18] This method avoided the usage of concentrated acidic solutions, but not the generation of harmful gases.

Another method for preparing GO that had branched into its own research field was *via* the electrolytic method, which had been reported to have yields as promising as Hummer's method. The electrolytic method had drawn the attention of many researchers due to its ease in execution, safety and efficiency. The exfoliation was typically initiated by the intercalation of ions, followed by the expansion induced by gaseous products. More specifically a voltage bias was applied to induce hydrolysis and produce radicals.[19, 20] Subsequently, the radicals attacked the sp^2 carbon atoms located on defect sites and on the edges of the graphite electrode to generate hydroxyl groups. However, some of these hydroxyl groups on the basal plane oxidized into epoxy groups, while some of the hydroxyl and ketone groups found on the edges oxidized into carbonyl and carboxyl groups, respectively. The graphite exfoliation was attributed to the combination of water electrolysis, anionic intercalation and gas evolution.

The primary factors that affected the oxidation level of GO products were the pre-treatment of graphite electrodes, and the type of oxidative electrolytes used. The operational inputs, which include applied voltages, electrolyte temperature and mechanical forces also contributed to the properties of the resulting graphene-based materials. Each of these factors had developed their own paths of research for further exploration and optimization.

For example, the quality of exfoliation was found to depend on the number of ions that were intercalated during the electrode pre-treatment. The pre-treatment typically involved soaking in concentrated H_2SO_4, which enabled HSO_4^- [19, 21-23] (or sometimes H_3O^+ [24]) ions to intercalate. Other reports had shown that the oxidative electrolytes, such as H_2SO_4, $HClO_4$ or HNO_3, were used in the electrolytic method, wherein anions intercalated under certain potentials. The subsequent electrochemical decomposition of the anions produced various oxygen-containing radicals (HO· and O·). Other oxidizing precursors were also considered as electrolytes (*e.g.* Na_2WO_4, $NaNO_3$, and H_2O_2) for GO synthesis.[25, 26] In their findings, H_2O_2 introduced many defects to the graphene materials, while $NaNO_3$ produced very thick GO (~50nm), which suggested poor exfoliation.

In the optimization of the operational parameters, increasing exfoliation voltage was correlated with faster generation of HO· and O· radicals.[27-29] Another factor, exfoliation temperature, affected the rate of generating oxidative radicals and their efficiency towards graphite exfoliation.[30, 31] Complimentary mechanical forces (*e.g.* stirplate mixing) was found to facilitate graphite exfoliation.[32]

2.1.2 Porous Graphene Oxide (pGO)

GO inherently possessed very small nanopores, which enabled it to reject everything other than water vapor (including ethanol and gasses). Although several research efforts were spent on investigating porous graphene, there was very little research on strategies to enlarge the pores of GO for other applications. Porous GO (pGO) is basically GO that had been further oxidized. The processes to generate pGO are accomplished by introducing more pores, enlarging the pores, and/or introducing more oxygen-containing functional groups. The properties inherent to GO but absent in graphene, were typically enhanced, such as hydrophilicity, ionic conductivity, and electrical resistance.

Based upon generating more defects and oxygen-containing functional groups, pGO possessed higher surface areas, a greater hydrophilicity, which would relate to higher water absorption rates and enhanced proton mobility. Alternatively, more and larger pores translated to more pathways for ions to traverse through the membrane. The challenges of introducing more defects and oxygen functional groups also implied that the mechanical integrity and chemical stability of GO were compromised, depending on the degree of oxidation.

2.1.2.1 Preparation of pGO

There are limited reports on preparing pGO. A major challenge lies in the trait that GO can be easily reduced. For example, pGO preparation techniques must be carried out at low temperatures because deoxygenation of GO began at 150 ^{o}C. Han *et al.* reported having prepared porous graphene oxide *via* steam etching.[33] When steam-etching was carried out at 200 ^{o}C, a significant amount of oxygen functional groups were removed. Han concluded that the steam-etched GO was partially reduced. There was another report using UV irradiation under O_2.[34] The GO suspension was dried under vacuum then irradiated with mercury lamp in O_2 or N_2–filled environment. As a result, nanopores were produced in oxygenated group domains where CO_2 evolved through photo-oxidation and GO was photo-reduced. The only other report claiming to have synthesized pGO was *via* ozonation[9]. This process was accomplished by bubbling O_3 into GO solution for set intervals, which generated nanopores and increased the number of oxygen-containing functional groups on the graphene oxide, and was very favorable for increasing proton conductivity. Even though pGO was produced, these methods were difficult to scale up and dangerous to administer. On the basis of the above considerations, there is an industrial need for scalable and environmentally benign methods of producing porous graphene oxide.

2.1.3 Graphene Oxide Membranes

GO membranes are thin films of GO, which make great candidate materials to mold into membranes. Compared to graphite and graphene, GO membrane inherently possesses a low electrical conductivity, which is the primary requirement for separators.[35, 36]

The property which allowed GO to be applied as a 2D proton conductor is due to the various hydrophilic oxygen functional groups (*e.g.* hydroxyl, carboxyl, epoxy) covalently attached to each side of the GO sheet. These groups are able to form a continuous hydrogen-bonding network with water molecules from a humidified environment.[37, 38] In other words, the high ionic conductivities can be attributed to the hydrophilic oxygen groups and rapid translation through the hydrogen-bonding network formed by adsorbed water layer on the GO surface. As an example, the proton conductivity of GO sheets (single or bulk) were in the order of 10^{-3} – 10^{-2} S cm^{-1} at 95% RH, depending on the temperature at which the characterization was conducted.[39-45] These conductivities can potentially reach that of commercial conductors such as Nafion. Studies show that GO proton conductivities increased with film thickness (under

200nm thick).[45] This property was due to a multilayer stacking of GO nanosheets to form compact bundles of 2D proton conduction channels which further contributed to accelerating proton mobility and hydrogen bond breaking/reformation process.[45] Some researchers speculated that, based on the proton conductivity, GO membranes could provide better performance in acidic electrolytes than that of many polymer proton conductors.[46]

GO membrane research has been steadily developing in various electrolytes, filtration, and purification. A major benefit lies in its impermeability towards most gases, yet selectively permeable towards water. For example, water molecules permeate through GO membrane at least 10^{10} times faster than He atoms.[47]

2.1.3.1 Membrane Preparation and Attribute Tuning

Over the years, many techniques have been developed for preparing GO membranes and selectively tuning specific properties.[35] When tuning for specific properties, GO synthesis controls the chemical structure, whereas the fabrication method determines the physical structure. For example, Paneri *et al.* found that the methanol permeability was linearly related to the flake size, while proton conductivity did not depend on the physical structure because protons conducted through the functional groups rather than channels.[48] Lv *et al.* discovered that adjusting the pH controls the extent and nature of functional groups, physical size of membrane channels, and also optical properties.[49]

There are many methods that have been developed for preparing GO membranes, primarily revolving around self-assembly. The simplest variance of this self-assembly would be through “drop-cast”-ing GO solution.[50] This involves pouring a solution of GO onto a substrate (*i.e.* petri dish) then letting the solvent evaporate. Subsequently, the standalone membrane can be displaced from the substrate. Another variant of self-assembly is *via* Layer-by-Layer deposition.[51] This technique involves repeatedly dipping a substrate into a GO solution, then a cross-link-containing solution, alternating between the two solutions repeatedly. The number of thickness of the layer can be controlled depending on the number of immersions that were made. A group of self-assembly techniques that has become the most commonly used process for preparing GO membrane is utilizing filtration.[52] Within filtration, there are 3 common approaches:[53] pressure-assisted self-assembly (PASA), vacuum-assisted self-assembly (VASA) and evaporation-assisted self-assembly (EASA).

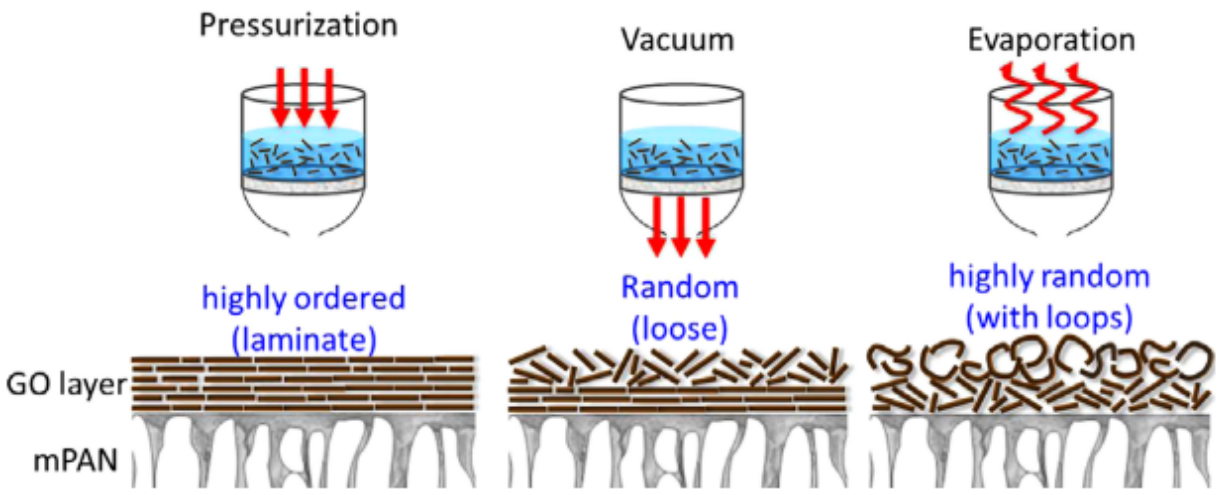

Figure 2-1. Schematic of GO/mPAN membranes preparation *via* (left) pressure-assisted self-assembly, (middle) vacuum-assisted self-assembly (VASA), (right) evaporation-assisted self-assembly (EASA) (reprinted from Ref[53] with permission from Elsevier).

A very recent approach of preparing GO membranes involves using nematic liquid crystals of GO to prepare GO-based nanofiltration membranes.[54] The GO solutions were initially concentrated with the aid of hydrogel beads to produce nematic phase GO liquid crystals, followed by casting on a doctor blade to orient into GO membranes. This newer technique offers better versatility in controlling the membrane architecture, and efficiency in forming membranes.

2.1.4 Graphene Oxide Composite Membranes

Practical GO-based membranes take the form of polymer/GO nanocomposites. Most of the studies in this field has essentially been screening for synergistic characteristics between GO and the complimenting polymer. As a result, possible combinations where GO fulfills the role as a base, filler and even a functionalized bridge between the mobile ion and base has been considered and explored quite thoroughly.

When considering GO as a grafting base, there are a wide variety of polymers with various chain structures that can be grafted, which allow for many possible combinations. For example, Shen *et al.* developed a thermal responsive composite *via* grafting poly(sulphobetaine) (PMABS) onto GO in order to prevent thermal runaway reactions in energy storage devices.[55] PMABS is an upper critical solution temperature polymer, which readily

attached to GO and functioned as an additive in non-aqueous electrolyte. The PMABS/GO-containing cell reversibly reduces specific storage capacity by >50% (compared to 30% without polymer modification) when operating beyond the “safe” temperature range. It also prevents reversible ion flow at elevated temperatures, whereas traditional means would irreversibly short the cell. In this study, GO provided the physical scaffold and functional groups that enable the covalent anchoring of PMABS. In another report, Zarrin *et al.* developed a hydroxide-conducting membrane by grafting an ionic liquid, hexyl-methyl imidazole (HMIM) onto GO.[56] HMIM was anchored onto GO by both covalent and non-covalent bonds that were induced by esterification reactions and electrostatic π-π stacking, respectively.

Despite several advancements made in utilizing GO as a grafting base, even more advancements were made in utilizing GO as a graft or filler. GO has many favorable properties that can enhance the base material, *e.g.* high hydrophilicity, which enables better water uptake and retention. The largest category of GO composite membranes, in terms of research and development, are GO/Polymer membranes. A plethora of polymers, which can be further subdivided into fluorinated (*e.g.* Nafion), and non-fluorinated (*e.g.* sulfonated poly-(ether ether ketones (SPEEK)), chitosan) have also been thoroughly explored.[57] Perfluorosulfonic acid membranes (*i.e.* Nafion) serve as the industry standard due to its high proton conductivity and excellent mechanical, thermal and chemical stability. Adding GO can raise the standard by augmenting both the side chains and backbone of Nafion, as well as the strong interfacial attraction that is formed. For example, Ansari *et al.* added GO into the Nafion polymer matrix and found significant changes in the ionic domains.[58] Zarrin *et al.* incorporated sulfonated GO into Nafion to improve selectivity and proton conductivity.[59] The result was an improvement in proton conductivities of up to 4 times over recast Nafion.

Non-fluorinated polymers that had been sulfonated or blended with mineral acids/inorganic precursors were also widely used due to its facile functionalization and excellent stability. One such example is SPEEK, which has been considered due to its thermal, chemical and mechanical stabilities.[57, 60] However, it does possess lower ionic conductivities when compared to Nafion, which can be mitigated by the incorporation of various fillers. Kumar *et al.* grafted sulfonated graphene oxide onto SPEEK for polymer electrolyte fuel cells.[61] In this report, the sulfonated GO enhanced the proton conductivity by interconnecting the proton transport channels between SPEEK sulfonic acid groups. As a result, the composite membrane demonstrated high proton conductivities at both low and high humidity. Another example is polyacrylonitrile (PAN), which has been studied due to its process efficiency and excellent

resistance to oxidative degradation. Zhu *et al.* discovered synergistic effects, including a highly porous structure and good wettability, which can be exploited when mixing PAN and GO as a separator in LiS batteries.[62]

One other major category of composites for grafting GO is incorporating it into metal organic frameworks (MOFs), which also has been heavily investigated.[56, 63, 64] MOF is a class of crystalline materials that contain metal ions that are held together by organic bridging ligands.[63] MOFs are attractive materials due to their large surface area, structure tenability and high porosity.[65-67] As an example of utilizing GO in MOFs, Bian *et al.* reported the use of GO as a stabilizer for an *n*-octanol and water emulsion system to promote the formation of MOF/GO *via* Pickering emulsion-induced growth. In this report, the presence of GO was reported to have enhanced the surface porosity, and water resistance.[68, 69] In another case, Castarlenas *et al.* utilized layer-by-layer assembly to prepare UiO-66-GO mixed matrix membranes. There was an improved selectivity and permeability for H_2 adsorption, which can be attributed to the exfoliation of GO and the addition of defects in the hybrid layers.[70]

In addition to utilizing GO as a grafting base or the graft itself, utilizing functionalized GO as a bridge between mobile ions and the base is very practical. More specifically, there are many polymers that would be rendered unusable in electrochemical systems due to its very low ionic conductivity. However, this lack can be compensated by introducing mobile ions into the polymer matrix. Here, GO *via* its surface functional groups can play dual roles of enabling a connection with the polymer, and providing mobile ions for the composite to facilitate ionic conductivity. For example, polybenzimidazole (PBI) has been formed into membranes due to its excellent thermal stability and good chemical stability, but has seen limited use in electrochemical applications due to its limited ionic conductivity.

In a recent report, Lin *et al.* challenged this notion by tethering an ionic liquid (IL) to GO (IL-GO), then dispersed it into another ionic liquid to enhance the conductivity in dye-sensitized solar cells (DSSCs).[71] IL-GO was prepared *via* epoxide ring-opening reaction between GO and 1-(3-aminopropyl)-3-methylimi-dazolium bromide (IL-NH_2), then an anion exchange was introduced with Lithium bis(trifluoromethane-sulfonyl) imide (LiTFSI). The result of adding 4 wt% IL-GO improved the overall power conversion efficiency to 7.04%, from 5.65% for that without IL-GO. IL-GO was found to have improved the diffusion coefficients of I_3^- which enabled an easier regeneration of the dye molecule; however, excess IL-GO increased the viscosity and hindered the ionic transfer. From the same group, Wan *et al.* prepared polybenzimidazole (PBI)/IL-functionalized GO (PBI/IL-GO) composite membrane for alkaline anion exchange

membrane (AEM) fuel cells.[29, 72] The addition of IL-GO significantly the increased water uptake, and maintained acceptable swelling degree and alkaline stability, which ultimately led to an improved ionic conductivity. Another example is a zwitterion-coated (ZC) GO containing both ammonium and sulfonic acid groups as proton-carrying additive for PBI-based PEMs.[73] The attached sulfonic acid groups contributed to an increased proton conductivity, while the dissociation of sulfonic acid was facilitated by the electrostatic attraction of quaternary ammonium groups. GO was mixed with poyletherimide (PEI) and 1-[3-(di-methylamine) propyl]-3-ethylcarbodiimide, then refluxed in DMSO with 1, 3-propanesultone, and dried to obtain ZC-GO. The PBI/ZC-GO composite membrane was prepared *via* mixing ZC-GO with PBI vigorously and casting onto a glass plate. ZC-GO possessed an extremely high surface area and large amounts of ammonium and sulfonic acid groups, which enabled higher water retention and proton conductivity rates. It also extended the number of available ion exchange sites per clusters, which enhanced the proton mobility of the membrane.

2.2 Fundamentals and Electrolytes in Energy Conversion and Storage Devices

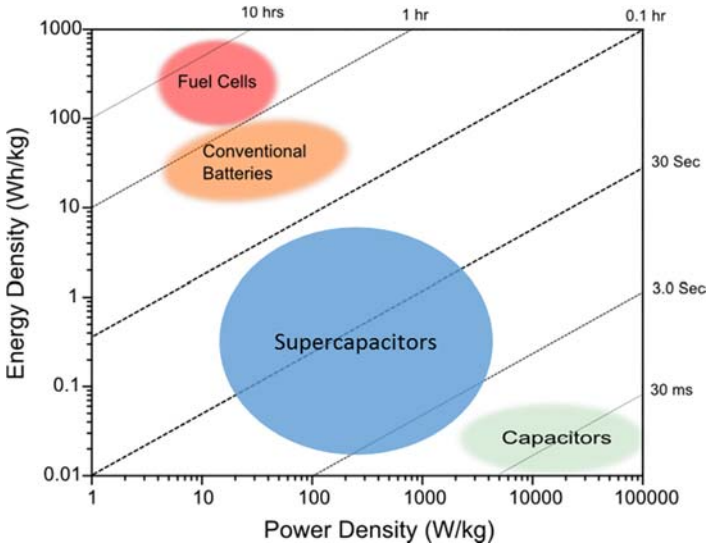

Figure 2-2. Simplified Ragone plot outlining the major types of energy conversion and storage devices and their relative performances

This section covers the background and operating principle of the energy conversion and storage devices for which the thesis work was prototyped on. **Figure 2-2** outlines the major categories within energy conversion and storage devices.

2.2.1 Polymer Exchange Membrane Fuel Cells (PEMFCs)

On one corner of the Ragone plot **(Figure 2-2)** lies the fuel cell, which possesses high energy densities but lacking in the power density (in comparison to the other categories of energy storage devices). Within the field of fuel cells, there are many different subtypes depending on the operating temperature and fuel used. Each subtype also has a plethora of research and development that had advanced each technology since the inception of fuel cells.

The scope of this section will be limited to PEMFCs, which operate at the lower temperature end of the fuel cell spectrum and utilize H_2 and air as its fuel. PEMFCs remain a very promising technology, possessing high electrical efficiencies (up to 60%) greater than that of internal combustion engines and conventional power plants. They produce very low emissions, wherein the only exhaust is unused air and water. With very high energy densities, as seen in **Figure 2-2**, they are simple in operation, low cost over the lifetime of the material, as well as no moving parts involved. Moreover PEMFCs are very modular; more power can be easily generated by running multiple cells in parallel; and less planning is necessary when compared to other sources, such as power plants. Unfortunately, the widespread commercial adaptation has yet to be realized because hydrogen is not readily available. Hydrogen generation will most likely generate emissions, but are lower than comparable conventional energy conversion technologies. Another major hindrance to wider usage is due to the cost, which is associated with the expensive materials needed to produce PEMFCs. Although electrocatalysts utilize precious metals, substitution and reduction of noble metals for this process are being explored. Another major component of the PEMFC is the PEM, which the current state-of-the-art electrolyte is based on perfluorosulfonic acid (PFSA) (commercially most common used polymer is Nafion®, which was developed by DuPont in 1960s).

The PEM can be considered the core of PEMFC. It must possess efficient proton conductivity, low fuel permeability, and high mechanical stability. Considering these characteristics, Nafion has been adopted as the industry standard. The Nafion backbone is comprised of polytetrafluoroethylene (PTFE, or also known as Teflon), which provides the structural support, while the sulfonic acid functional groups facilitate proton transport. The major

drawback of Nafion is that it is costly to produce due to the complex and toxic manufacturing process, swelling problems and fuel crossover.[74, 75] There has been a lot of efforts spent on finding new materials to replace Nafion. As a result, graphene oxide-based membranes were investigated.[8] Although GO membranes absorb more water than Nafion, the membrane also swells to a greater degree, which increases the risk of deterioration when hydrated. There have been progress in developing GO membranes for PEM, and also potential for improvement.

2.2.1.1 Principles of Operation

A PEMFC is primarily comprised of an electrolyte, anodic and cathodic electrodes containing catalyst (for electrochemical reactions), gas diffusion layers, bipolar and flow field plates. The key components can be summed up in a Membrane Electrode Assembly (MEA) which is comprised of only the PEM, anode and cathode. The setup consists of a negative electrode (anode) and a positive electrode (cathode) sandwiching the electrolyte.[76]

In the operation of a typical PEMFC, the fuel in the form of hydrogen is fed to the anode and air to the cathode. Each hydrogen atom is split at the electrode. The proton travels through membrane, while the electron travels to the current collectors, through the external load-containing circuit, then back to the other electrode on the other side of the membrane. The electrons then meet at a catalyst site with the proton, which travels through the electrolyte, and the oxygen, which was fed from the other side of the fuel cell. As for the by-products, water and heat are simultaneously produced in the electrochemical reaction and must be removed from the system to prevent performance issues.

The aforementioned electrochemical reactions are summarized in the following equations:

$$Anode: H_2 \rightarrow 2H^+ + 2e^- \quad \textbf{(2-1)}$$

$$Cathode: \frac{1}{2}O_2 + 2H^+ + 2e^- \rightarrow H_2O \quad \textbf{(2-2)}$$

2.2.2 Supercapacitors

On the other side of the Ragone plot lies the supercapacitors or sometimes referred to as electric double layer capacitors (EDLCs), which vaunts its high power densities, but is lacking

in its energy densities (compared to the other types of energy storage devices). Supercapacitors, also known as ultracapacitors, have garnered much attention since its initiation in 1957.[77]

Supercapacitors holds several advantages over conventional batteries and fuel cells. It possesses a high power density, shorter charging times, and a longer battery and shelf life. Unfortunately, it suffers from its low energy density, which has been progressively mitigated through much research over the years. Popular approaches include manipulating the electrode architecture to increasing the surface area, optimizing the electrode/electrolyte compatibility (*e.g.* adjusting surface functionality, pore structure/size, ion size), and increasing operational voltage (*e.g.* utilizing a non-aqueous electrolyte).

Due to the low energy densities, supercapacitors are uncommonly used as a sole, primary source of energy, but rather as a complimentary energy source. Thus far, it's been often implemented in conjunction with other energy sources that have higher energy densities, but lack the initial power. For example, supercapacitors are used in regenerative braking systems; it stores charge when the vehicle brakes, then releases it upon acceleration.[78] Moreover, it can be found in lifting operations, where bursts of power is needed,[79] transitional backup power systems, supplying energy when sources are being exchanged,[79] increasing energy grid stability, voltage stabilization in start/stop systems. Lastly, supercapacitors are starting to see more usage in consumer electronics: wearable and portable electronics,[80-82] and even as a primary power source in railcars.[83]

Supercapacitors tend to be very similar in composition and setup compared to traditional capacitors, *i.e.* two electrodes are separated by a dielectric layer (separator). Although conventional capacitors use flat plates, the electrodes of supercapacitors are commonly carbon derivatives because they tend to possess higher surface areas, and more surface area equates to more sites for charge accumulation. Thus, supercapacitor electrodes tend to have far greater surface areas than that of capacitors, which enables a higher energy density by partially comprising its power density. Another functional difference involves separating capacitor electrodes with a layer of air while supercapacitors tend to be separated by membranes soaked in an electrolyte. With supercapacitors, the separator acts both as an insulator that separates the electrodes and a medium to facilitate ion transfer between the electrodes. These separators are often functionalized with ionic groups to enable both separation and ion conducting capabilities.

Researchers have divided electrolyte into several categories depending on the composition:[84]

I. Aqueous (*e.g.* KOH, KCl, H_2SO_4)

II. Organic (*e.g.* $TEABF_4$/ACN)

III. Ionic-Liquids (*e.g.* EMIM/BF_4)

IV. Solid-state or semi-solid-state, which can be further divided into: inorganic electrolyte, gel polymer electrolytes, and dry solid polymer electrolytes

V. Redox-active electrolytes. Overlaps with categories I-III, but special emphasis on redox-active compounds

Supercapacitors can be subdivided primarily into 2 types: EDLCs and pseudocapacitors. EDLCs are non-faradaic capacitors that store energy by separation of charge in a Helmholtz double layer.[85] Since, charge is stored non-faradaically, there is no charge transfer between electrode and electrolyte, which means that there will not be any chemical/composition changes (in either electrode or electrolyte), the charge/discharge is highly reversible and it will easily maintain a high cycling stability. Pseudocapacitors possess fast, reversible faradaic (redox) reactions at each electrode when a potential is applied. Here, the electro-activity is not merely limited to the surface, but occurs throughout the electrode. Comparing to EDLCs, pseudocapacitors tend to hold more capacitance, which equates to larger energy densities, but possess relatively lower power densities due to slower kinetics involving redox reactions occurring naturally slower than electrostatic accumulation. Moreover, they tend to have lower cycling stability due to the electrochemical changes constantly occurring within the electrode.

Actually, there is *another* type of supercapacitor that hybridize the two primary types called hybrid supercapacitors.[85] This hybrid technology capitalizes on the relative advantages, yet mitigate the disadvantages of EDLCs and pseudocapacitors. This technology can be further subdivided into: composites, asymmetric and battery type hybrid supercapacitors. Briefly, the composite subtype integrates carbon-based materials with either conducting polymers or metal oxides utilizing both charge storage mechanisms. The carbon material provides a high surface-area, conductive backbone for the complimentary component, which focuses on boosting capacitance. The asymmetric subtype combines faradaic and non-faradaic reactions *via* coupling an EDLC electrode with a pseudocapacitor electrode. Lastly, the battery subtype also couples two different electrodes, but from different energy storage types: a supercapacitor

electrode and a battery electrode. This technology compromises on a device that possesses a higher energy density than most supercapacitors and a higher power density than most batteries.

2.2.2.1 Principles of Operation

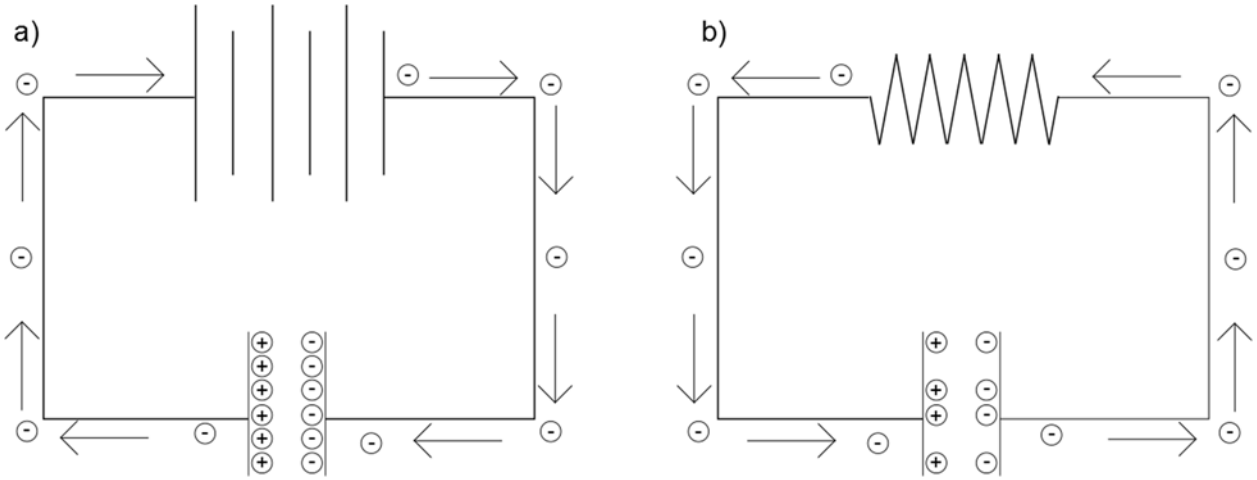

Figure 2-3. Schematic of a typical capacitor operation during a) charging and b) discharging

Supercapacitors are not only constructed very similarly to capacitors, but also operate very similarly. As seen in **Figure 2-3**, the basic operation of a capacitor is as follows. During charging where the capacitor is attached to an energy source **(Figure 2-3a)**, an electric field develops causing positive charges to accumulate on one plate and negative charges to accumulate on the other plate. The larger the plates, the more charge can be stored, and the greater the potential difference there will be in the capacitor. During discharge where the capacitor is attached to an external load **(Figure 2-3b)**, the accumulated charge on the plates will dissipate along with the potential difference.

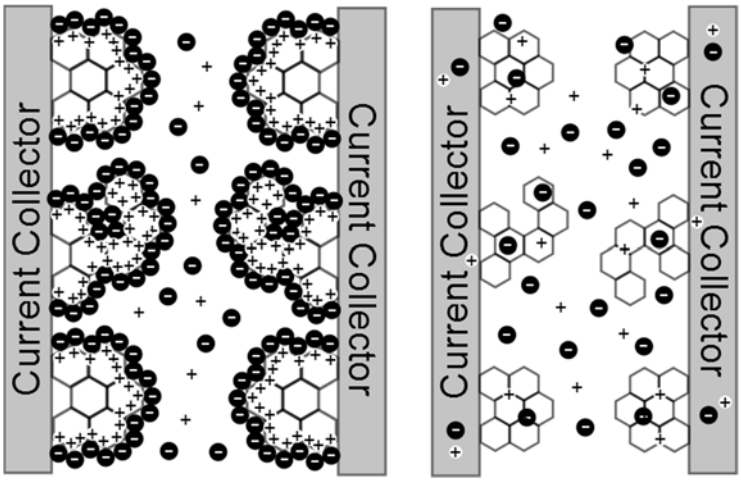

Figure 2-4. Diagram of electrostatic accumulation in EDLCs

As previously mentioned, EDLCs store energy by holding a separation of charge in the Helmholtz double layer.[85] When an energy source is applied, charges accumulate on electrode surfaces. The ions in electrolyte diffuse across separator into the pores of the electrode of the opposite charge. The electrodes prevent recombination of ions, and instead a double layer of charge is produced at each electrode. When the energy source is replaced with an external load, similar to capacitors, the potential difference dissipates, flowing electrons [86]from anode through the load into cathode until the electrodes are left at an electrical equilibrium.

2.2.3 Batteries (Zinc-Air)

In between fuel cells and supercapacitors (on the Ragone plot), lies batteries. But in particular, zinc-air cells are more like a hybrid between fuel cells and batteries, possessing properties that were otherwise unique to each technology. Zinc-air primary batteries, most known for their application in hearing aids, are metal-air batteries that generate energy by oxidizing zinc with oxygen from air. Moreover, there are mechanically and electrically rechargeable analogues, which have both been conceived and developed. The mechanically rechargeable cells can recharge by replacing the zinc anode and electrolyte, or use zinc powder to replenish reactants. This technology has yet to see large-scale usage due to the complexity of setting up a network of zinc depositing/recharging stations. Instead, the most efficient designs led researchers to zinc-air batteries that utilized a flowing electrolyte configuration, which also improved the durability of the zinc electrode.[87, 88]

Thus far, zinc-air cells have been used in various applications, and depending on the application, the size and assembly of the storage device differs. For example, button cells have been designed for small devices, *i.e.* hearing aids and watches. Larger batteries have been developed for large devices, *i.e.* film cameras. Lastly, very large batteries were created for electrical vehicle propulsion and even grid-scale energy storage.

Zinc-air cells have been well-researched due its high energy density, relatively low costs, safe operation and market-ready solutions. Compared to other metal-air batteries, zinc is abundant, low in cost and possess a low equilibrium potential. Moreover, zinc-air cells can be prepared at ambient conditions, whereas other metals, such sodium, lithium and potassium, require inert atmospheres (*e.g.* argon) for handling and battery assembly. Compared to lithium, the energy densities involving zinc are gravimetrically inferior, but volumetrically superior due to inherently higher atomic density of zinc metal.

Unfortunately, for small zinc-air batteries like button cells, it is not trivial to scale-up (with same construction) due to air diffusion performance, heat dissipation and leakage problems. For Psecondary zinc-air cells face other various challenges, which include dendrite formation, non-uniform zinc dissolution and limited solubility in electrolytes. Moreover zinc corrosion can produce potentially explosive hydrogen, which can be partially mitigated by use of vent holes. Lastly, the power density has been relatively low due to the catalysis challenges involving the oxygen gas that is fed into the air electrode.

2.2.3.1 Principles of Operation

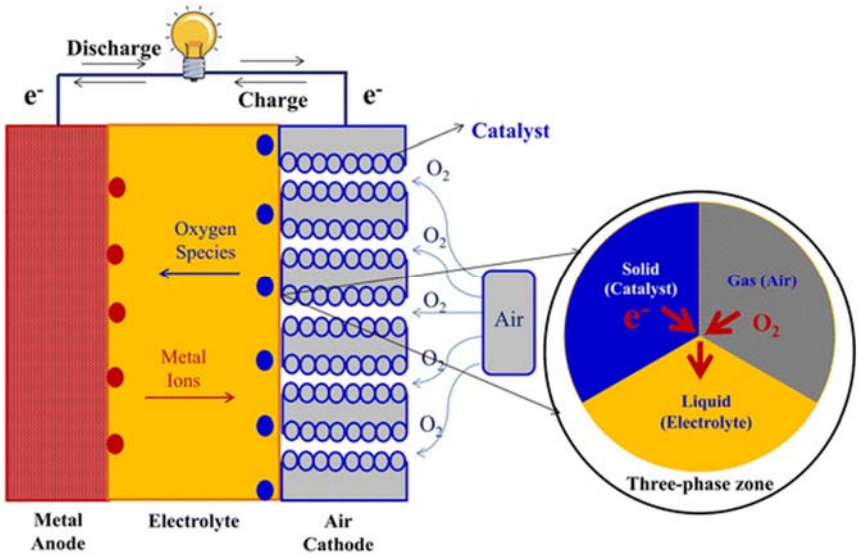

Figure 2-5. Simplified schematic of a discharging metal-air battery and corresponding three-phase zone. (Reprinted from Ref[89], with open access under Creative Commons Attribution 4.0 International License)

As depicted in **Figure 2-5**, a metal-air is typically comprised of four main components: an air electrode (usually a gas diffusion layer with a painted layer of catalyst), an alkaline aqueous electrolyte, a separator, and a metal (in this case, zinc) electrode.

During discharge, the oxygen from air diffuses/reacts at air electrode (cathode) and is reduced to hydroxide ions *via* ORR (**Equation (2-5)**) at the three phase interface (oxygen, electrolyte and electrocatalyst). Simultaneously, zinc cations are generated at zinc electrode. The generated hydroxide ions then migrate into the zinc electrode, where zinc is oxidized into zincate ($Zn(OH)_4^{2-}$) ions liberating electrons which travel to cathode *via* external circuit (**Equation (2-3)**). At super-saturated $Zn(OH)_4^{2-}$ concentrations, it will further decompose into insoluble zinc oxide (ZnO) and water (**Equation (2-4)**). The water from the anode is recycled at cathode (water is not consumed). The overall reaction produces theoretical 1.66V, but lower in practice. For charging, the reactions are reversed. Briefly, at the air electrode, oxygen evolution reaction (OER) occurs, where oxygen is generated and released. Meanwhile, the zincate ions are reduced back to zinc at the zinc electrode.

The described electrochemical reactions (for discharge) can be summarized in the following equations:

$$Zinc\ electrode = Zn + 4OH^- \rightarrow \mathrm{Zn(OH)_4^{2-}} + 2\mathrm{e^-}, \quad \mathrm{E_0 = -1.26V\ vs.\ standard\ hydrogen\ electrode\ (SHE)} \tag{2-3}$$

$$Electrolyte = \mathrm{Zn(OH)_4^{2-}} \rightarrow \mathrm{ZnO + H_2O + 2OH^-} \tag{2-4}$$

$$Air\ Electrode = {}^{1}/_{2}\, O_2 + \mathrm{H_2O + 2e^- \rightarrow 2OH^-}, \quad \mathrm{E_0 = 0.40V\ vs.\ SHE} \tag{2-5}$$

$$Overall = 2Zn + O_2 \rightarrow \mathrm{2ZnO}, \quad \mathrm{E_0 = 1.66V} \tag{2-6}$$

The equations for charging would be similar, but in the reverse directions.

2.2.4 Alcohol Fuel Cell Sensor (AFCS)

Although alcohol fuel cell sensors (AFCSs) are not quite considered an energy storage or conversion device, the fundamental working principle is based on the fuel cell. Breathalyzers, or breath analyzer, are devices that estimate the blood alcohol content (BAC) from a breath sample. Generally, the presence of alcohol can be detected in blood, urine, breath or *via* transdermal. Obtaining a blood or urine sample may be challenging, when the subject is in a public area or if the sample is needed within a very short timeframe. Obtaining samples *via* transdermal route tends to involve high costs and detection can produce false positive results.[90] The best option is an alcohol breath testing which is now more commonly used because sampling is non-invasive and the procedure is accurate, low-cost, convenient, and rapid in detection. Among the breathalyzers, there are three major types, which are based on either fuel cell, semiconductor, or infrared (IR) spectroscopy technology.

AFCSs are widely used and developed because it is not affected by environmental pollutants and other chemicals. It tends to have higher levels of sensitivity and selectivity to differentiate alcohol from acetone. The responses and recovery tend to be much quicker, which would allow for concurrent testing.

The disadvantages associated with AFCSs include a higher cost of manufacturing due to the use of platinum material and MEA setups. It also requires more power and parts, wherein devices tend to be bigger than the semiconductor-based devices. The state-of-art MEAs typically use a polyvinyl chloride membrane saturated with aqueous sulfuric acid, which are not safe and incompatible with electronic devices. This last drawback has been partially mitigated through a replacement with solid-state electrolyte membranes.

2.2.4.1 Principles of Operation

AFCS operates very similar to the direct alcohol fuel cell,[91] but for the purpose of detecting ethanol. The process starts with a subject exhaling into the breath analyzer device. An ethanol present in the breath is partially oxidized into acetic acid at the anode,[92] where electrons are released and flow through the external circuit. At the cathode, atmospheric oxygen is reduced, *i.e.* electrons are accepted from the anode and consumed by reducing the oxygen to water. This reaction oxidizes ethanol into acetic acid and water. The electric current that is produced is measured and translated as an approximation of the overall blood alcohol concentration.

The process can be summarized in the following equations

$$Anode: CH_3CH_2OH + H_2O \rightarrow CH_3CO_2H + 4H^+ + 4e^- \quad \textbf{(2-7)}$$

$$Cathode: O_2 + 4H^+ + 4e^- \rightarrow H_2O \quad \textbf{(2-8)}$$

$$Overall: CH_3CH_2OH + O_2 \rightarrow CH_3CO_2H + 4H_2O \quad \textbf{(2-9)}$$

For the approximation of the blood alcohol concentration, it is generally accepted based on Henry's law, that the ethanol concentration expelled from the lungs is directly proportional to the ethanol concentration in blood. Based on statistical sampling of many individuals, 1 mL of blood contains 2100 times more ethanol than 1 mL from the air in the lungs. Using this relationship, the blood alcohol concentration can estimated from the electric current that was detected from the AFCS.

Chapter 3: Characterization Techniques

3.1 Morphological and Elemental Analysis

3.1.1 Scanning Electron Microscopy (SEM)

Scanning Electron Microscopy (SEM) is the most popular and versatile method for visually examining surface microstructures and chemical compositions, as it is capable to view both organic and inorganic materials so long as the sample surface is conductive or can also be made conductive through carbon/gold sputtering. Graphically, it is capable of producing three-dimensional-like images due to its large depth of field. In SEM, an electron beam is focused through a series of condenser lens and swept across the surface of the specimen. The electrons decelerate upon coming in contact with the specimen and generate a variety of signals. For the scope of this project, the signals of interest are secondary electrons, backscattered electrons and X-rays. The most widely used signal is the secondary electron emission signal, which is used principally for its topological contrast, *i.e.* investigating surface texture and roughness.[93] The other signal, backscattered electrons, are used to examine compositional and topographic information.[93] In this thesis, SEM was utilized to investigate the layered structure observed at the cross-section of GO-based films.

3.1.2 Transmission Electron Microscopy (TEM)

Transmission Electron Microscopy (TEM) is a high-resolution, imaging tool used to view very small specimen, in the order of a few angstroms to sub-micrometers. Similar to the SEM operating principle, an electron beam is generated at a source and focused through a series of condenser-lens system, which in this case, also controls the illumination area of the sample.[94] Unlike SEM, TEM detects electrons which are transmitted through the thin specimen through a fluorescent screen, where it is then converted to an electric signal to produce the final image.[94]

There is a specific imaging mode in TEM called high-resolution transmission electron microscopy (HR-TEM),[95] which is also known as phase contrast. The HR-TEM allows for direct imaging of the atomic structure of the sample based on the phase of the electron waves that resulted from the specimen interaction. The TEM and HR-TEM aided in resolving the pore distribution and size of the nanopores in GO and pGO.

3.1.3 X-Ray Diffraction (XRD)

X-ray diffraction (XRD) is a technique used to explore the crystal structure and atomic spacing of a material. The XRD device is primarily comprised of 3 basic components: an x-ray tube, a sample holder and an x-ray detector. In XRD, either the X-ray tube and detector rotate simultaneously, or the sample rotates. X-rays are generated in an x-ray tube, filtered through a monochrometer, then collimated and directed onto the sample to produce diffraction patterns corresponding to the specific crystal planes.[96] The detected angle of diffraction can be related to the specific crystal orientation *via* Bragg's law as follows:

$$n\lambda = 2d\ sin\theta \quad \textbf{(3-1)}$$

where *n* represents the order of the spectrum, λ is the wavelength of the x-ray, *d* is the interplanar spacing detected from the diffraction signal, and θ is the diffraction angle.

In the case of graphene-based materials, the interplanar spacing also corresponds to the inter-sheet distance. It should be noted that XRD cannot detect amorphous materials, since it will result in diffuse patterns that resemble noise rather than distinct peaks as to that when scanning crystalline materials.

Scherrer's equation in **Equation 3-2** can be applied to define the relationship between the d-spacing and the number of layers per stack of graphene (oxide):[97]

$$L_c = {}^{(A\lambda)}\Big/_{(Bcos\theta)} \quad \textbf{(3-2)}$$

where *A* is the shape factor (~0.9); *B* is the full width at half maximum (FWHM) of the (002) peak in radians. In this project, XRD was used to compare GO samples, the interlayer spacing and their corresponding number of layers.

3.1.4 Raman Spectroscopy

Raman spectroscopy is a non-destructive characterization for obtaining high-resolution, structural and electronic information. The Raman spectrometer generates an intense, monochromatic electromagnetic beam that is focused on the sample, inducing a dipole moment. For the purpose of this study, the moment of interest is the inelastic scattering (also known as Raman scattering), which can be further divided into stokes and anti-stokes scattering.

Stokes/anti-stokes scattering occurs when there is a lower/higher energy of scattered radiation compared to the incident beam, resulting in an upshift/downshift (respectively) in frequency. This shift in frequency describes the characteristic information on the vibrational modes of the sample.

Typical to graphene-based materials, two characteristic peaks are seen at ~1350 cm^{-1} and ~1580 cm^{-1} which correspond to the D-peak and G-peak, respectively. The D-peak corresponds to degree of disorder within the sample,[98] or more specifically, to the double resonance process.[99] The G-peak corresponds to first order scattering of the stretching vibration mode E2g observed for the sp^2 carbon domain. As a result, the amount of defects present on a graphitic sample can often be characterized by the ratio of the intensity of the D-peak against that of the G-peak (I_D/I_G).

Tuinstra-Koenig[100] discovered an inverse relationship between the I_D/I_G ratio and the in-plane crystallite size, L_a, and described the relationship by the following equation:

$$L_a = (2.4\ x\ 10^{-10})\ \lambda^4\ (^{I_D}/_{I_G})^{-1} \quad \textbf{(3-3)}$$

Many decades later, due to the constant refining of research and technology, researchers found that utilizing Tuinstra-Koenig's law to calculate the crystallite size *via* the I_D/I_G ratio only held true under specific conditions. Instead, a modified relationship for a more generalized model was proposed; the proposal utilizes a ratio that accounts for the entire area under the D-band and G-band (A_D/A_G).[99, 101, 102] In the determination of the areas under the curve, the A_D can be decomposed by a Lorentzian (distribution) centered at the peak of the D band, while the A_G can be derived by using the Breit-Wigner-Fano (BWF) shape for the G band.[99, 101, 102] For this research, Raman spectroscopy was used to quantify the degree of graphitization, or conversely, the ratio of disorder to graphitization (A_D/A_G), as well as the in-plane crystallite size L_a.

3.1.5 Energy Dispersive X-ray Spectroscopy (EDX)

The energy dispersive X-ray spectroscopy (EDX) is an elemental analysis technique is that is used to determine the composition and distribution of spot area of the sample. It is commonly coupled with a SEM or TEM to complement the microscopic analysis. After bombarding the sample with electrons, X-rays are emitted and collected by a detector. EDS operates on the basis that each element has a unique set of binding energies enabling

appropriate identification.[103] The emitted X-ray variations can be spatially identified and overlaid on a corresponding SEM image to map the concentration of the differing elements. In this work, EDS identified the extrinsic elemental composition, their distribution in a sample, and confirm the results from XPS.

3.1.6 X-Ray Photoelectron Spectroscopy (XPS)

X-Ray photoelectron spectroscopy (XPS), also known as electron spectroscopy for chemical analysis (ESCA), is a quantitative technique that measures elemental compositions and electronic states existing on the surface. The operation of XPS begins with irradiating the surface with photons at a characteristic energy.[104] The photons then interact with the core electrons in the atoms of the sample.[104] As a result, ionized states are produced and a photoelectron is emitted with an energy approximately the difference between the photon energy and the binding energy.[104] The elements present on the sample can then be identified by back-calculating the binding energy. XPS was used to probe the surface for doped heteroatoms elements at different stages of the experiment, which helped elucidate the procedural mechanisms with hydroxyl radical oxidation and phytic acid functionalization.

3.1.7 Fourier-Transform Infrared (FTIR) Spectroscopy

Fourier-Transform Infrared (FTIR) Spectroscopy is commonly used to distinguish the molecular structures of organic compounds. It is used to obtain an absorption/emission spectrum in the infrared (IR) region. A broadband light source shines into a Michelson interferometer and then a detector measures the amount of light that is absorbed by the specimen. The beam is then configured to shine a different set of frequencies. This information is then translated to display the absorption at each wavelength.[105] Organic compounds possess a variety of vibrational motions from the constituent atoms, which result in a culminated IR spectrum corresponding to each component vibration. Conversely, existing bonds and functional groups can be identified by comparing absorption positions of IR spectrum with characteristic absorption regions. In this work, FTIR was used to confirm the molecular structure by analyzing the chemical bonds within the sample, and complemented by XPS to confirm and elucidate the procedural mechanisms.

3.2 Physical Properties

3.2.1 Thermal Gravimetric Analysis (TGA)

Thermal Gravimetric Analysis (TGA) is a destructive technique that monitors changes in physical and chemical properties as a function of (increasing) temperature. Generally, mass is lost or gained due to decomposition, oxidation or loss of volatiles. The TGA operates by heating the sample at a constant rate in either open-air or inert environment. Meanwhile, the mass is constantly monitored for the entire process and charted for further analysis. TGA can be used to quantitatively identify the temperature of degradation of GO-based membranes. Thus, it was used to confirm the high thermal endurance at the temperatures of interest.

3.2.2 Mechanical Properties

Mechanical properties encompass a plethora of equipment, characterization, and even established and standardized techniques (ASTM) used to describe the mechanical strength of materials. For example, a tensile tester can be employed to carry-out and quantitatively describe the mechanical properties of the samples. Typically, a sample is punched out in the shape of a fishbone or rectangle. Subsequently, the sample held between two vice grips, then slowly pulled in opposite directions. All the while, the resistance is measured and summarized in a stress/strain curve. Values, such as tensile strength, Young's modulus, elongation at break, toughness, *etc.*, can be extracted for further analysis. In this work, the mechanical properties were explored to ensure adequacy in their application.

3.2.3 Contact Angle (Water)

Contact angle is the quantitative measurement of the wettability of a liquid with respect to a solid surface *via* the Young Equation. A contact-angle goniometer measures the contact angle at the 3-interface point among the substrate, the air, and a liquid droplet (with respect to the droplet). For example, the static sessile drop method was conducted by pipetting a droplet of sample-containing solution (water) onto a static substrate of interest. Images are then captured by charge-coupled device camera. Wetting angles less than 90^{o} is considered wetting, or hydrophilic, while wetting angles between 90^{o} and 180^{o} is considered non-wetting, or

hydrophobic. The water contact angle was used to inspect how hydrophilicity varies depending on the composition.

3.2.4 Water Uptake (WU)

Water uptake (WU) measures the capability of an electrolyte membrane to retain water. The degree and rate at which the membrane absorbs water is correlated to the membrane's viscoelastic properties, which is interdependent on the membrane hydration. Increased hydration usually corresponds to enhanced ion conductivity and fuel cell performance.[106] To calculate WU, the membrane is initially soaked in deionized water at room temperature for 24 hours. Upon removing the water droplets from the surface of the membrane, it is weighed immediately. The membranes are then air dried, followed by drying in a desiccator for 4 hours, before their weights are measured again. The WU can be determined by the following equation:[59]

$$WU\ [\%] = \frac{W_{wet} - W_{dry}}{W_{dry}} \times 100 \quad \textbf{(3-4)}$$

where W_{wet} and W_{dry} are the mass of the wet and dry membrane respectively.

Alternatively, dynamic vapor sorption can also be used to calculate the water uptake. To ensure the sample is thoroughly dry, the sample is placed on a weighing pan (within a sealed chamber) and subjected to 0% RH N2 air for 8 hours at room temperature. The mass is measured and referenced as the dry weight. Subsequently, the sample is subjected to a 100% RH N_2 air until the change in mass with respect to time [dm $(dt)^{-1}$] is less than 0.004% to ensure that the sample is well saturated with water. This method was used in favor of submerging hydrophilic samples in water, wherein the process may disintegrate the material when submerged for extended periods of time.

3.2.5 Ion Exchange Capacity (IEC)

Ion Exchange Capacity (IEC) is an attribute of membranes which measures the number of ions that can be exchanged per unit mass of the membrane. Here, the dried samples are soaked in NaCl (*e.g.* 2 M) for 4 hours to exchange the sodium ions with existing protons held in the membranes. A back-titration is conducted using a known concentration of NaOH, and IEC values can be calculated *via* the following equation:[59]

$$IEC\ [meq/g] = \frac{V_{NaOH} * C_{NaOH}}{W_{dry}} \quad \textbf{(3-5)}$$

where V_{NaOH} is the titrant volume at equivalent point, C_{NaOH} is the molar concentration of the titrant, and W_{dry} is the dry mass of the membrane.

In this work, the WU and IEC were measured for calculating the proton mobility when combined with the ionic conductivity results.

3.2.6 Dynamic Vapor Sorption (DVS)

DVS is a gravimetric technique that measures the capacity of and how quickly the sample is able to absorb the solvent (water vapor).[107] The DVS operates by varying the vapor concentration in the environment immediate to the sample while simultaneously measuring the resulting change in mass. The DVS begins with measuring the dry mass of the sample. The sample is then subjected to a specified relative humidity (RH) profile, where the RH increases at step intervals, but rests for a certain amount of time to allow the sample to equilibrate before proceeding to the next RH step. During the evaluation, the mass is being tracked, recorded, and charted. The DVS was used to chart the water uptake and fitted to Park's model[108] to determine water mobility.

3.2.6.1 Park's Model[109]

Park's model is a multimodal adsorption model developed to fit water vapor adsorption isotherms. It is based on three different mechanisms for water adsorption/uptake (WU) and can be summarized by the following relationship:

$$WU = W_{SA} + W_{NSA} + W_C \quad \textbf{(3-6)}$$

where W_{SA} is specific adsorption (Langmuir model at lower water activity), W_{NSA} is nonspecific adsorption (Henry's law), W_C is clustering at high water activity. Each mechanism of absorption can be simplified to:

$$W_{SA} = \frac{Q_0 K_L a_w}{1 + K_L a_w} \quad \textbf{(3-7)}$$

$$W_{NSA} = K_H a_w \quad \textbf{(3-8)}$$

$$W_C = nK_A a_w^n \quad \textbf{(3-9)}$$

where Q_0 is the specific site capacity (mmol g^{-1}), K_L, is the affinity constant, K_H is Henry's Law coefficient (mmol g^{-1}), K_A is the aggregation equilibrium constant (mmol g^{-1}) regarding $nH_2O \rightleftharpoons (H_2O)_n$, n is the aggregate size, and a_w is the water activity/relative humidity. Substituting **Equations (3-7), (3-8)**, and **(3-9)** into **(3-6)** yields the expanded expression:

$$WU = \frac{Q_0 K_L a_w}{1 + K_L a_w} + K_H a_w + nK_A a_w^n \quad \textbf{(3-10)}$$

which was used to fit the moisture absorption isotherm. In this study, Park's model is fitted to the DVS-measured vapor isotherm in order to understand the behaviors of the water mobility at different humidity.

3.3 Electrochemical Characterization

3.3.1 Electrochemical Impedance Spectroscopy (EIS)

Electrochemical impedance spectroscopy (EIS) measures the impedance of a cell, which can be converted into an ionic/electrical resistance of a sample. In the process, a small alternate current (AC) sinusoidal potential is applied to the cell to measure the pseudo-linear response of the current, which can then be used to derive the impedance response of the system.[110] The resulting data is typically displayed in a Nyquist plot or a Bode plot. For membranes, EIS was used to investigate the through-plane and in-plane conductivity that were calculated from the real resistance.

3.3.2 Ionic Conductivity

For membranes, the sensitive responses from EIS are crucial for evaluating the ionic conductivity. The chemical potential distribution and polarisation are considered in the measurements of resistivity with the current flow, which can be divided into 2-probe and 4-probe methods. By using AC impedance spectroscopy, the ion conductivity of electrolyte membranes can be measured in the longitudinal (4-probe) or the perpendicular (2-probe) direction, and is calculated by the following relationship:

$$\sigma = \frac{L}{AR} \quad \textbf{(3-11)}$$

where for a 2-probe setup: σ is the ionic conductivity, *L* corresponds to the length between reference electrodes, *A* is the cross-sectional area, *i.e.* the product between the length of a probe and the thickness of the membrane, and *R* is the real resistance. For a 4-probe setup: σ corresponds the ionic conductivity, *L* is the thickness of the membrane, *A* is the planar area of the membrane, and *R* is the real resistance. The in-plane and through-plane conductivity were used to compare the capability to transfer ions (protons or hydroxides) between membranes.

By measuring the conductivity at different temperatures, the activation energy can be obtained *via* the Arrhenius relationship:

$$\sigma = \sigma_0 \exp(-\frac{E_a}{RT}) \quad \textbf{(3-12)}$$

where σ_0 is the pre-exponential factor, E_a is the activation energy, *R* is the gas constant and *T* is the thermodynamic temperature in K.

3.3.3 Proton Mobility

Proton mobility is an attribute that quantitatively describes how easily protons can move through a medium (*e.g.* membrane, water). Mobility is proportional to the conductivity and inversely proportional to the concentration of protons as shown in the following equation:[111]

$$u(H^+) \left[{}^{cm^2}/_{V^{-1}\, s^{-1}} \right] = \frac{\sigma}{Fc(H^+)} \quad \textbf{(3-13)}$$

where σ is the proton conductivity, *F* is Faraday's constant (96485 C/mol), $c(H^+)$ is the proton concentration which can be calculated by the following equation:[111]

$$c(H^+) \, [mol/L] = \frac{IEC * d}{WU} \quad \textbf{(3-14)}$$

where IEC is the ion-exchange capacity, d is the density of the solvent (water, taken as 1 g/ml), and WU is the water uptake. The proton mobility was used to quantitatively contrast and to confirm trends observed in the ionic conductivity.

3.3.4 Linear Sweep Voltammetry (LSV)

LSV is a voltammetry technique that measures current while sweeping the electric potential at a constant rate (similar to CV, but only from lower to upper limit). It is often used to screen for redox reactions, which would be detected as a peak/trough in the signal. The characteristics of the LSV response depend on (i) rate of electron transfer reaction; (ii) Chemical reactivity of electroactive species; and (iii) voltage scan rate. The results are typically outputted as current-potential (I-V) graphs. In this work, LSV will be used to confirm the electrical resistance of the membranes.

3.3.5 Battery Performance Evaluation

This section provides a quick overview on some well-discussed criteria that are used to evaluate energy storage devices (*i.e.* supercapacitors, zinc-air batteries, and alcohol fuel cell sensors). The de facto parameters such as, operating voltage, power density, energy density, specific capacity and cycling stability can be revealed in the following characterizations.

3.3.5.1 Cyclic Voltammetry (CV)

Cyclic Voltammetry is an electrochemical technique that measures the current, while varying the electric potential at a constant rate. It is typically used to investigate the rate performance and capacitance of the device. The potential towards the working electrode gradually changes at a set ramp rate, then reverses the scan back to the initial potential. Meanwhile, the current response is simultaneously measured, then plotted on a “CV” graph.

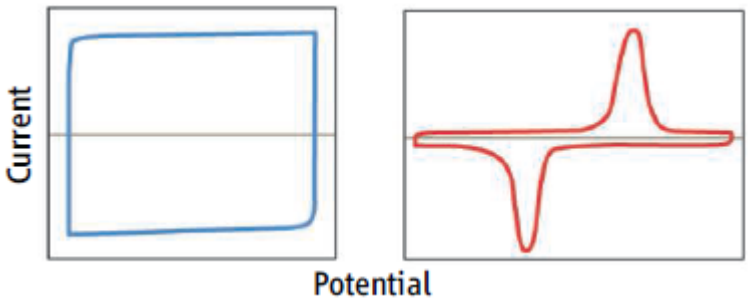

Figure 3-1. Cyclic Voltammograms distinguishing the difference between capacitor and battery materials. (Reprinted from Ref.[112] with permission from AAAS)

Figure 3-1 shows CVs of supercapacitors that when applied to a constant rate in the potential will typically exhibit either a linear current response (in blue), or faradaic redox peaks (in red), or sometimes a combination of both. The rectangular shape highlights the rapid electrostatic accumulation, while the peaks highlight the occurrence of redox reactions. In this project, CV is used to confirm the low ionic transfer resistance in the membrane, *i.e.* to conduct ions quick enough to preserve the supercapacitance behavior.

3.3.5.2 Galvanostatic Charge/Discharge (GCD)

GCD, also known as chronopotentiometry, is a widely used technique to evaluate polarization, specific capacity, energy/power density, equivalent series resistance, and stability. As the name implies, GCD, applies a constant or step current and measures the potential response as a function of time. The durability can be evaluated with a large loop of charging and discharging cycles. Durability is a key indicator of stability and reaction reversibility.[113] GCD is used to compare polarization losses and confirm the pragmatic functionality of the membrane in a flexible battery.

3.3.6 (Alcohol) Fuel Cell Gas Sensor (AFCS) Evaluation

Alcohol fuel cell gas sensor (AFCS) functions in principle similar to that of a fuel cell. As the name implies, this device detects alcohols (*i.e.* ethanol). Human breath is simulated by preparing a predetermined ethanol vapor mixture; the vapor mixture was then injected into the AFCS system at a fixed volume. The vapor is subsequently detected, which triggers the ethanol

oxidation reaction (EOR) at the anode and oxygen reduction reaction (ORR) at the cathode. As a result this reaction process, electrons are released and captured; the signal can then be correlated to a concentration of ethanol vapor. The AFCS was built to evaluate the sensitivity and selectivity of the membrane in detecting alcohol from a human breath simulation.

Chapter 4: Imidazole-doped Graphene Oxide for Enhanced Hydroxide Conductivity

This chapter is adapted with permission from Zarrin H, Sy S, Fu J, Jiang G, Kang K, Jun YS, Yu A, Fowler M, Chen Z. Molecular Functionalization of Graphene Oxide for Next-generation Wearable Electronics. ACS Applied Materials & Interfaces. 2016 Sep 15;8(38):25428-37.

4.1 Introduction

Entering the golden era of wearable electronics has urged the development of fully solid, lightweight, flexible, and efficient energy storage devices (*e.g.* batteries and supercapacitors) to be reliable at different environments.[114-116] To accomplish this, the compartments of energy storage systems (*e.g.* electrodes and electrolytes) must be replaced with flexible materials having high sustainability at various operating conditions.[116-118] Specifically, the ion-conductive electrolytes in these systems are voluminous and undesirable since their performance is highly dependent on the operating temperature and relative humidity (RH) levels.[119, 120] Thus, it is essential to replace them with a flexible and lightweight electrolyte membrane (EM) possessing high and stable ionic conductivity at not only fully humidified and elevated temperatures but also low RH and room temperature conditions.

Recently, the research has focused on the development of graphene oxide (GO)-based EMs to (i) enable the fabrication of lightweight and flexible electronics and (ii) increase the compatibility of carbon-based electrodes with the electrolyte.[9, 41, 44, 59, 121-126] Because of its ultrahigh surface area, yet nanoscale thickness,[52, 127] GO nanosheets and their derivatives can simply stack and form stable, lightweight, and flexible membranes. However, the rate of ion conduction in GO-based EMs is highly sensitive to the changes of the operating conditions and extremely dependent on the existence of water in the system (*i.e.*, RH). GO is intrinsically proton-conductive, electrical insulator and highly hydrophilic. Thus, the interlayer spacing widens as RH increases,[47] enabling water molecules to be trapped within, and as a result increases the rate of ion transfer. Accordingly, when the humidity decreases, the ion conductivity will drastically decline (*e.g.* by 1 order of magnitude).[44] Since a practical ion-conductive EM requires a minimum ion conductivity of 0.01 S cm^{-1} at different operating

conditions,[128] it is vital to efficiently boost that for the GO-based EMs with slightest dependency on the operating conditions (*e.g.* RH and temperature).

The existence of enormous oxygenated groups (*e.g.* hydroxide, epoxy, and carboxyl groups) on the basal plane and edges of the nanosheets enables chemical functionalization of GO[127] and manipulation of its electrical and physicochemical properties for the desired application. Herein, to develop a flexible GO-based EM with high ion conductivity and minimum dependency on the operating conditions, especially at low RH and room temperature, the large surface area of GO has been functionalized with 1-hexyl-3-methylimidazolium chloride (HMIM) molecules *via* both esterification and electrostatic $\pi_{cation}-\pi$ stacking reactions. HMIM is an imidazolium-based ionic liquid with low viscosity and high thermal stability.[129, 130] The combination of bulky and asymmetric cations and anions in HMIM yields an architecture possessing considerable ion conductivity and electrochemical stability at not only different RH and temperatures but also alkaline pHs.[130] These extraordinary features within HMIM has resulted in a freestanding HMIM/GO membrane with a superior hydroxide conductivity of 0.064 ± 0.0021 S cm^{-1} at 30% RH and room temperature with minimum dependency on the operating conditions when compared to the commercial polymeric membrane. To study the practical application of the HMIM/GO films in wearable electronics, a fully solid-state, thin, flexible zinc–air battery and supercapacitor have been fabricated exhibiting high battery performance and capacitance at low humidified and room temperature conditions, respectively. The successful results of this study manifest the feasibility of using the thin and flexible HMIM/GO membrane as a reliable solid EM in energy storage systems and wearable electronics at different operating conditions.

4.2 Experimental Section

All materials were purchased from Sigma Aldrich (unless specified) at an ACS reagent grade or higher, and used without further purification. Furthermore, any water used in the work was of double-deionized (DDI) water.

4.2.1 Preparation of Graphene Oxide

GO was prepared in a batch reaction *via* the oxidation of graphite powder (2−15 μm, Alfa Aesar) *via* modified Hummer's method.[16, 131] Specifically, 5 g graphite powder and 2.5 g sodium nitrate were mixed with 115 ml concentrated sulfuric acid in an ice bath. Shortly after, 15 g potassium permanganate was slowly added in 2 g aliquots. Subsequently, the ice bath was removed and the mixture was allowed to stir for 2 h. Then while stirring, 350 mL water was added slowly and left to stir for another 30 mins. Yet while stirring, another 300 mL water was added, followed by 100mL hydrogen peroxide (30 wt%), and finally yielding the golden brown mixture. Lastly, the mixture was washed with 3L hydrochloric acid (5%) and copious amounts of water until the pH > 4.

4.2.2 x-HMIM/GO Membrane Fabrication

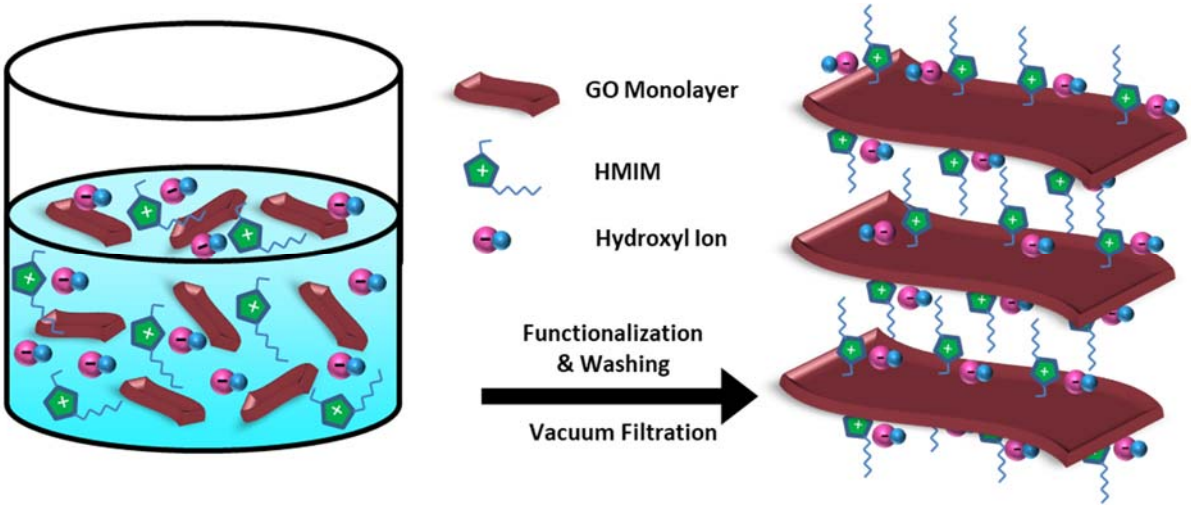

Figure 4-1. Scheme of the experimental procedure preparing free-standing x-HMIM/GO membranes from functionalizing GO nanosheets with HMIM.

Figure 4-1 illustrates the process of preparing freestanding x-HMIM/GO membranes (x = weight ratio of HMIM to GO = 1, 2, 5, or 10) at GO:HMIM:KOH weight ratios of 1:1:1, 1:2:2, 1:5:5, and 1:10:10. Firstly, GO (40 mg) was dispersed in water and then mixed with HMIM and KOH at room temperature for 48 h. Thereafter, the homogeneous solution was centrifuged several times with water to remove any excess KOH and unreacted HMIM. Then, the resulting

x-HMIM/GO was redispersed into water before casting into a membrane *via* the vacuum filtration method using an Anodisc membrane (47 mm in diameter, 0.2 μm pore size, Whatman). Lastly, the freestanding membrane was further air dried and then, peeled from the filter paper. The thicknesses of all membranes were in the range of ~26−32 μm.

4.2.3 Zinc-Air Battery Fabrication

To prepare the air electrode in the Zn−air battery, a gas diffusion layer (GDL, Ion Power Inc., 25BC) was coated with catalyst ink prepared by sonicating a mixture of active material and carbon black, in a 2:1 mass ratio, which is dispersed in isopropyl alcohol, and a binder (AS-4 ionomer, Tokuyama Inc.) that is 10 μL mg^{-1} of the total mixture. Co3O4 nanoparticles (<50 nm particle size) were used as the bifunctional electroactive material for the air electrode at a density loading of 1.0 mg cm^{-2}. A stainless-steel mesh was selected the as the current collector to be attached to the air electrode, serving both as an electrical conductor and a pathway for the passing oxygen. For the anode, a zinc pellet was prepared using cold compaction of zinc powder (purum) under a pressure of 5 MPa for 2 min. Then, copper foil was applied to the zinc anode as a current collector. Before assembly into the Zn-air battery, the 5-HMIM/GO and A201 EMs were preconditioned at 50% and 90% RH, respectively, and at ambient temperature for 2 h. The all-solid-state Zn−air battery, with an active surface area of 1.13 cm^2, was fabricated by sandwiching the solid electrolyte membrane between the zinc pellet and bifunctional, air electrode. The single-cell electrochemical evaluation was conducted with a battery prototype fabricated in-house using atmospheric air as the oxygen source. To obtain the galvanodynamic charge/discharge profiles of the battery, a potentiostat (Princeton Applied Research, VersaSTAT MC) was used to measure the changes in the voltage while the current density scanned from 0 to 20 mA cm^{-2} at a step interval of 1 mA cm^{-2}. The cyclability test was performed on the Zn-air batteries, made of HMIM/GO and A201 membranes at ~50% and 100% RH, using a pulse cycling technique, where each cycle was run for 10 min at a current density of 200 mA g^{-1}.

4.2.4 Supercapacitor Fabrication

To prepare the carbon electrodes in the symmetrical supercapacitor, stainless steel shims (0.07 mm, type 304, Custom Gaskets Ltd.) as the current collectors, were coated with a

thin layer of aqueous, conductive-carbon ink (Anders Products) and dried overnight at 40 °C. Albeit the carbon-ink possesses a low capacitance, it was selected to minimize the influence of pores and divert the focus to the solid electrolyte performance. The active area of the electrodes was set to 1 cm^2. Before the assembly, the 5-HMIM/GO and A201 EMs were preconditioned at 50% and 90% RH, respectively, and at ambient temperature for 2 h. The supercapacitor cell was then assembled by sandwiching the solid electrolyte membrane between the electrodes. Electrochemical characterizations were carried out at room temperature by cyclic voltammetry (CV) and EIS on the potentiostat.

4.2.5 Physicochemical Characterization

The structural integrity and distribution of elements in the x-HMIM/GO membranes were examined *via* cross-sectional SEM images and EDX mapping (LEO FESEM1530). XRD (INEL XRG 3000) and Raman spectrometry (Bruker Senterra, 532 nm laser) were utilized to study the changes in the crystallinity of the samples and the effects of disordering on the plane. The elemental and chemical-bonding analyses of x-HMIM/GO membranes were examined *via* XPS (Thermo Scientific Al KAlpha X-ray source) and FTIR (Avatar 320) to elucidate the possible mechanism of functionalization. To assess the thermal behavior of GO and x-HMIM/GO membranes, the thermogravimetric analysis (TGA, TGAQ500 V20.10) was performed under nitrogen in the temperature span of 25 to 800 °C at a heating rate of 10 °C min^{-1}. The water contact angle on the surface of freestanding membranes was measured using an optical tensiometer (CA 2500 XE) with the software (AST Products, Billerica, MA) to inspect how the hydrophilicity changes with the loading of HMIM in GO.

4.2.6 Electrochemical Characterization

To measure the in-plane ionic conductivity, all free-standing membranes and the commercial A201 were sandwiched in a four-probe cell made of platinum wires and Teflon plates. To perform the through-plane conductivity test, all *x*-HMIM/GO membranes were pressed between two stainless steel rods with 1 cm^2 surface area. In order to calculate the ionic resistance at different temperatures and relative humidity (RH), the conductivity cell was accommodated inside a lab-made thermal-controlled humidity-chamber. Exposing the cell to different RH levels was performed by mixing water-saturated nitrogen with dry nitrogen flow at

different temperatures. For measuring the real temperature, a thermocouple sensor was placed in close proximity to the sandwiched membrane. To stabilize the operating conditions, the cell remained at least 1 h at each specific temperature and RH until no changes were observed in the hygrometer and thermometer. AC electrochemical impedance spectroscopy (EIS) was applied to evaluate the ionic conductivity by estimating the real impedance of samples from the Bode plots using Princeton Versastat MC potentiostat. The frequency range was between 1 MHz and 10 Hz with perturbation voltage amplitude of 50 mV. At a given temperature and RH, the measurements were repeated at least four times with 10 min interval. The hydroxide conductivities were then calculated using **Equation (3-11)**.

4.3 Results and Discussion

4.3.1 Physicochemical Characterization

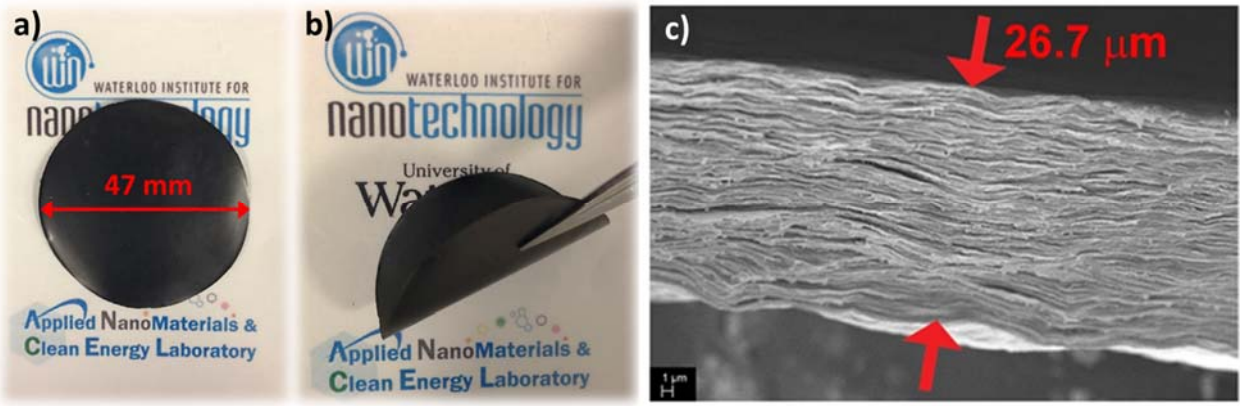

Figure 4-2. (a) Digital photo of freshly vacuum-filtered, 47 mm-diameter, 10-HMIM/GO membrane. (b) Digital photo demonstrating the flexibility of a 10-HMIM/GO membrane. (c) Cross-sectional SEM image of 10-HMIM/GO membrane indicating the thickness of 26.7 um.

The vacuum filtration method yielded a uniform, smooth-surfaced, freestanding, and flexible x-HMIM/GO membranes ('x' represents the weight ratio to GO; x = 1, 2, 5, 10), as shown in **Figure 4-2a, b** The cross-sectional SEM picture shown in **Figure 4-2c** reveals the morphology of the 26.7 μm 10-HMIM/GO membrane where the functionalized GO nanosheets are stacked layer by layer forming a flexible membrane.

Table 4-1. Mechanical Properties of GO and 5-HMIM/GO Membranes

Membrane	Tensile strength (MPa)	Young's Modulus (GPa)	Elongation at break (%)	Toughness (MPa)
GO	39.55	3	1.08	0.14
5-HMIM/GO	35.49	1.7	2.13	0.37

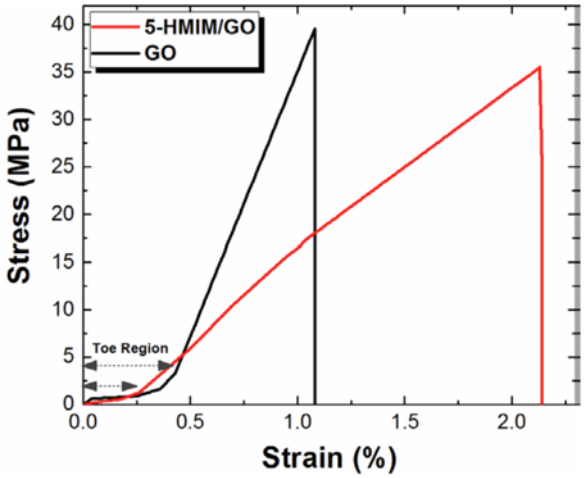

Figure 4-3. The Stress-strain plot of GO and 5-HMIM/GO membranes at room temperature (26 °C) and RH of 35%.

To determine the effects of HMIM functionalization on the mechanical strength of HMIM/GO membrane, the typical stress-strain curves for GO and 5-HMIM/GO membranes are shown in **Figure 4-3**. The tensile strength, Young's modulus, elongation at break, and toughness are listed in **Table 4-1**. At the beginning phase of tension test, a non-linear relation between stress and strain can be observed, which is called toe region. This region does not express any mechanical property of the samples and occurs because of the wavy form of the membranes when placed in the machine. When samples are completely straightened, the elastic region starts, where the stress and strain are linearly correlated. The HMIM functionalization has reinforced the mechanical strength of GO-based EM by boosting the toughness about 62% and becoming more flexible than the bare GO film.

Figure 4-4. The EDX mapping of a) carbon, b) oxygen, and c) nitrogen elements distributed between the layers of 10-HMIM/GO membrane.

Figure 4-4a-c represent the EDX mapping of carbon, oxygen, and nitrogen in the cross section of 10-HMIM/GO membrane, respectively, confirming the uniform distribution of aforementioned elements through the layers of GO nanosheets.

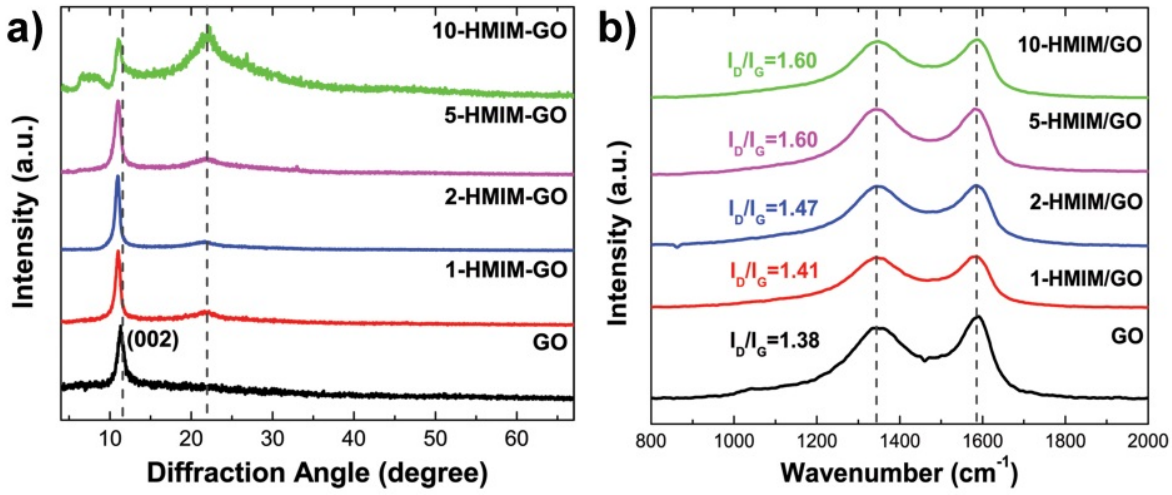

Figure 4-5. a) The XRD, and b) Raman spectra of free-standing GO and x-HMIM/GO membranes

Table 4-2. The calculated crystallite sizes using XRD and Raman spectra

Sample	XRD		Raman	
	β	*La (nm)*	*ID/IG*	*La (nm)*
GO	0.012	11.20	1.38	14.14
1-HMIM-GO	0.013	10.07	1.41	13.84
2-HMIM-GO	0.014	10.01	1.47	13.28
5-HMIM-GO	0.015	9.51	1.60	12.20
10-HMIM-GO	0.015	9.53	1.60	12.20

The XRD spectra of GO and x-HMIM/GO membranes in **Figure 4-5a** reveals how the interlayer spacing changes after functionalizing GO with HMIM ionic liquid. **Table 4-2** compares the calculated crystallite sizes (*La*) of GO and *x*-HMIMI/GO membranes from Raman and XRD results. In the Raman spectra, from the integrated intensity ratio (I_D/I_G) the L_a of all samples were estimated using the Tuinstra-Koenig relationship as follows:[100, 132]

$$L_a = (2.4 \times 10^{-10})\lambda^4 \left(\frac{I_D}{I_G}\right)^{-1} \quad \textbf{(4-1)}$$

where *λ* (nm) is the Raman laser line wavelength. In order to measure the crystallite size of GO and *x*-HMIM/GO membranes from the XRD spectra, the critical (002) peak was analyzed which gives the required information for the lattice size of GO utilizing Scherrer's equation as follow:

$$L_a(002) = \frac{K\lambda}{(\beta cos\theta)} \quad \textbf{(4-2)}$$

where L_a (002) is the size of crystallite in nm, *K* is a constant dependent on the crystallite shape (0.89), *λ* is the X-ray wavelength in nm, *β* is the full width at half maximum (FWHM) in radian, and θ is the scattering angle in radian.

The GO membrane shows the typical sharp (002) peak at 2θ = 11.33°, which corresponds to an interlayer spacing of 7.80 Å.[133] As the weight ratio of HMIM increases in functionalizing GO, the GO (002) peak broadens and shifts to a lower diffraction angle of 10.98°, which corresponds to a higher interlayer space of 8.05 Å. This infers the incorporation of bulky HMIM groups onto the surface of GO, which increased the distance between the stacked nanosheets and decreased the crystallinity of GO nanosheets. The crystallite sizes of GO and x-HMIM/GO membrane were estimated *via* Scherrer's equation (**Equation (3-2)**), verifying the reduction of GO crystallite size when increasing the loading of HMIM (**Table 4-2**). Furthermore, the loading increase of HMIM functional groups newly developed a diffraction peak at 22.03°. The emergence of such a broad peak is attributed to the extended degree of functionalization by increasing the amount of HMIM, which reinforced the exfoliation and disordered spacing between the lower-crystalline, stacked interlayers.[123, 134]

Raman spectroscopy was employed to quantify the surface defects on the GO and x-HMIM/GO membranes (**Figure 4-5b**). For all samples, the two typical Raman bands for GO-based materials are located at ~1580 and ~1345 cm^{-1}, which are generally referred to the G band (*i.e.*, vibrations of graphitic sp^2-hybridized carbon) and D band (*i.e.*, vibrations of sp^3

carbon atoms due to the defects and disorders on the graphene surface and edges), respectively.[135-137] The addition of HMIM is reflected in the increase of integrated intensities of the D to G bands (I_D/I_G) ratio, confirming the successful incorporation of HMIM on the basal plane. This implies that HMIM functionalization has resulted in a net increase of surface defects. However, the I_D/I_G ratio remained the same for 5-HMIM/GO and 10-HMIM/GO, indicating that the GO surface has been saturated with HMIM groups. It is well known that the in-plane crystallite size (L_a) of GO is inversely proportional to I_D/I_G.[98, 132, 138] L_a for GO and x-HMIM/GO membranes were calculated (**Table 4-2**) using the Tuinstra−Koenig equation (**Equation (3-3)**).[100] **Figure 4-5b** indicate the reduction of crystallite size, by the increasing I_D/I_G, as the HMIM loading increased in GO. The trends observed in the crystallite size from Raman are consistent with that from XRD, where both characterizations demonstrated a lower crystallinity for HMIM/GO membranes with higher loadings of HMIM.

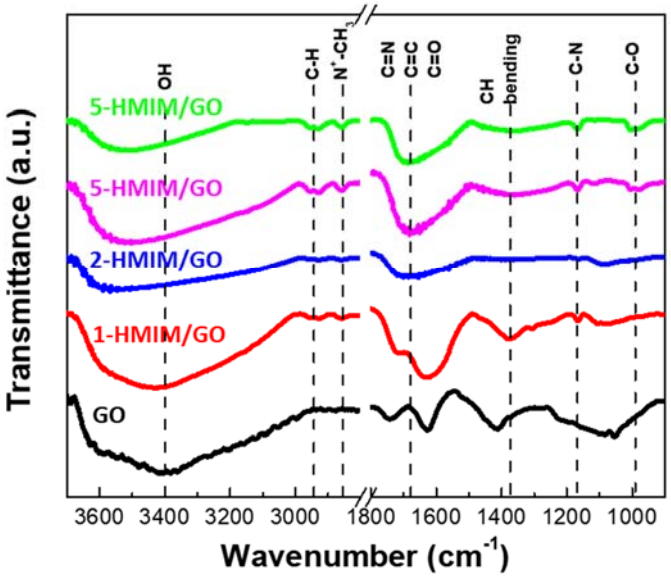

Figure 4-6. FT-IR spectra of freestanding GO and x-HMIM/GO membranes.

Figure 4-6 displays the FT-IR spectra of GO and x-HMIM/GO freestanding membranes, which acknowledge the chemical attachment of HMIM to GO nanosheets. The GO spectrum is consistent with previous reports where the IR peaks at 1054, 1412, 1628, 1742, and 3417 cm^{-1} were referred to the vibrations of epoxy (C−O), carbon−hydroxyl (C−OH), sp^2 carbon (C=C), carbonyl/carboxyl (C=O), and free hydroxyl (OH) groups, respectively.[59, 123, 139] When the amount

of HMIM functionalization increased, the stretching vibrations of epoxy groups significantly weakened and shifted to a higher wavenumber of 1170 cm^{-1}. Alternately, a newly broad peak emerged at 1080 cm^{-1} for 1-HMIM/GO and 2-HMIM/GO, which shifted to 990 cm^{-1} for 5-HMIM/GO and 10-HMIM-GO membranes. This developed peak was attributed to the stretching vibrations of C−N bonds either in the imidazolium ring or formed on the surface of GO after ring-opening reaction (refer to functionalization mechanism). After functionalization, the C−OH bond shifted to a lower wavenumber of 1370 cm^{-1}, which gradually broadened as the loading of HMIM increased. It is assumed that this broad peak could be an overlap of C−H bending in the imidazolium ring and stretching vibrations of C−OH on the GO surface.[140-142] The deformation of epoxy and hydroxyl groups conveyed the cruciality of their presence in the interactions between GO and HMIM. It was seen that by increasing the weight ratio of HMIM to GO, the C=C and C=O peaks gradually merged into a broad peak at 1670 cm^{-1} representing C=N, C=C, and C=O bonds in x-HMIM/GO membranes. The two newly appeared peaks at 2860 and 2935 cm^{-1} were attributed to the cationic nitrogen bonded to the methyl group ($N^{+}-CH_3$) and stretching C−H bond in HMIM, respectively. Except for 1-HMIM/GO, the very broad −OH peak redshifted to ∼3530 cm^{-1} for all x-HMIM/GO membranes, indicating that HMIM was attached onto GO and that this peak shift may be due to the chemical bonding between these two components.[139]

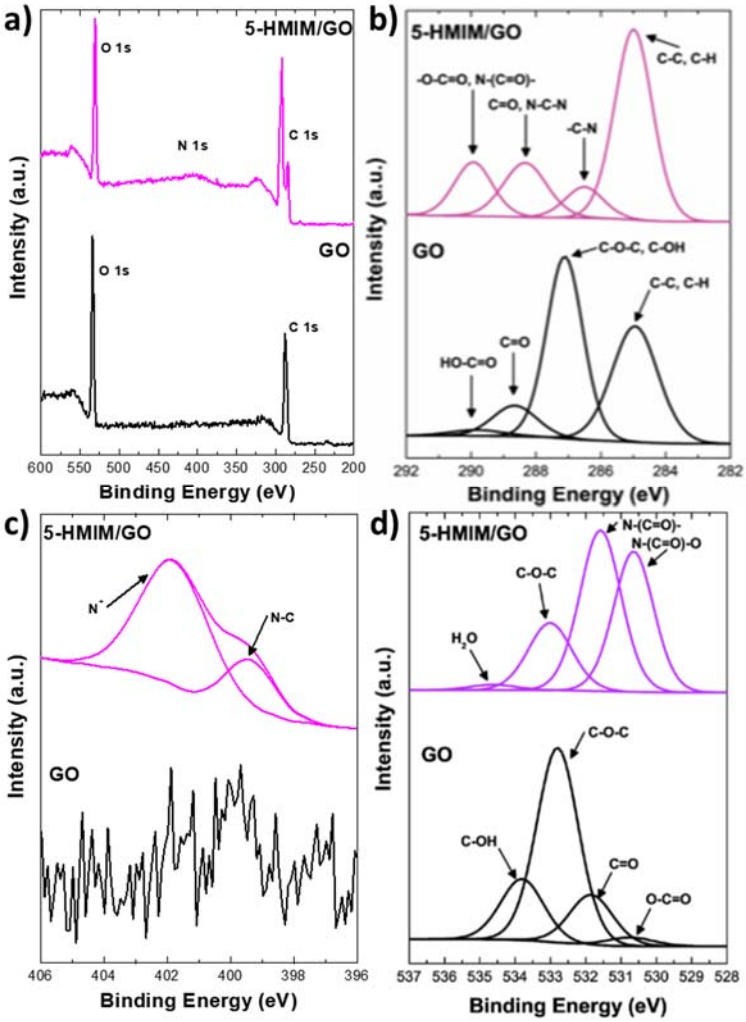

Figure 4-7. (a) Low-resolution XPS, (b) high-resolution C 1s XPS, (c) high-resolution N 1s XPS, and (d) high-resolution O 1s XPS spectra of freestanding GO and 5-HMIM/GO membranes.

Figure 4-7a demonstrates the survey XPS data for GO and 5-HMIM/GO membranes where the emergence of nitrogen peak in 5-HMIM/GO, with an atomic percentage of 4.89%, confirms the successful HMIM-functionalization onto GO. In order to investigate the types of chemical bonds that developed after functionalization, broad scans of C 1s, N 1s, and O 1s spectra were recorded for both GO and 5-HMIM-GO in **Figure 4-7b-d**. The C 1s spectra in **Figure 4-7b** were deconvoluted into four peaks. The GO membrane exhibited aromatic C 1s peaks at 284.94 eV (sp^3-hybridized C−C/C−H), 287.11 eV (epoxide, C−O−C/hydroxyl, −C−OH), 288.66 eV (carbonyl, C=O), and 289.83 eV (carboxyl, O=C−OH), which are in agreement with the literature.[59, 123] The C 1s spectrum for 5-HMIM/GO revealed an intense C−C/C−H peak at

284.99 eV, which is due to the long hexyl chain attached to HMIM. The disappearance of the epoxide/hydroxyl peak and the emergence of a new peak at the binding energy of 286.51 eV in 5-HMIM/GO can be attributed to either the interaction between the pyridinic nitrogen atoms and carbon in the imidazolium ring of HMIM (*i.e.*, −C−N), or the newly formed −C−N bonds after the ring-opening reaction of HMIM with GO. Furthermore, the carbonyl and carboxyl peaks in 5-HMIM/GO membrane became sharper after slight shifts to 288.34 and 289.93 eV, respectively. These intensifications can be assigned to N−C−N bonds in the imidazolium ring of HMIM and the formation of O=C−N− bonds covalently attached to the surface of GO *via* the ring-opening reaction.[143] The N 1s spectra of GO and 5-HMIM/GO membranes compared in **Figure 4-7c** confirms the successful functionalization of GO with HMIM groups since GO does not typically contain any nitrogen. In 5-HMIM/GO membrane the developed N 1s bond at 399.41 eV correspond to either the pyridinic nitrogen atoms (−C−N) in HMIM or the generated N−(C=O)− bonds after the ring-opening reaction.[144] The lifted peak at 401.78 eV represents the cationic nitrogen in either the imidazolium ring of HMIM or the produced secondary ammonium when HMIM has been covalently bound to GO nanosheets.[143] **Figure 4-7d** represents the high resolution O1s spectra of free-standing GO and 5-HMIM/GO membranes. The GO membrane exhibited the typical peaks at 530.74 eV (carboxyl, O=C–OH), 531.85 eV (carbonyl, C=O), 532.8 eV (epoxide, C–O–C), and 533.8 eV (hydroxyl, –C–OH) which were similar to the previous reports.[59, 123] After functionalizing the GO with HMIM groups, the carboxyl and carbonyl peaks were significantly intensified assigned to the generation of N–(C=O)–O and N –(C=O)– bonds after the ring-opening reaction through which the HMIM is covalently bound to the GO surface. The intensity reduction of epoxide peak at 533.01 eV and the disappearance of hydroxyl peak additionally support the ring-opening of epoxide on GO surface and the reaction of hydroxyl groups with the ring-opened HMIM. The very broad but weakly emerged peak at 534.6 eV is assigned to the existence of trapped water molecules in 5-HMIM/GO membrane. The intensified carboxylic and carbonyl peaks in the O 1s spectrum of 5-HMIM/GO membrane in **Figure 4-7b** compared to those in the GO spectrum in **Figure 4-7d** further approve the occurrence of the ring-opening reaction between HMIM and GO nanosheets.

4.3.2 Functionalization Mechanism

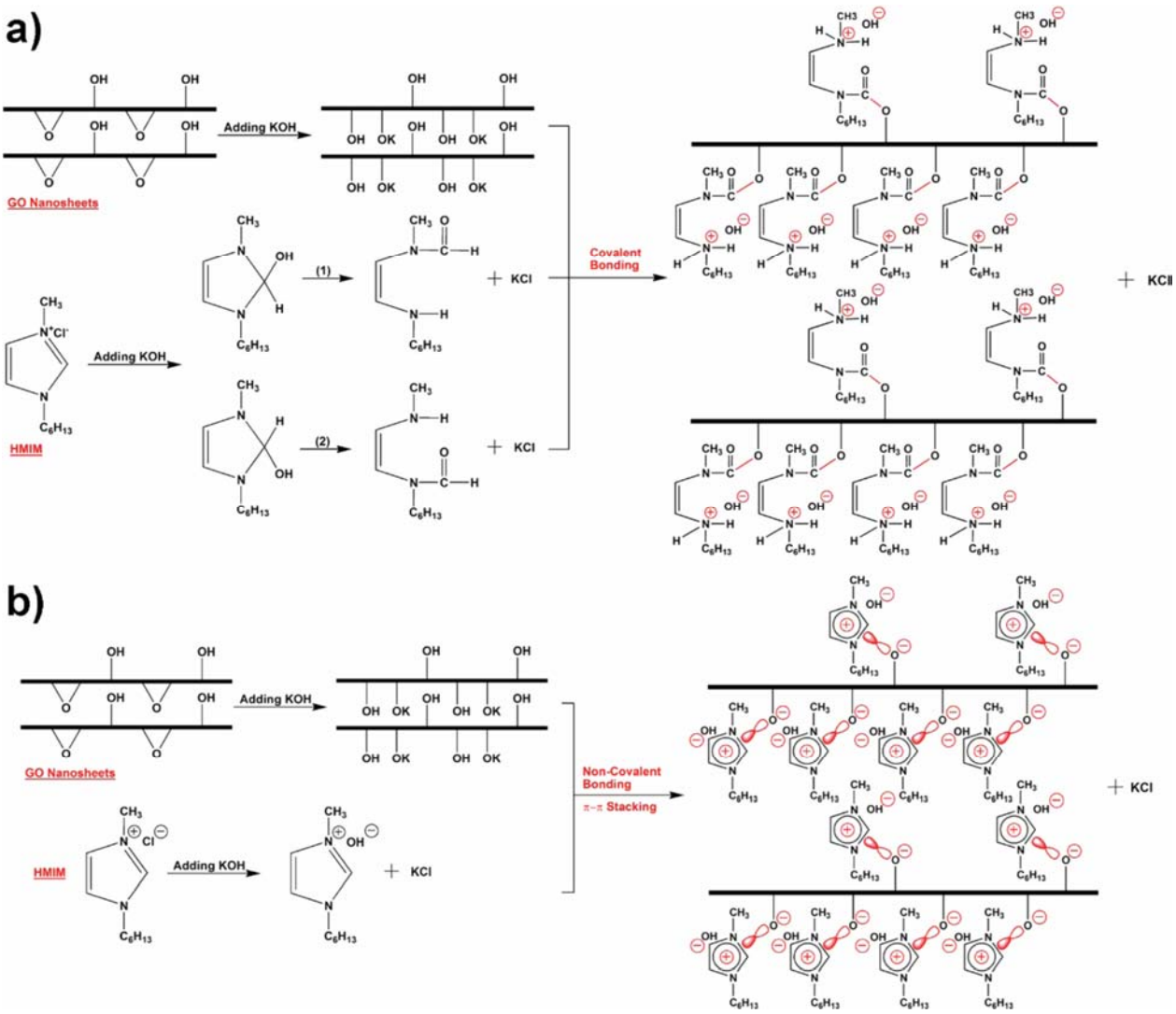

Figure 4-8. Illustrations of (a) covalent and (b) noncovalent bondings of HMIM to GO nanosheets.

According to the outcomes from FT-IR and XPS two possible functionalization mechanisms are proposed in **Figure 4-8**, both of which may have occurred simultaneously. The first suggested mechanism is based on the covalent bonding between the imidazolium ring and GO nanosheets *via* a nucleophilic ring-opening reaction with epoxy and hydroxyl groups under alkaline conditions. According to **Figure 4-8a**, the carbon connecting two pyridinic nitrogen atoms in the imidazolium ring of HMIM can be nucleophilic-attacked by a hydroxyl ion, changing the double bond between the nitrogen and carbon to a single bond.[145] As a result, two transient carbinolamine isomers, amine chains, and KCl salt are produced. KOH attacks GO by reacting

with epoxy groups, generating hydroxyl groups and potassium ions weakly bound to the epoxide, accessible for being reacted with HMIM.[146, 147] The hydroxyl groups on GO donate protons to HMIM which reacts with the amine chains producing secondary ammonium cations capable of conducting hydroxides. Subsequently, the carbinolamine isomers react with the formed oxyanions on the GO surface, generating carboxylate esters which covalently bind the ring-opened HMIM to GO. The significant increase in the intensity corresponding to the carboxylic, carbonyl, and hydroxyl peaks in C 1s (**Figure 4-7b**) and O 1s (**Figure 4-7d**) XPS spectra strongly supports the proposed functionalization mechanism through the covalent bonding of HMIM with GO nanosheets. Another hypothesis for the functionalization mechanism could be based on the noncovalent bonds between HMIM and GO nanosheets in an alkaline medium (**Figure 4-8b**). Since N=C and N−C−N bonds did not disappear in the FTIR and XPS spectra, it can be concluded that in addition to the ring-opening reaction of HMIM with GO, the HMIM itself still exist in the freestanding membranes. In that case, the cationic imidazolium groups in HMIM can electrostatically interact with negatively charged GO nanosheets and induce the $\pi_{cation}-\pi$ stacking between HMIM and GO nanosheets.[148] This not only keeps the layers stacked together in the freestanding membrane but also highly favors the conduction of hydroxide ions *via* the cationic HMIM along and throughout the layers. It is expected that the covalent and noncovalent bindings of HMIM to GO nanosheets exist concurrently and both attribute to the conduction of hydroxide ions in the freestanding x-HMIM/GO membranes.

4.3.3 Ion Conductivity Measurements

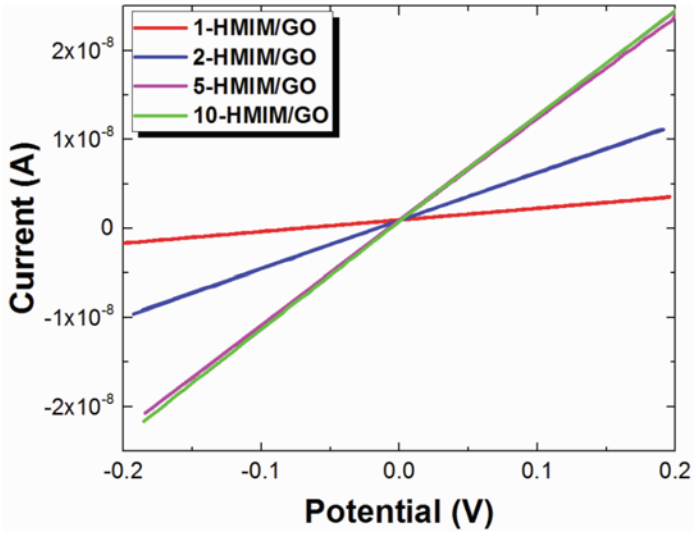

Figure 4-9. I–V plots of the x-HMIM/GO membranes at both 30 and 90% RH and room temperature conditions.

Table 4-3.The calculated electrical resistance (from I-V plots in Figure 4-9) and conductivity (from Equation (3-11)) for x-HMIM/GO membranes.

Membrane	Electrical resistance (ohm)	Electrical conductivity (S cm-1)
1-HMIM/GO	7.64×10^{7}	9.82×10^{-6}
2-HMIM/GO	1.86×10^{7}	4.04×10^{-5}
5-HMIM/GO	8.49×10^{6}	5.89×10^{-5}
10-HMIM/GO	8.36×10^{6}	3.42×10^{-5}

To ensure that the membranes exhibit a high electrical resistance and will not short a practical cell, all x-HMIM/GO membranes were inspected. GO itself is an electron insulator because of the existence of oxygenated functional groups on its basal plane and edges as well as having distorted sp^3 hybridization.[149] In order to investigate if the GO-based membranes have maintained their electron insulation properties after HMIM functionalization, we have measured their electron conductivities from the current vs. voltage (I-V) plots. The I–V plots (**Figure 4-9**) were recorded at room temperature in both wet and dry conditions by varying the voltage between ±0.2 V. The slopes of the linear I-V curves in **Figure 4-9** and **Equation (3-11)** were used to calculate the electronic resistance and electron conductivities of the HMIM/GO membranes, respectively. All calculated results are demonstrated in **Table 4-3**. All HMIM/GO membranes have extremely high electron resistance and electron-insulating behaviour.

Although the increase of HMIM/GO weight ratio from 1 to 10 has increased the slope of the I-V curves and thus decreased the electronic resistance from 7.64×107 to 8.36×106 ohms, the 10-HMIM/GO membrane still exhibits a high electron-insulating behavior. This test confirms the electron insulation of all HMIM/GO membranes to be used as solely ion-conducting EMs in Zn-air battery and supercapacitors.

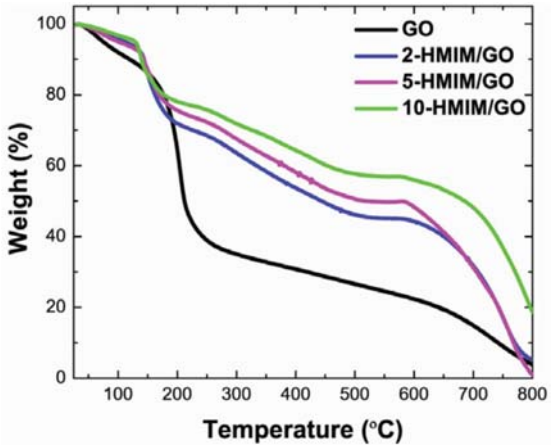

Figure 4-10. The TGA comparison between the free-standing GO and x-HMIM/GO membranes.

For evaluating the performance of the membranes, the free-standing GO and x-HMIM/GO membranes will be compared based on three key parameters, which are comprised of temperature, RH and mass loading of HMIM. Since the hydroxide conductivities of x-HMIM/GO membranes are considered up to an elevated temperature of 50 °C, thermogravimetric analysis (TGA) was performed (**Figure 4-10**) to assess their thermal stability. Before running the test, the samples were preserved at room temperature and 30 %RH in a humidity chamber for 2 h. The TGA for GO and all *x*-HMIM/GO membranes are divided into three and four different zones, respectively. The weight loss in zone one was related to the water evaporation which was calculated ~14% for the GO membrane in the range of 30-150 °C, ~6% for 2- and 5-HMIM/GO, and ~4% for 10-HMIM/GO membranes occurred between 30 °C to 114 °C. The smaller amount of water loss in *x*-HMIM/GO membranes indicated to a lesser tendency of GO membrane to absorb water molecules after functionalization. In the second zone, the weight loss for the GO membrane was between 150 °C to 250 °C, whereas that took place from 114 to 200 °C for *x*-HMIM/GO membranes. That weight loss was caused by the decomposition of the unstable oxygen-containing functional groups which was 48%, 23%, 19%,

and 18% for the GO, 2-HMIM/GO, 5-HMIM/GO, and 10-HMIM/GO membranes, respectively.[139] By increasing the degree of functionalization, more oxygenated groups were involved in the ring-opening reaction. In zone three, a 15% weight loss was observed for the free-standing GO membrane between 250 °C and 570 °C which was attributed to the removal of more stable oxygen groups.[139] In this zone, the mass of *x*-HMIM/GO membranes started to decrease from 200 °C to 580 °C, which were about 26%, 25%, and 21% for 2-HMIM/GO, 5-HMIM/GO, and 10-HMIM/GO, respectively. This mass disappearance for *x*-HMIM/GO membranes was due to the bonded HMIM groups beginning to disassociate from the GO surface. In the last zone the sharp weight-loss of *x*-HMIM/GO membranes after 580 °C are assigned to the complete removal of HMIM groups.[150-152] According to TGA results, the functional groups started to degrade after 200 °C, which guarantees the high thermal endurance of each membrane at the temperatures of interest.

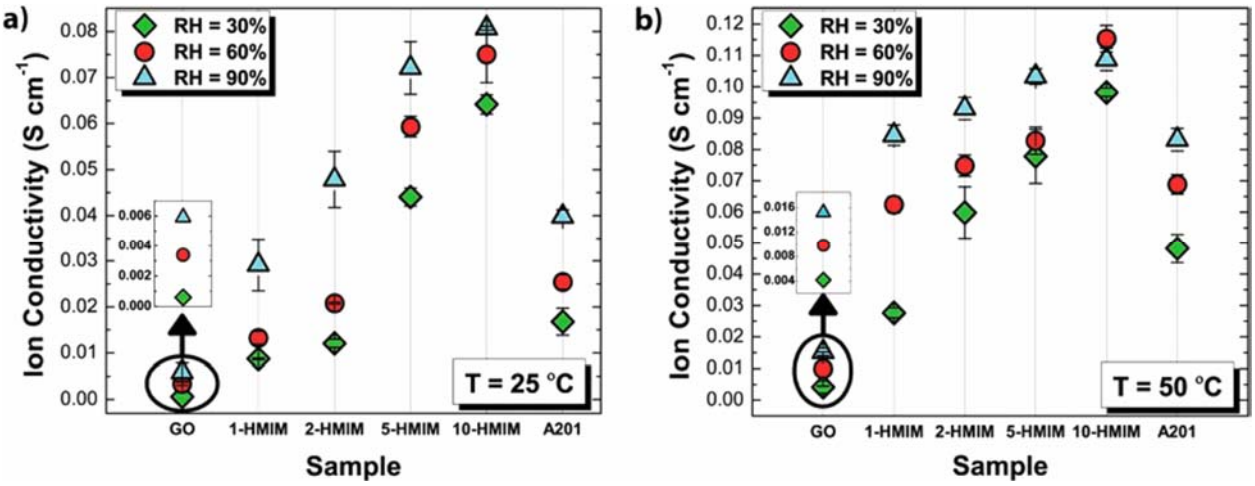

Figure 4-11. In-plane hydroxide conductivity of A201 from Tokuyama, the freestanding GO membrane, and freestanding x-HMIM/GO membranes in different RH at (a) 25 °C and (b) 50 °C.

Finally after verifying the prerequisites of using the membranes as EMs, **Figure 4-11** presents the in-plane hydroxide conductivity of the freestanding GO and x-HMIM/GO membranes, and a reference comparison to that of the commercial A201 membrane from Tokuyama. In the case of the commercial A201, the measured hydroxide conductivity, at room temperature and 90% RH, was similar to that reported in literature,[153] *i.e.*, ~0.04 S cm^{-1} (**Figure 4-11a**). Considering the pristine GO membrane, where its ion conduction is highly dependent on

the presence of water molecules, amongst the considered membranes, it exhibited the lowest ion conductivity of 0.000589 S cm^{-1} at 25 °C and 30% RH. When the RH increased to 60% and 90%, the conductivity of the GO notably increased by 5.8 and 10.1 times. At high RH, multilayer physical adsorption of water molecules occur through hydrogen bonding on the hydroxyl groups of GO.[154] Moreover, the OH and COOH groups became ionized, and thereby contributing hydronium charge carriers.[34, 154, 155] In addition, the strong dependency of the ionic conductivity on temperature change (**Figure 4-11b**) demonstrates the high sensitivity to the operating conditions in A201 membrane. The obtained results for ion conduction in pristine GO and A201 membranes is indicative of their performance dependency on the operating conditions, which limits their practical application for wearable energy-storage devices. Post-HMIM-functionalization, for both 25 and 50 °C (**Figure 4-11**), raising RH from 30% to 90% increased the hydroxide conductivity by ~3.5 times at the two lower HMIM loadings (*i.e.* 1-HMIM/GO and 2-HMIM/GO), whereas for the two higher HMIM loading (*i.e.* 5-HMIM/GO and 10-HMIM/GO) increased merely ~1.5 times. This effect can be linked to the increased interlayer spacing of GO nanosheets functionalized with HMIM groups.

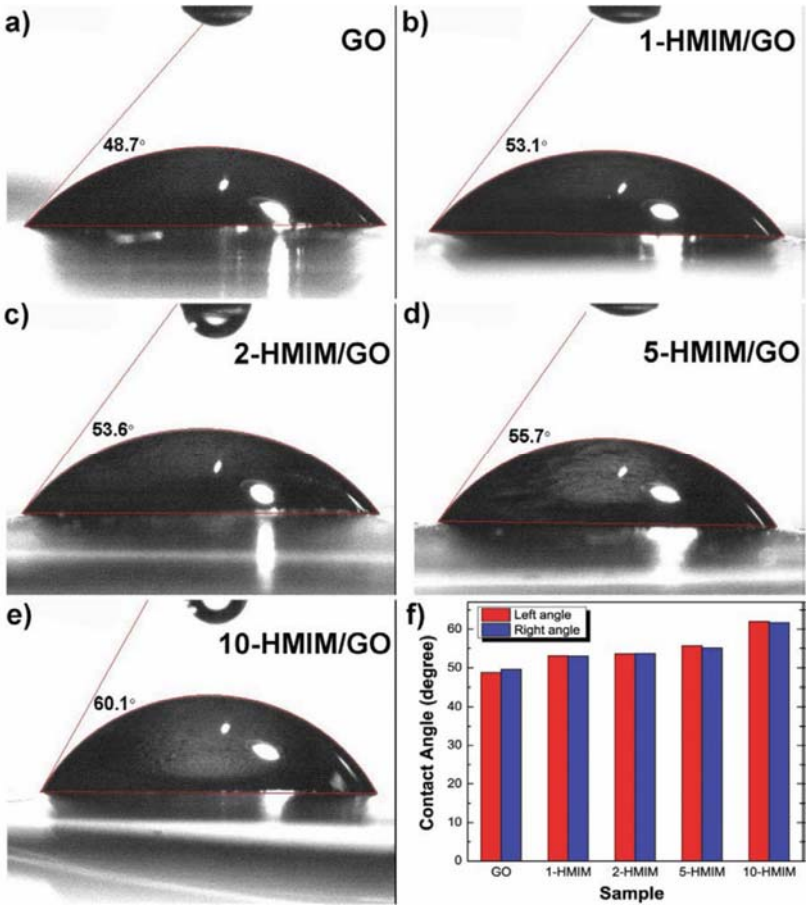

Figure 4-12. Water contact angle images of free-standing a) GO, b) 1-HMIM/GO, c) 2-HMIM/GO, d) 5-HMIM/GO, and e) 10-HMIM/GO membranes. f) The comparison between left and right water contact angles in all free-standing membranes.

To evaluate any variation in the hydrophilicity of the GO membrane after being functionalized with HMIM, the water contact angle on the surface of all membranes was measured and displayed in **Figure 4-12a-e**. For this purpose, a droplet of water (about 7 µL) was laid onto the surface of all samples and the images were captured using a charge-coupled device camera. Contact angles below 90° exhibit the hydrophilic feature of a sample. The digital images of water drops revealed that the loading increase of HMIMI has increased the water contact angle, denoting the decrease of hydrophilicity of *x*-HMIMI/GO membranes. As shown in **Figure 4-12f** both left and right contact angles for all free-standing membranes were equal, expanding from 48.7° to 60.1° by increasing the weight ratio of HMIMI to GO from 1 to 10.

Although doped with low concentrations of HMIM, yet some oxygenated groups persist on the GO surface, the distance between nanosheets increased and favor the extra absorption of water molecules at higher RH, which can facilitate ions transfers and notably increase the hydroxide conductivity. When the HMIM loading increases, most of the oxygenated groups (*e.g.* epoxy and hydroxyl) are involved in the formation of either covalent or noncovalent bondings with HMIM (**Figure 4-8**), which then negatively affects the water absorption. The reduction of hydrophilicity in GO *via* increasing the loading of HMIM has been shown by the incremental increase of the water contact angle from 48.7° for GO to 60.1° in 10-HMIM/GO membrane (**Figure 4-12**).

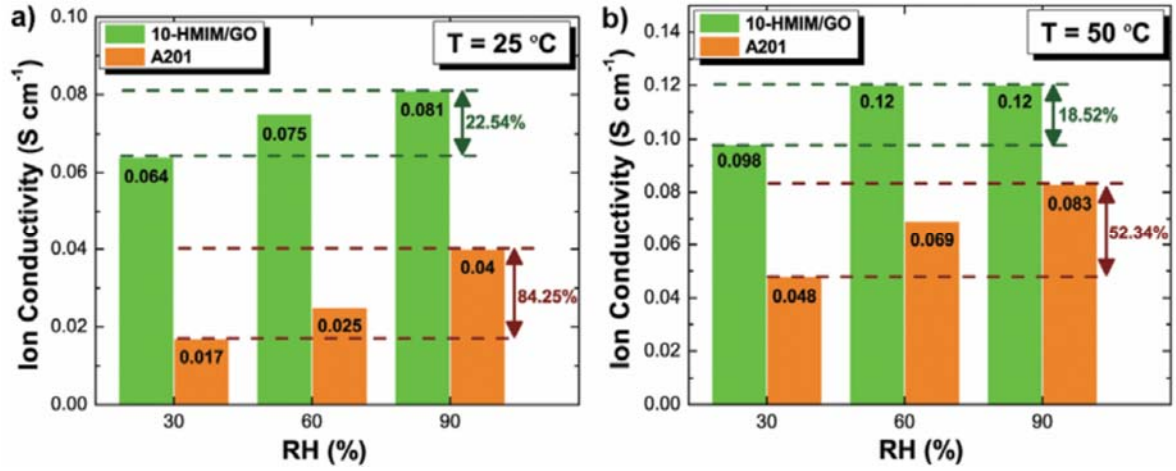

Figure 4-13. Sensitivity of ion conductivity in 10-HMIM/GO and A201 membranes to RH change at the temperature of a) 25 °C and b) 50 °C.

However, since HMIM itself is an ion-conductive ionic liquid with minor dependency on a humid medium, a higher degree of that in GO not only boosts the hydroxide conductivity at lower RH but also effectively decreases the performance sensitivity to the operating conditions. For example, at a low RH of 30% and room temperature, the ion conductivity of 10-HMIM/GO membrane was 3.8 times higher than that of commercial A201. By changing RH from 30% to 90%, the hydroxide conductivity of 10-HMIM/GO varied only 23% and 19% at 25 and 50 °C, respectively, whereas that of A201 membrane underwent a dramatic change of 84% and 52% at the same conditions (**Figure 4-13**).

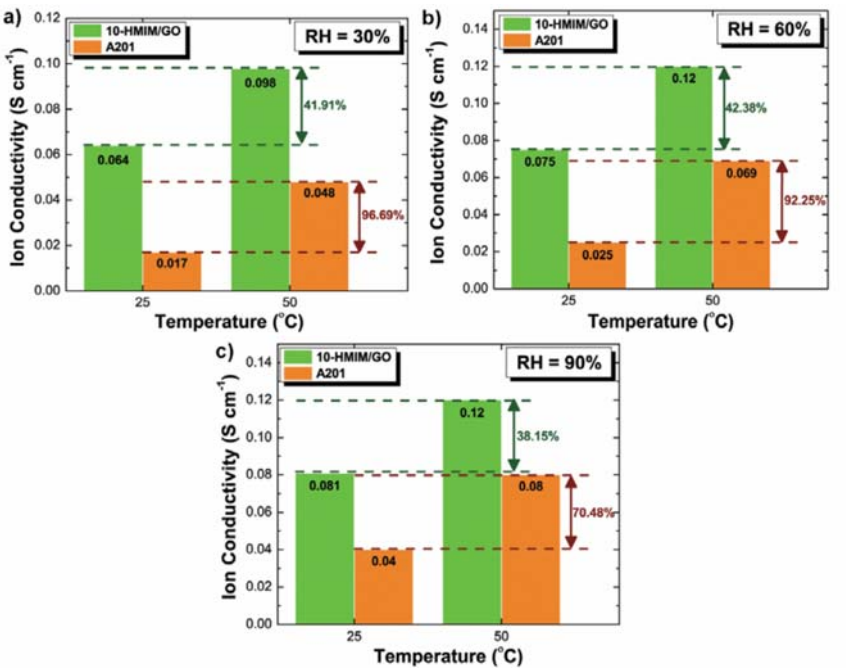

Figure 4-14. Sensitivity of ion conductivity in 10-HMIM/GO and A201 membranes to the temperature change at RH of a) 30%, b) 60%, and c) 90%.

Likewise, the impact of temperature increase from 25 to 50 °C on the rate of ion transfer in 10-HMIM/GO membrane was ~50% less than that in commercial A201 (**Figure 4-14**).

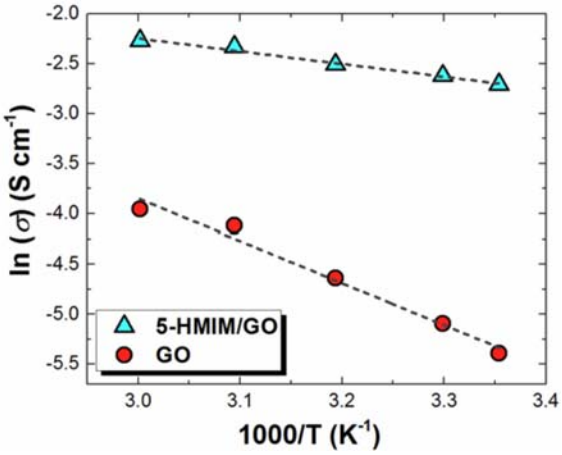

Figure 4-15. Arrhenius plots showing the natural logarithm of hydroxide conductivity vs. the reciprocal of temperature for GO and 5-HMIM/GO membranes.

To determine the mechanism of hydroxide conduction in HMIM/GO membrane, the activation energy (E_a) for ion-migration in both GO and 5-HMIM/GO membranes is calculated. To perform the test, first, the samples are equilibrated at room temperature and 60% RH, and then their in-plane ion conductivities are measured at 25, 30, 40, 50, and 55 °C. Assuming an Arrehnius behaviour (**Equation (3-12)**), E_a is measured from the slope of linear regression of natural logarithm of ion conductivity (ln σ) vs. the reciprocal of the temperature (1000/T) as plotted in Figure S7. As shown in Figure S7, the E_a for GO and 5-HMIM/GO membranes are about 34.92 and 10.56 kJ mol^{-1}, respectively. The E_a of 5-HMIM/GO is also compared to that of the commercial A201 membrane (*ca.* 11.26 kJ mol^{-1}) as reported in literature and our previous work.[156, 157] Compared to GO and A201, the lower E_a of 5-HMIM/GO implies the dominance of Grotthus mechanism rather than vehicle mechanism in the membrane. The hypothesized mechanism can be highly supported by the minor sensitivity of hydroxide migration to temperature and RH in 5-HMIM/GO membrane. From these derived values, the minor sensitivity of hydroxide migration to temperature and RH in HMIM/GO membranes can be approved by the dominance of Grotthus mechanism rather than vehicle mechanism in the membranes (**Figure 4-15**).[158, 159]

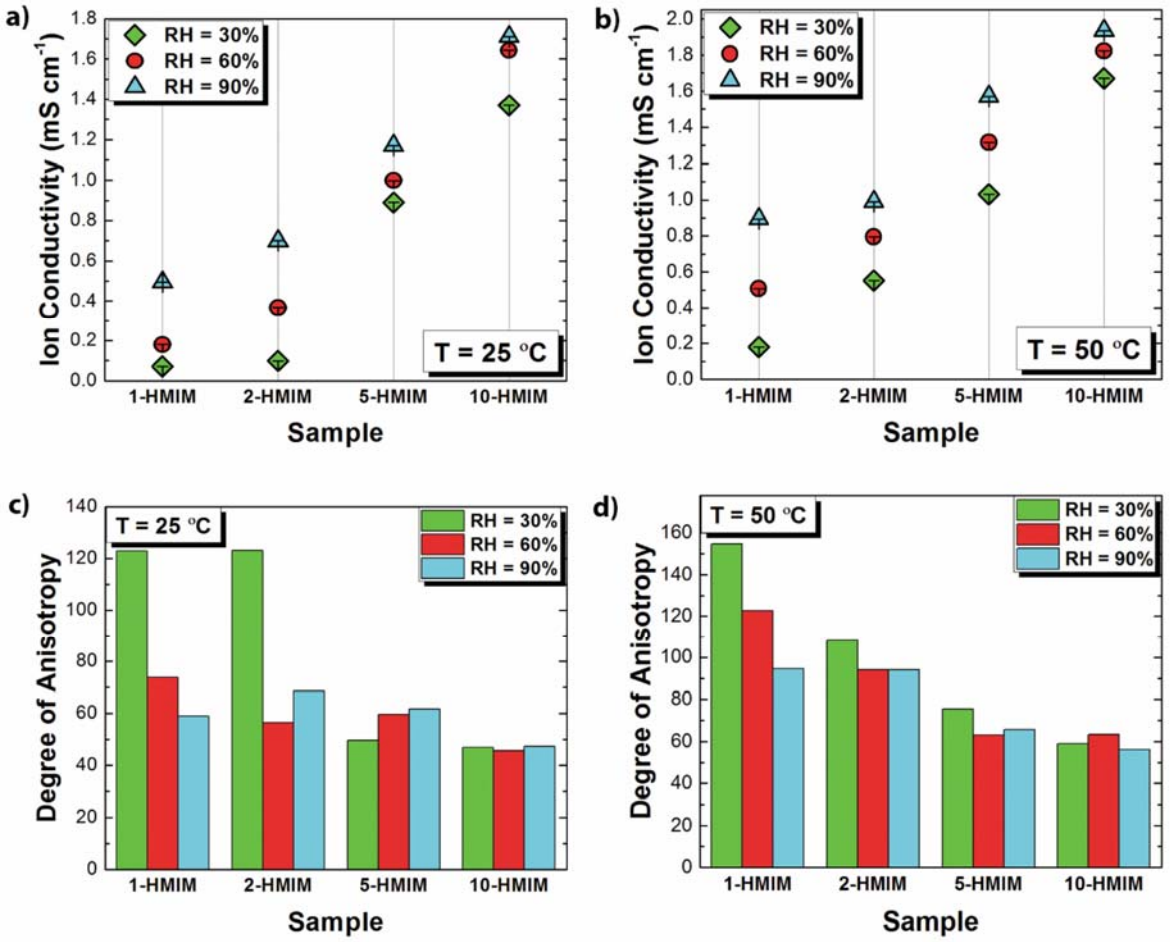

Figure 4-16. The through-plane hydroxide conductivity of freestanding x-HMIM/GO membranes in different RH at a) 25 °C and b) 50 °C. Degree of anisotropy for x-HMIM/GO membranes in different RH at c) 25 °C and d) 50 °C.

These results are highly supportive to the development of wearable energy-storage systems where the performance dependency on the operating conditions would otherwise restrain their long-term application and reliability. The through-plane hydroxide conductivities of all x-HMIM/GO membranes are shown in **Figure 4-16a, b**. Depending on the HMIM loading in GO, the through-plane conductivity has dropped about 1−2 orders of magnitude when compared to their in-plane conductivity. The resulted differences between in-plane and through-plane conductivities arise from two main reasons. First, in the through-plane arrangement (*i.e.*, through the thickness) L in **Equation (3-11)** corresponds to the membrane thickness, in the range of micrometers, and A is the (flat) area of the electrodes, which is generally much larger than the thickness. Thus, opposed to in-plane direction, the dimensional ratio (*i.e.* L/A) is very

small, and the impedance contributions from the interfacial region between the membrane and the electrodes become more restrictive.[160, 161] The other factor causing the discrepancy between the in-plane and through-plane ion conductivities in membranes may arise from variations in material's physical properties at its microstructural orientations, called morphological anisotropy. Depending on the similar or different ionic conductivity value in each direction, the membrane can be considered as an either isotropic or anisotropic material, respectively. To evaluate that, a degree of anisotropy must be defined, which is the ratio of the in-plane to the through-plane conductivity. According to the obtained results **(Figure 4-11 & Figure 4-16a, b)**, the degree of anisotropy was calculated and tabulated in **Figure 4-16c, d**. By increasing the loading of the HMIM functional groups in GO (*e.g.* 5-HMIM/GO and 10-HMIM/GO), the degree of anisotropy decreased significantly, which supported the faster ion transfer through the thickness of the HMIM/GO membranes. This may stem from the existence of a more uniform microstructural morphology in both directions of 5-HMIM/GO and 10-HMIM/GO membranes, as conferred by XRD and Raman results. As revealed in the XRD (**Figure 4-5a**) and Raman spectra (**Figure 4-5b**), the increased loading of HMIM functional groups reinforces the exfoliation of GO nanosheets and disorderly spacing between the stacked interlayers. Accordingly, the crystallinity decreased, which creates higher ion mobility in all dimensions of highly loaded HMIM/GO membranes.

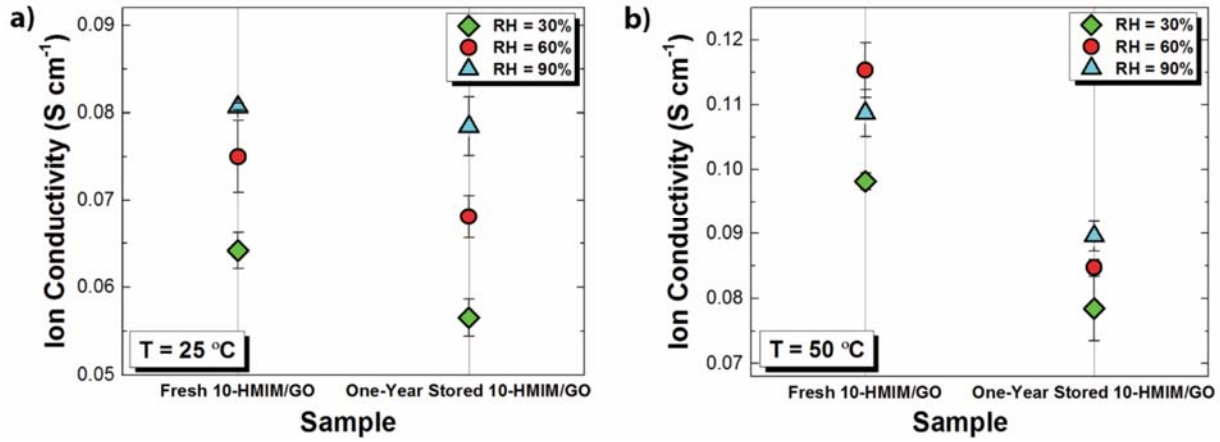

Figure 4-17. Durability of Hydroxide Conduction in a one-year stored 10-HMIM/GO membrane at different RH and temperatures of a) 25 °C and b) 50 °C

As the sustainability of hydroxide conduction over a period of time is of great importance for wearable electronics, the hydroxide conductivity of a one-year-stored 10-HMIM/GO

membrane was also re-measured and compared to a freshly made sample in **Figure 4-17**. According to **Figure 4-17a**, at room temperature, the hydroxide conductivity of a one-year-stored 10-HMIM/GO membrane decreased about 11.8, 9.2, and 2.8% at RH of 30, 60, and 90%, respectively. At 50 °C (**Figure 4-17b**) the conductivities also decreased about 20, 26.5, and 17. 6% at RH of 30, 60, and 90%, respectively.

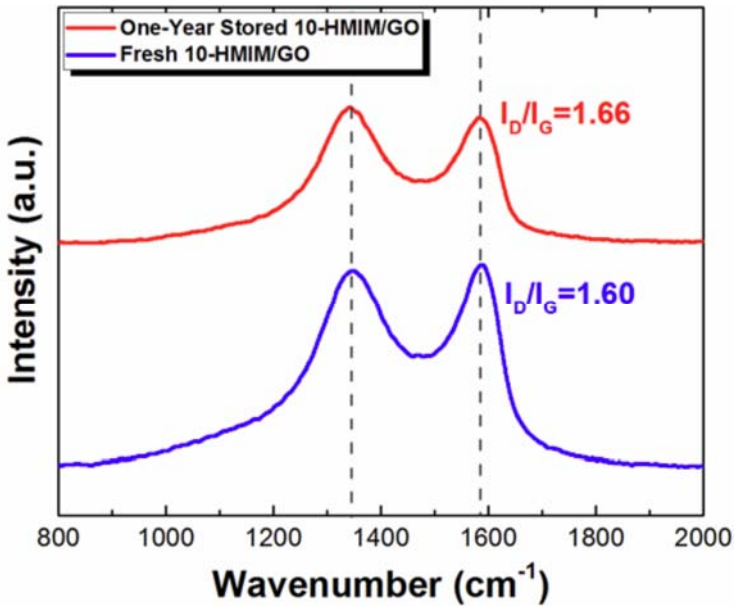

Figure 4-18. The Raman spectrometry of the one-year stored 10-HMIM/GO membrane

The slight reductions in the conductivities in the one-year-stored 10-HMIM/GO could be attributed to the increased defects on the surface of HMIM/GO based on the Raman spectrum in **Figure 4-18**. This may have occurred due to the exposure of 10-HMIM/GO membrane to ambient room conditions for one year. In spite of the minor performance decrease, the hydroxide conductivity of the HMIM/GO membrane is sufficiently high enough to maintain the performance for energy-storage systems at different environmental conditions.

4.3.4 Electrochemical Characterization

In order to affirm the applicability of freestanding x-HMIM/GO membranes in wearable energy-storage systems, flexible Zn−air battery and supercapacitor were fabricated using 5-

HMIM/GO membrane as the hydroxide-conductive solid electrolyte and was also compared to those made from the commercial A201 polymeric membrane from Tokuyama. Similar to other alkaline electrochemical devices, Zn−air batteries and alkaline supercapacitors suffer from the major limitations caused by the aqueous KOH electrolyte such as evaporation, carbonation, operating temperature, alkaline corrosion, safety, and electrochemical stability,[119, 162] which dramatically restrict their applications in wearable electronics. Accordingly, replacing the aqueous alkaline electrolytes with a solid-state, thin, and flexible membrane can not only address the aforementioned issues, but also provide a lightweight alternative.

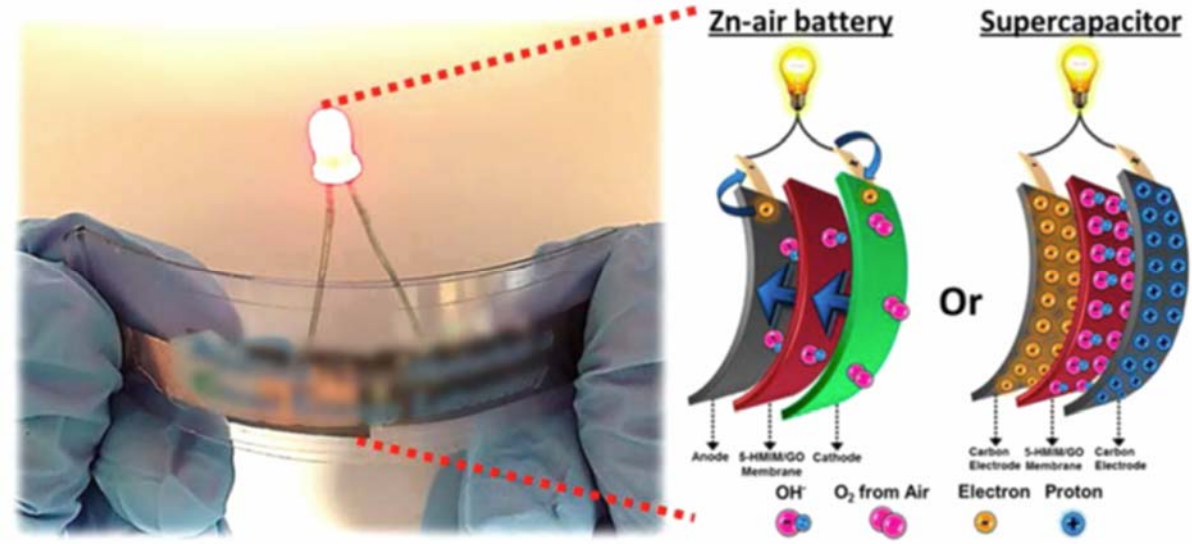

Figure 4-19. Picture of a flexible electrochemical energy storage device containing the freestanding 5-HMIM/GO membrane as the solid hydroxide conductive EM. The energy storage system could be either a Zn-air battery or a supercapacitor.

As shown in **Figure 4-19**, the fully solid-state, flexible, and lightweight zinc−air battery and supercapacitor were fabricated by sandwiching a 27 μm freestanding 5-HMIM/GO electrolyte membrane between either (i) a Zn pellet anode and a bifunctional Co_3O_4 cathode for the Zn−air cell or (ii) two carbon-coated electrodes for the supercapacitor.

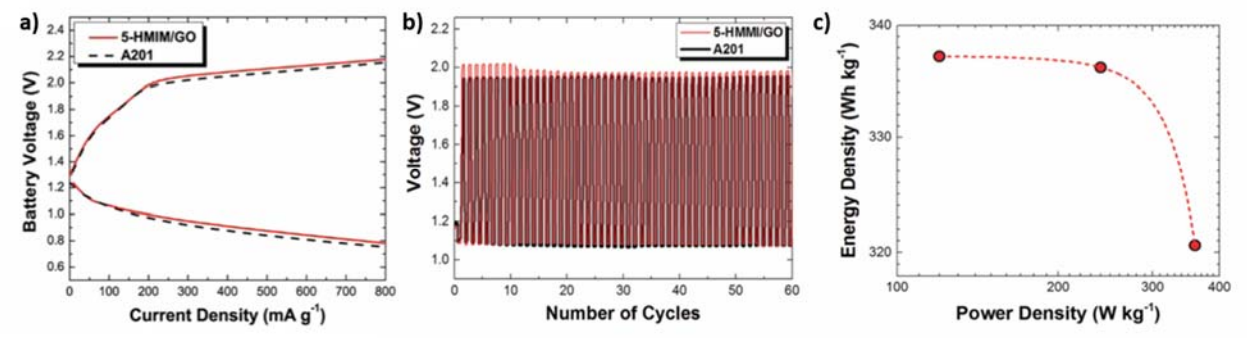

Figure 4-20. a) Charge/discharge polarization curves, and b) galvanostatic charge and discharge cycling at a current density of 200 mA g^{-1} with a 10 min cycle period, of Zn-air batteries made of a freestanding 5-HMIM/GO membrane and the commercial A201. c) The Ragone plot for 5-HMIM/GO Zn-air battery.

Figure 4-20a exhibits the cell potential change of the solid-state Zn−air battery possessing low humidified 5-HMIM/GO membrane during discharge and charge as a function of current density compared to that of a fully humidified A201 polymeric membrane (28 μm) from Tokuyama at room temperature. While discharging the battery, the open-circuit voltage (OCV) for both membranes was about 1.25 V. Despite operating at a lower humidity than A201, the Zn−air battery made of freestanding 5-HMIM/GO membrane has exhibited a larger discharging current density than that of A201. For example, at 0.8 V, the discharging current density of the battery equipped with 5-HMIM/GO membrane was 1.2 times higher than that with a fully-humidified A201 membrane. This can be associated to the superior hydroxide conductivity of 5-HMIM/GO membrane (at low RH) than that of A201 (at higher RH and temperature) (**Figure 4-11**). However, a fully humidified A201 showed a slightly better charging current density compared to low-RH 5-HMIM/GO membrane; at 2 V, the charge current density of A201 was about 1.2 times higher than that of 5-HMIM/GO. Furthermore, to review the cycling performance of batteries, the galvanostatic charge and discharge of 5-HMIM/GO and A201 Zn−air batteries have been evaluated in **Figure 4-20b**. Both membranes exhibit stable charge/discharge performances for 60 cycles. The comparable cycling stability of 5-HMIM/GO at 50% RH to A201 at 100% RH confirms its pragmatic functionality at low RH and room temperature conditions to provide adequate service as a solid-state, flexible battery, especially in drier climates. Moreover, the long cycling stability of 5-HMIM/GO at 50% RH is higher than that of many reported solid EMs in the literature, which were tested at the more favourable 100% RH.[163, 164] A Ragone plot have also been generated for the 5-HMIM/GO Zn−air battery (**Figure 4-20c**) to assess the effect of discharge rate on the energy density decay of the battery. In order to generate the

Ragone plot, the 5-HMIM/GO contained Zn-air battery was completely discharged at three different current densities, of 100, 200, and 300 mA g^{-1}, to measure the specific energy density at different discharge rates. Despite the large increase of specific power density, from 120 to 360 W kg^{-1}, the specific energy density of the Zn−air cell has merely dropped 16.6 Wh kg^{-1}. The high sustainability of the specific energy density can be attributed to the stable hydroxide conductivity of 5-HMIM/GO membrane during discharge, which prevents the rapid polarization of the zinc electrode as conventionally occurs in Zn−air cells using liquid KOH electrolytes. According to the presented Ragone plot, the minor performance sensitivity to the surrounding RH and temperature in 5-HMIM/GO membrane demonstrates the feasibility of replacing KOH liquid electrolytes with reliable solid EMs for upcoming Zn−air batteries.

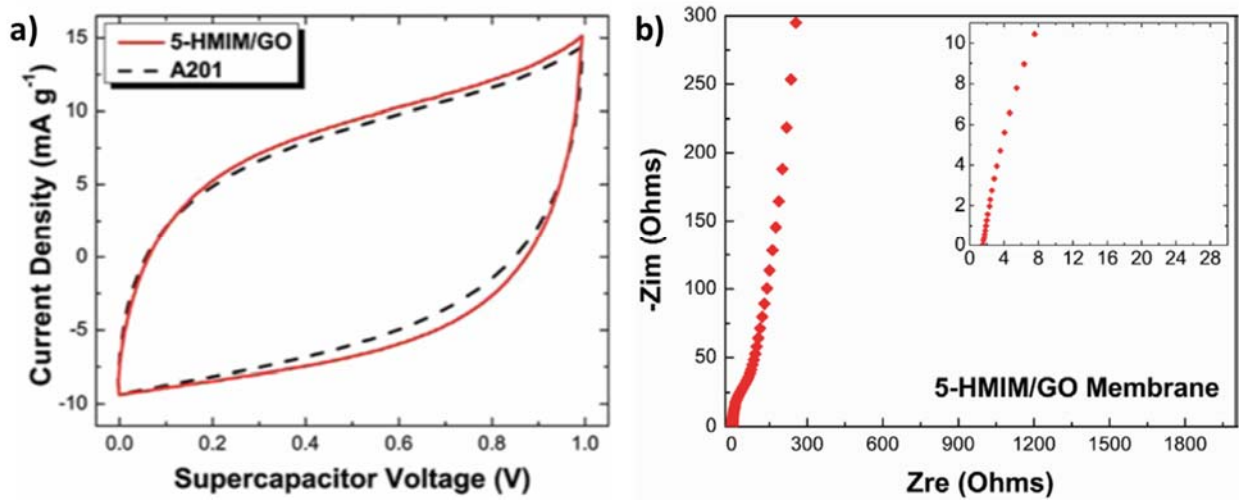

Figure 4-21. a) CV curve of supercapacitors made of a freestanding 5-HMIM/GO membrane and the commercial A201 at a scan rate of 0.2 V s^{-1}. b) The EIS curve of the supercapacitor containing 5-HMIM/GO membrane.

Figure 4-21a compares the CV of the supercapacitors equipped with a fully-humidified A201 against the low-RH 5-HMIM/GO membrane at a scan rate of 0.2 V s^{-1}. The CVs are virtually rectangular showing that both solid EMs have low ionic transfer resistances, additionally justified by the electrochemical impedance spectroscopy (EIS) analysis in the **Figure 4-21b**. At the high-frequencies the low intrinsic resistance, represented by the x-intercept, represents a low internal resistance within the supercapacitor. This confirms the high ionic conductivity of the 5-HMIM/GO membrane at room temperature and low RH conditions. At low frequencies, since

the imaginary portion of the impedance approaches the infinity with a close phase angle shift to 90°, it can be concluded that using 5-HMIM/GO electrolyte membranes favor the flexible supercapacitors to act as an ideal capacitor without being dependent on the level of water in system. The low ionic transfer resistance in the low humidified 5-HMIM/GO is presumed to have originated from the incorporated HMIM groups, which increased the interlayer spacing and ionic conductivity without any dependence on the RH level. However, for the fully humidified A201, the low ionic transfer resistance stemmed from the existence of absorbed water molecules in the polymeric backbone of A201 and thus, the increased mobility of ions.

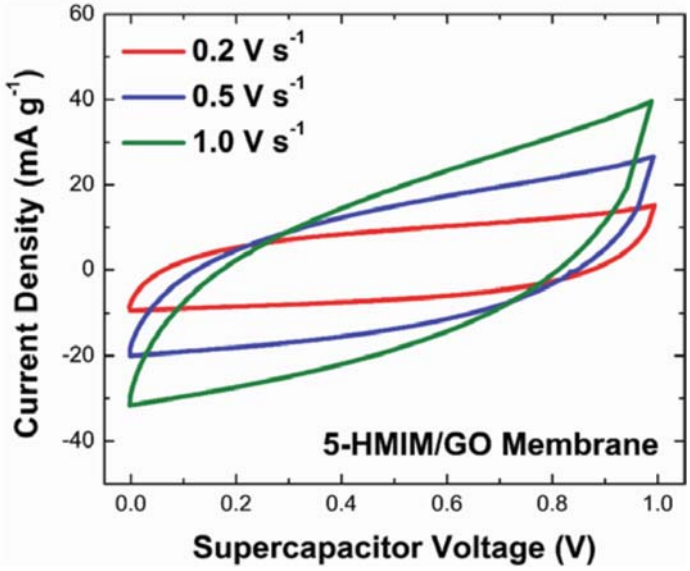

Figure 4-22. The CV curve of the supercapacitor containing 5-HMIM/GO membrane at scan rates 0.2, 0.5, and 1 V s^{-1}.

These results remained consistent with **Figure 4-22**, which showed the ionic mobility was still high albeit varying the CV scanning rates. The CV almost maintains its rectangular shape suggesting that the low humidified 5-HMIM/GO membrane maintains a low ionic transfer resistance, even at higher scan rates. At a scan rate of 0.2 V s^{-1}, the capacitances were calculated at 0.065 and 0.069 F cm^{-2} for the supercapacitors equipped with fully humidified A201 and low humidified 5-HMIM/GO membranes, respectively.

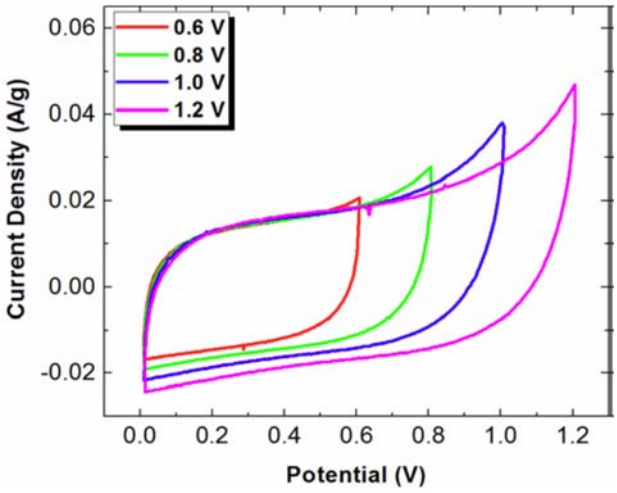

Figure 4-23. The CVs of a symmetric 5-HMIM/GO supercapacitor with different potential windows at a scan rate of 0.2 V s^{-1}.

The operational voltage window for the 5-HMIM/GO supercapacitor was measured by calculating the gravimetric capacitance at certain voltage windows (**Figure 4-23**) using the cyclic voltammetry (CV) at the scan rate of 0.2 V s^{-1}. The gravimetric capacitance consistently increased as the voltage window increased. The evaluated voltage window for the 5-HMIM/GO supercapacitor demonstrated a stable operational window up to 1.2 V. However, since most supercapacitors are operated in the range of maximum voltage (V_{max}) and half of V_{max},[165] 0 – 1 V can be selected as a safe operational voltage window for 5-HMIM/GO supercapacitors to buffer against any absorbed water electrolysis reactions at ~1.23 V. These results confirm that freestanding HMIM/GO membranes are considerably functional at low RH and room temperature, which can provide adequate operation for a solid-state, flexible battery or supercapacitor, without the need to be humidified.

Table 4-4. Comparison of hydroxide conductivity and device performance at Room Temperature (unless specified) within Zn-air batteries

Solid Electrolyte Membrane	Ion conductivity (S cm^{-1})	Device Performance *via* Power Density	Testing RH (%)	Reference
P(ECH-co-EO)	0.001 0.005 at 90 °C	14 mW cm^{-2}	100	[164]
S-PP/PE	0.018	27 mW cm^{-2}	100	[166]
PVA/PAA	0.3 0.5 at 80 °C	50 mW cm^{-2}	100	[167]
Sulfonated PPf	0.035	38 mW cm^{-2}	100	[168]
GGPE	0.0031	9h discharge at 0.92 V and 0.1 mA cm−2	100	[117]
PVA/PEO/KOH	0.3	12h discharge at 1 V and 1 A g−1	100	[163]
QAFCGO	0.033 0.058 at 70 °C	44.1 mW cm^{-2}	100	[169]
5-HMIM/GO	0.044 0.078 at 50 °C	35.12 mW cm^{-2}	30	This work

Table 4-5. Comparison of hydroxide conductivity and device performance at Room Temperature within alkaline solid supercapacitors

Solid Electrolyte Membrane	Ion conductivity (S cm^{-1})	Device Performance *via* Capacitance	Testing RH (%)	Reference
GO-B-PVA/KOH	0.2	130.8 F g^{-1} at 0.01 V s^{-1}	100	[170]
PVAPB	0.001	45 F g^{-1} at 0.02 V s^{-1}	100	[171]
5-HMIM/GO	0.044	19.7 F g^{-1} at 0.2 V s^{-1}	30	This work

A literature survey is conducted to compare the performance of HMIM/GO membrane to the so far reported hydroxide-conductive solid EMs in Zn-air batteries and alkaline solid supercapacitors. According to **Table 4-4** and **Table 4-5**, the majority of reported solid EMs are made of KOH-based gel polymer electrolytes such as poly(vinyl alcohol) (PVA), poly(ethylene oxide) (PEO), and polypropylene (PP) with a high concentration of KOH >10 wt%.[172] These membranes has shown hydroxide conductivities of 0.001–0.3 S cm^{-1} when tested at room temperature and 100% RH, showing their strong reliance on the degree of hydration. When used in the battery or supercapacitors, these membranes tend to lose water rapidly by evaporation since the electrodes are exposed to the atmosphere. This leads to a fast degradation of the hydroxide conductivity and the resultant battery and supercapacitor performance. As Zn-air batteries and supercapacitors are used in portable and wearable

electronics, the limited operating window of these membranes greatly restrict their application and reliability in different environmental conditions and climates. This comparison approves the high potential of HMIM/GO to be functional at different operating conditions, especially low RH, which is highly important for the reliability of wearable electronics to be used in dry climates.

4.4 Chapter Conclusion

In this chapter, in order to minimize the performance dependence of wearable electronics to the operating environment, a flexible GO electrolyte membrane was functionalized with HMIM molecules *via* esterification reaction. According to the spectrometric analyses, we postulated two different functionalization mechanisms that simultaneously occur including (i) the covalent bonding of ring-opened HMIM to the ring-opened epoxide and hydroxyl groups on the GO and (ii) the electrostatic interaction of cationic imidazolium groups in HMIM with negatively charged GO nanosheets. Compared to a pristine GO membrane and the commercial A201 membrane from Tokuyama, the resultant freestanding x-HMIM/GO membranes demonstrated not only significantly higher hydroxide conductivities at low RH and room temperature conditions but also the minimum performance dependency on the environmental conditions. For instance, the 10-HMIM/GO membrane exhibited a superior and stable hydroxide conductivity of 0.064 ± 0.0021 S cm^{-1} at 30% RH and room temperature, which was 3.8 times higher than that of the commercial membrane at similar conditions. Likewise, the hydroxide conductivity of 10-HMIM/GO membrane changed only 22.54% and 41.91% by increasing the RH to 90% (at room temperature) and temperature to 50 °C (at 30% RH), respectively. In contrast to the 10-HMIM/GO membrane, the hydroxide conductivity of A201 membrane was highly dependent on the operating conditions, which changed 84.25% and 96.69% by increasing the RH to 90% (from 30% RH, at room temperature) and temperature to 50 °C (from 25 °C, at 30% RH), respectively. The feasibility of using freestanding x-HMIM/GO membranes in flexible electronics was assessed by assembling 5-HMIM/GO membrane in a solid-state Zn−air battery and a supercapacitor. At room temperature, the charge−discharge voltage polarization of the flexible Zn−air cell and the CV curves of the supercapacitor containing the novel 5-HMIM/GO membrane, at low RH, were comparable to those of the commercial polymeric membrane (*i.e.*, A201), at humidified environment. This achievement is attributed to the high rate of ion transfer at low RH and room temperature conditions favored by the bonded HMIM groups on the surface of GO nanosheets. The results of this chapter discloses the promising potential of manipulating

a freestanding nanomaterial membrane to work as a flexible and lightweight EM in wearable energy storage devices, possessing highly stable performance even at different operating conditions, especially at low RHs and room temperature.

Chapter 5: Near-Isotropic Proton-Conducting Porous Graphene Oxide Membrane

This chapter is adapted with permission from Serubbabel Sy, Gaopeng Jiang, Jing Zhang, Hadis Zarrin, Timothy Cumberland, Salah Abureden, Ellsworth Bell, Jeff Gostick, Aiping Yu, and Zhongwei Chen. Near-Isotropic Proton-Conducting Porous Graphene Oxide Membrane. ACS Nano 2020 Nov 11; 14(11), 14947-19459.

5.1 Introduction

Graphene oxide (GO) is a widely-recognized two-dimensional (2D) atom-thick nanomaterial enriched with abundant oxygenated functional groups on the surface.[4, 173] GO preparation has realized many iterations and evolutionary changes since its inception made by Brodie [3, 174], *i.e.* utilizing chemical methods (*e.g.* chlorate,[175, 176] permanganate,[17, 177-179] *etc.*[180-182]), electrochemical methods,[19, 183] to microbial methods.[184-186] This development has been fueled by the many beneficial characteristics, a combination of which are distinctive of GO. For example, GO nanosheets tend to self-assemble into a thin, laminated membrane during solvent evaporation. Benefitting from the facile functionalization, high aspect ratio of GO nanosheets, and its highly selective, molecular/ionic sieves-like interlayers, the GO membrane can be well applied as an ideal separator for multiple important applications, such as gas separation,[47, 187-189] water treatment,[187, 188, 190-194] and electrochemical energy-storage or conversion devices (*e.g.* batteries, fuel cells, supercapacitors, solar cells, *etc.*).[56, 195-197] More notably, the high aspect ratio of nanosheets enables the GO membrane with typical anisotropic transportation properties, including thermal conductivity,[198] electronic conductivity,[199, 200] and water permeability.[47, 187, 201-203] Accordingly, the ionic conductivities of a GO membrane, mainly proton conductivity and hydroxide ion conductivity, are also found to be anisotropic, favoring the in-plane direction rather than the through-plane.[44, 56, 126] The ratio of in-plane proton conductivity ($\sigma_{\parallel}$) over the through-plane one ($\sigma_{\perp}$), *i.e.* the degree of anisotropy ($\sigma_{\parallel}/\sigma_{\perp}$) is reported to range from tens to hundreds for the GO membranes.[39, 40, 204-207] However, when a GO membrane is employed as the solid electrolyte in some practical electrochemical devices,[8, 9, 56, 59, 123, 125, 195, 204, 208-211] its anisotropic proton-conducting properties is not favorable because the through-plane proton conductivity is more essential and meaningful than the in-plane counterpart. Some approaches have been proposed to enhance the proton conductivity of GO membranes *via* either doping small

molecules[40, 205, 206, 212] or the functionalization with proton-conductive moieties.[59, 125, 209, 213] However, although these strategies have increased the overall ionic conductivity, they have not changed the degree of anisotropy. Therefore, if the degree of anisotropy of proton conductivity could be decreased or even if the GO membrane could be transformed to a near-isotropic or isotropic proton conductor, the through-plane proton conductivity would be further enhanced for practical applications.

Herein, considering the high aspect ratio of 2D GO nanosheets in a laminated and anisotropic-shaped GO membrane, we purpose a strategy to tailor the proton-conducting pathway across the GO membrane *via* creating a porous morphology in GO nanosheets. In this design, a renewed pore-formation methodology using sonication-assisted (SA) Fenton reaction is introduced. Briefly, Fenton reaction[214] involves the reduction of hydrogen peroxide in the presence of a ferrous catalyst to generate ·OH radicals, which are powerful and non-selective oxidants.

Table 5-1. Table comparing pore-forming methodologies for GO

Methodology	Precursors	Temperature	Scalable	Additional Notes	Ref
Steam-Etching	GO, Water	200 ºC (hydrothermal)	Very Difficult	Partially reduces GO	33
UV irradiation	GO, O_2	Room Temp.	Difficult	Partially reduces GO	34
Ozonation	GO, O_3	Room Temp.	Easily		9
Annealing	rGO, Air	400 ºC	Difficult		215
Microwave Plasma	rGO, O_2	Room Temp.	Very Difficult		215
UV irradiation	rGO	Room Temp.	Easily		215
SA-Fenton reaction	GO, H_2O_2 & Ferrous salt	Room Temp.	Very Easily		This work

Compared to the so far reported methods, which is summarized in **Table 5-1**, SA-Fenton reaction is favorable towards the pore-forming process in terms of the following distinct advantages. First, the hydroxyl radicals, initialized *via* Fenton reaction, function as the strong

oxidizers to further oxidize GO and maintain the oxidizing environment in the suspension. Second, harsh treatments such as heat treatment, UV radiation and plasma etching are avoided in this facile method,[34, 144, 216-219] decreasing the risk of reducing the GO nanosheets. Third, the enhanced mixing and diffusion as well as additional hydroxyl radicals generated *via* sonication improve the reaction efficiency, which shortens the reaction duration and enables the possibility of scaled-up production. The obtained free-standing porous GO (pGO) membranes demonstrate a significant enhancement in the through-plane proton conductivity, and resulting isotropy, as opposed to pristine GO membranes because of the balance between the in-plane and the through-plane proton conduction. The value of $\sigma_{\parallel}/\sigma_{\perp}$ for the pGO membrane can reach up to 2.77 at 25°C and 100% relative humidity (RH), confirming it as a near-isotropic, proton-conducting GO membrane. Despite both GO and pGO membranes exhibiting low ethanol detection limits, and excellent ethanol linearity, the significant enhancement in response and sensitivity when integrated into an alcohol fuel cell sensor further testifies of its superior proton conduction across the pGO membrane. Therefore, generating pores on GO nanosheets *via* the SA-Fenton reaction has proven to be an effective strategy to transform a GO membrane to a near-isotropic proton conductor and a promising protic solid electrolyte for electrochemical devices.

5.2 Experimental Section

Graphite flakes (2-15 μm) were purchased from Alfa Aesar. Other chemicals, including sulfuric acid (H_2SO_4, 98%), potassium permanganate ($KMnO_4$, 99%), sodium nitrate ($NaNO_3$, 99%), hydrogen peroxide (H_2O_2, 30%), hydrochloric acid (HCl, 37%), iron(II) sulfate heptahydrate ($FeSO_4 \cdot 7H_2O$, 99%) were purchased from Sigma-Aldrich.

5.2.1 Synthesis of Graphene Oxide

GO was prepared according to modified Hummer's Method.[17, 220] Briefly, graphite powder (2 g,) and $NaNO_3$ (1 g) were mixed with concentrated sulfuric acid (46 ml) in an ice bath. $KMnO_4$ (6 g) was added slowly into the mixture under mechanical stirring. The temperature was maintained below 20 °C. The ice bath was removed, while the exfoliation and oxidation continued under stirring for an additional 2 hours. Then, distilled deionized (DDI) water (140 ml) was slowly added, resulting in a violent effervescence. The mixture was allowed to stir for another 30 minutes to increase the degree of oxidation in the product. The mixture was further

diluted with DDI water (120 ml) and treated with H_2O_2 (40 ml), turning the solution color to bright yellow. The resultant solution was filtered and washed with diluted HCl (2L, 5 %) to remove metal ions. Then, the acid was removed *via* cycling between re-dispersion with copious amounts of DDI water and the centrifugation at 4000 rpm, until the pH of the dispersion was around 3.0. Lastly, the GO was stored as a diluted solution (~10 mg mL^{-1}) for further use.

5.2.2 Synthesis of Porous Graphene Oxide (pGO)

The preparation of pGO was fulfilled *via* sonication-assisted Fenton reaction (SA-Fenton). Typically, $FeSO_4 \cdot 7H_2O$ (0.5 mg) was dissolved into DDI water (5 mL), then the solution was dropwise added into the GO solution (40 mg, 100 mL) under vigorous mixing. After stirring for 30 min, dilute H_2O_2 solution (1.6%, 20 mL) was added into the mixture dropwise and it was allowed to continue stirring for another hour. Then, the solution was subjected to a high frequency (44 kHz) sonication radiation for a prescribed period of time, for instance 12 hours. The resultant suspension was charged in a dialysis bag to remove the iron ions through dialysis. Finally, the pGO suspension was lyophilized and re-dispersed into DDI water at a concentration of 0.5 mg mL^{-1}.

5.2.3 Membrane Fabrication

The free-standing GO and pGO membranes were prepared *via* the typical vacuum filtration casting. Prior to membrane casting, a thin layer of GO nanosheets was pre-deposited, to prevent ethanol permeation,[41, 47, 187] on the poly (ether sulfones) (PES) membrane (47 mm, 200 nm) *via* the filtration of a dilute GO suspension (1 mg mL^{-1}, 5 mL). Then, the aforementioned pGO suspension (0.5 mg mL^{-1}, 80 mL) was filter-cast through the GO-coated PES membrane, and the obtained free-standing flexible pGO membrane was about 25 μm thick. For the sake of comparison, GO membrane was also fabricated *via* the filtration of a dilute GO suspension (0.5 mg mL^{-1}, 80 mL) through the pre-coated PES membrane.

5.2.4 Physicochemical and Electrochemical Characterizations

The chemical structure of GO and pGO nanosheets was characterized *via* X-ray photoelectron spectroscopy (XPS, Thermo Scientific Al K-α X-ray source) and the elemental

composition was analyzed semi-quantitatively by XPS and energy-dispersive X-ray spectroscopy (EDX, LEO FESEM1530). The structural morphology of nanosheets and membranes were imaged by Transmission Electron Microscopy (TEM, JEOL 2010F) and Scanning Electron Microscopy (SEM, LEO FESEM1530). X-ray diffraction (XRD) patterns were collected by a Rigaku Miniflex 600 X-ray diffractometer while the Raman spectra were obtained from a DXR Raman microscope (Bruker Senterra, 532 nm laser).

The conductivity measurements were proceeded *via* AC electrochemical impedance spectroscopy (EIS, Princeton Versastat MC Potentiostat) at a frequency range of 100 kHz to 1 Hz and perturbation signal amplitude of 100 mV in varied environmental conditions. Initially, the thickness of each membrane was measured with a micro-caliper. Then, for through-plane (TP) measurements, the membrane was sandwiched between two overlapped platinum current collectors. However, for in-plane (IP) measurements, the membrane was sandwiched between a Teflon block equipped with four platinum wires for connection. After confirming the dimensions of the membrane, the sandwiched membrane was placed within an in-house, humidity chamber, where the environmental conditions were regulated. The IP and TP resistances were measured first at room temperature and varying the humidity (25 %, 40 %, 55 %, 70 %, 85 %, 100 % RH), then holding the humidity at 100% and varying the temperature (25 ^{o}C, 30 ^{o}C, 35 ^{o}C, 40 ^{o}C, 45 ^{o}C). Lastly, the conductivity was calculated *via* **Equation (3-11)**. The activation energy is calculated to determine the proton transportation mechanism within the membrane. The proton conductivity follows the Arrhenius relationship (**Equation (3-12)**). Thus, for each membrane, the activation energy for proton transport can be calculated from the slope of $ln\ \sigma_0$ *vs. 1000/T* plot.

To calculate the proton mobility, water uptake (WU) and ion exchange capacity (IEC) were measured first. WU (g g^{-1}) was measured by cutting the membrane into a 1 cm x 1 cm square and weighing it as it absorbs water at 100% RH in a gravimetric sorption analyzer (DVS Resolution, Surface Measurement Systems, London, U.K.). Initially, the sample was subjected to dry N_2 air at 25 ^{o}C for 6 hours (to obtain the dry sample mass), then held at 100% RH until the dm dt^{-1} of the membrane reached 0.0008 % min^{-1}. The water uptake was calculated by comparing the mass of the sample at the end of the water absorption session with respect to its dry sample mass. IEC was evaluated *via* the classical titration method. Briefly, 15 mg dry GO or pGO samples were weighed and dispersed in NaCl solution (10 mL, 1 mol L^{-1}) for 4 h to fully exchange the protons in the membrane with Na^+ ions. Then, standard sodium hydroxide (NaOH) solution (0.01 mol L^{-1}) was used to titrate the mixture until it turned pink, as indicated by

phenolphthalein. According to the volume of used NaOH solution, the IEC value (mmol g^{-1}) is determined based on the following equation,[59]

$$IEC = c_{NaOH} V_{NaOH} / m_{sample} \quad \textbf{(5-1)}$$

where c_{NaOH} is the concentration of the standard NaOH solution (*i.e.* 0.01 mol L^{-1}), V_{NaOH} is the volume of used standard NaOH solution, and m_{sample} is the mass of the dry sample. Thus, the proton mobility (μ_{H^+}, $cm^2\ V^{-1}\ s^{-1}$) of GO and pGO membranes in either direction can be calculated according to:[111]

$$\mu_{H^+} = \frac{\sigma_{H^+} \times WU}{F \times IEC \times d} \quad \textbf{(5-2)}$$

where σ_{H^+} is the measured proton conductivity (S cm^{-1}) in either direction, *F* is the Faraday constant (96485 C mol^{-1}), *d* is the density of aqueous solution, taken as 1 g cm^{-3}.

5.2.5 Dynamic Vapor Sorption Measurements

Water absorption isotherms were obtained *via* the dynamic vapor sorption (DVS) experiment, which was equipped with a microbalance and a mass resolution of 0.1 μg. Typically, the membrane is cut into 1 cm x 1 cm squares and placed onto the DVS pans. Initially, the sample was dried in an N_2 environment at 25 °C for 8 hours, then subjected to a relative humidity (RH) profile of: 0 to 10% RH at interval of 1%, and 10% to 97.5% RH at interval of 2.5%. The mass was measured at each equilibrium, or the end of each interval as denoted by whichever was shorter between 3 hours or a dm dt^{-1} of 0.004%.

According to literature,[221-223] the water absorption isotherm of proton exchange membrane can be fitted to Park's multimode absorption model:

$$WU = W_{SA} + W_{NSA} + W_C \quad \textbf{(5-3)}$$

which corresponds to the 3 different mechanisms of absorption: W_{SA} corresponds to the specific adsorption, W_{NSA} to non-specific adsorption and W_C corresponding to clustering. Furthermore, each mechanism of absorption can be expanded to:

$$W_{SA} = \frac{Q_0 K_L a_w}{1 + K_L a_w} \quad \textbf{(5-4)}$$

$$W_{NSA} = K_H a_w \quad \textbf{(5-5)}$$

$$W_C = nK_A a_w^n \quad \textbf{(5-6)}$$

where Q_0 is the specific site capacity (mmol g^{-1}), K_L, is the affinity constant, K_H is Henry's Law coefficient (mmol g^{-1}), K_A is the aggregation equilibrium constant (mmol g^{-1}) regarding $nH_2O \rightleftharpoons (H_2O)_n$, n is the aggregate size, and a_w is the water activity/relative humidity. Finally, substituting **Equations (5-4)**, **(5-5)**, and **(5-6)**, into **(5-3)** yields the expanded expression:

$$WU = \frac{Q_0 K_L a_w}{1 + K_L a_w} + K_H a_w + nK_A a_w^n \quad \textbf{(5-7)}$$

which was used to fit the moisture absorption isotherm.

5.2.6 Electrochemical Gas Sensor Evaluation

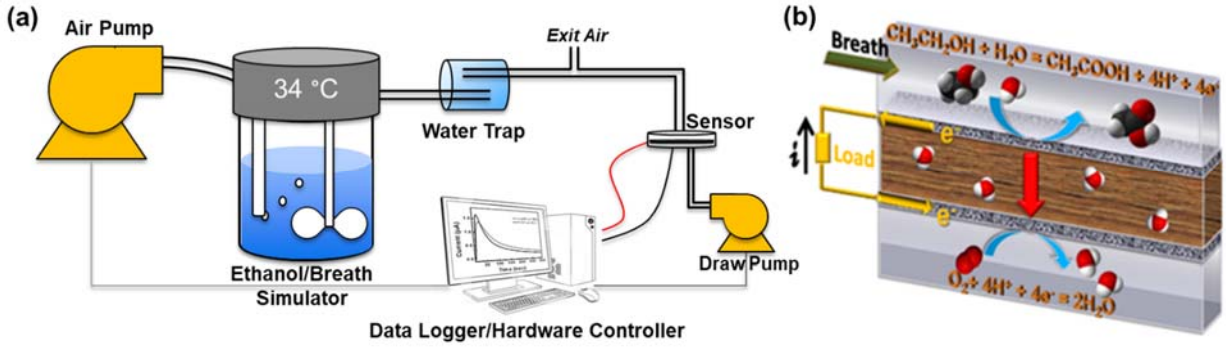

Figure 5-1. Diagram of (a) the electrochemical gas sensor setup and evaluation, and (b) the electrochemical principle in AFCS

A pGO or GO membrane was first sandwiched with two commercial gas diffusion electrodes (GDE, 0.5 mg_{Pt} cm^{-2}, 60% Pt/C, Fuel Cell *etc.* Ltd., Texas, USA) and hot-pressed into a membrane electrode assembly (MEA). The hot-pressing was conducted at 130°C and 20 MPa for 3 min with plastic sheets as the supporting layers. A round MEA with a diameter of 16 mm was integrated into a plastic housing and sealed prior to the evaluation of electrochemical alcohol sensor. Prior to the test, the housing sat in the humidity chamber at 60% RH and 25 °C for 72 h and equilibrated with the environment. Then, the housing was inserted into the testing device **(Figure 5-1a)**. When the test started, warm ethanol vapor was carried by the air at a fixed flow rate out from the breath simulator (Guth, PA, USA) and a fixed volume of this gas sample was injected to the housing electrochemical gas sensor *via* an induction pump. The

response current-time curve was recorded by a digital multimeter (Agilent 34411A). Five repeated rests were required for each sensor at each ethanol vapor concentration within a 30 min testing period. The integrated peak area under the response curve was calculated as the main signal that is linear with the concentration of ethanol vapor. [209, 210] The linear standard curves of peak area and ethanol vapor concentration for GO and pGO membranes were plotted after the collection of response curves to all testing ethanol vapor. The sensitivity was defined as the fitted slope of linearity curves.

Alternatively in **Figure 5-1b**, when the ethanol vapor enters the alcohol fuel cell sensor (AFCS) housing chamber, the ethanol molecules diffuse through the gas diffusion electrode (GDE) to interact with the catalyst on surface. Moreover, the ethanol will adsorb onto the Pt/C catalyst triggering ethanol oxidation reaction (EOR) at the anode, simultaneously releasing electrons and protons, and the by-product, acetic acid. The protons (oxonium ions) from the EOR migrate through the membrane to the cathode, while the electrons migrate through the external circuit to cathode. At the cathode, protons interact with electrons and oxygen, from the air, initiating oxygen reduction reaction (ORR) and generating water as the only product. The electrons that flowed through the external circuit are recorded and correlated to the ethanol concentration in vapor *via* the coulometric methodology.

5.3 Results and Discussion

5.3.1 Physicochemical Characterization & Functionalization

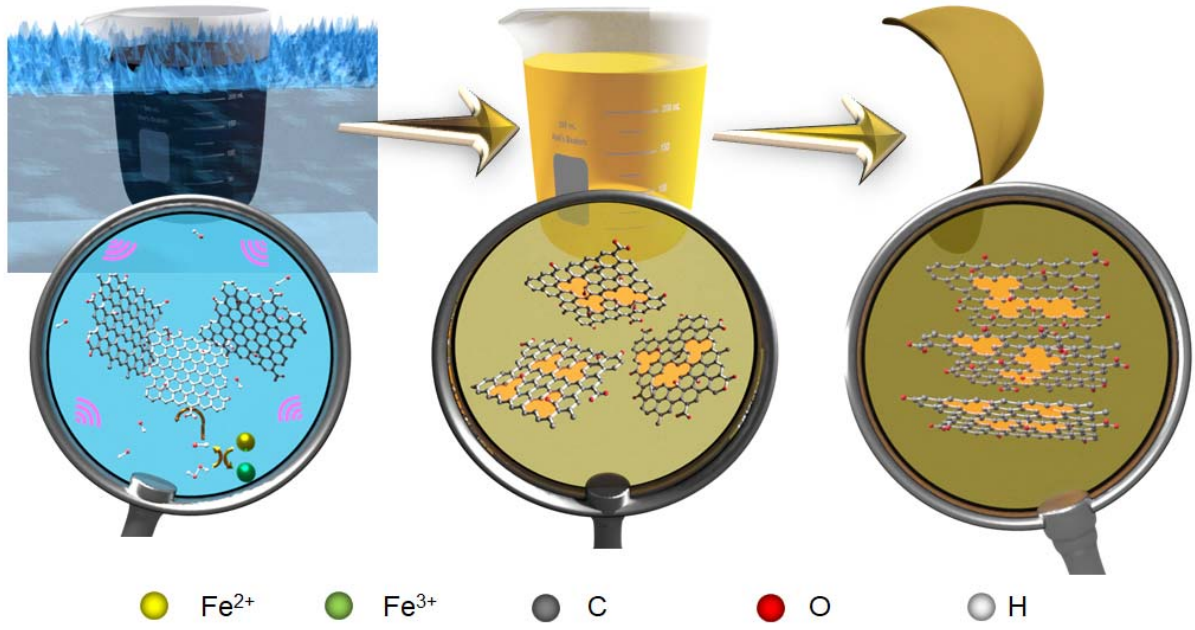

Figure 5-2. The preparation of free-standing pGO membrane by SA-Fenton reaction and filtration casting.

As illustrated in **Figure 5-2**, to prepare the near-isotropic proton conducting pGO membranes, the SA-Fenton reaction is introduced to the procedure. The highly-oxidative hydroxyl radicals were initiated *via* trace amounts of the Fe^{2+}/Fe^{3+} redox-couple,[224, 225] which prompts the formation of pores on the GO nanosheets *via* further oxidization. The significant color change (from dark, opaque brown to light, transparent yellow) of the GO suspension after being treated by SA-Fenton reaction successfully confirms the structural changes and further oxidation of GO.[9]

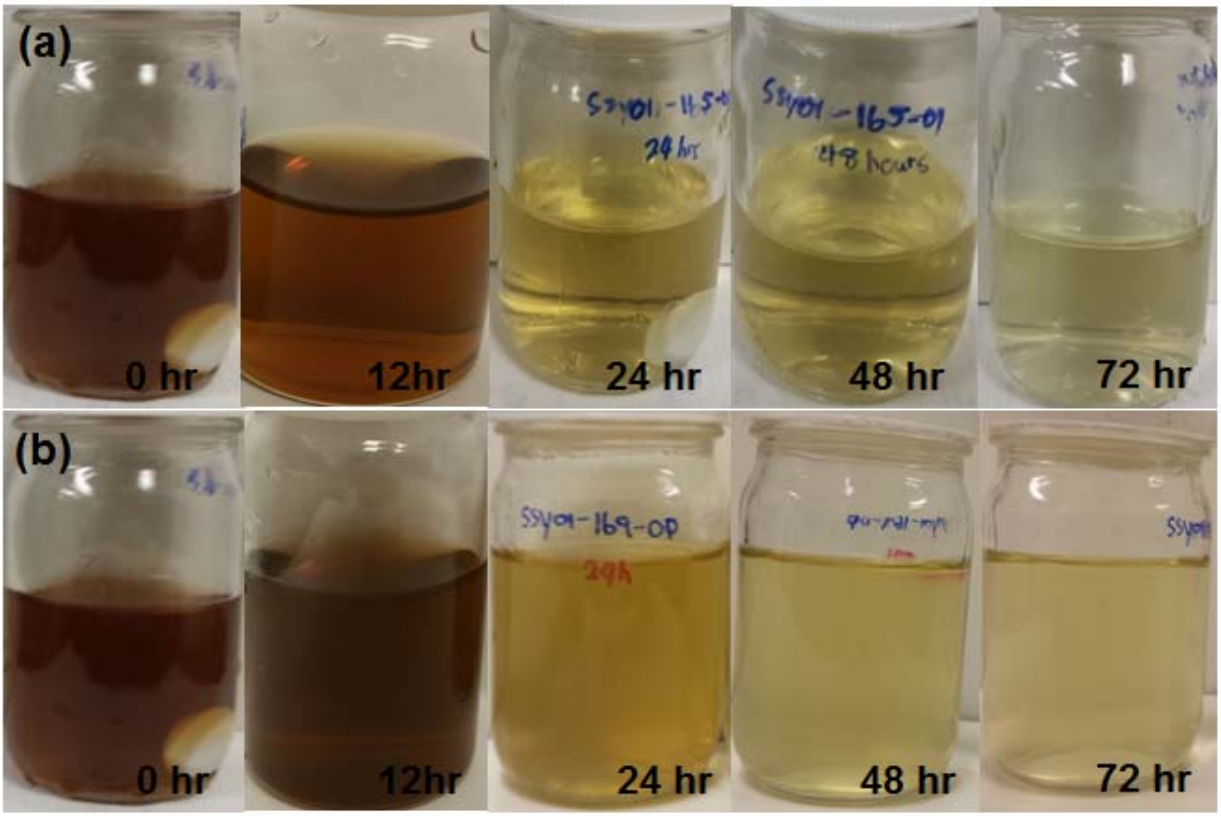

Figure 5-3. Digital pictures of GO suspension under the treatment of (a) SA-Fenton reaction and (b) normal Fenton reaction for different durations.

Apart from the traditional Fenton reaction, the extra radiation energy from high-frequency, ultrasonic waves in the aqueous solution can dramatically accelerate the reaction. This effect was directly observed by the faster color fade in the presence of a sonication field (**Figure 5-3**) in comparison with the treatment *via* normal Fenton reaction.

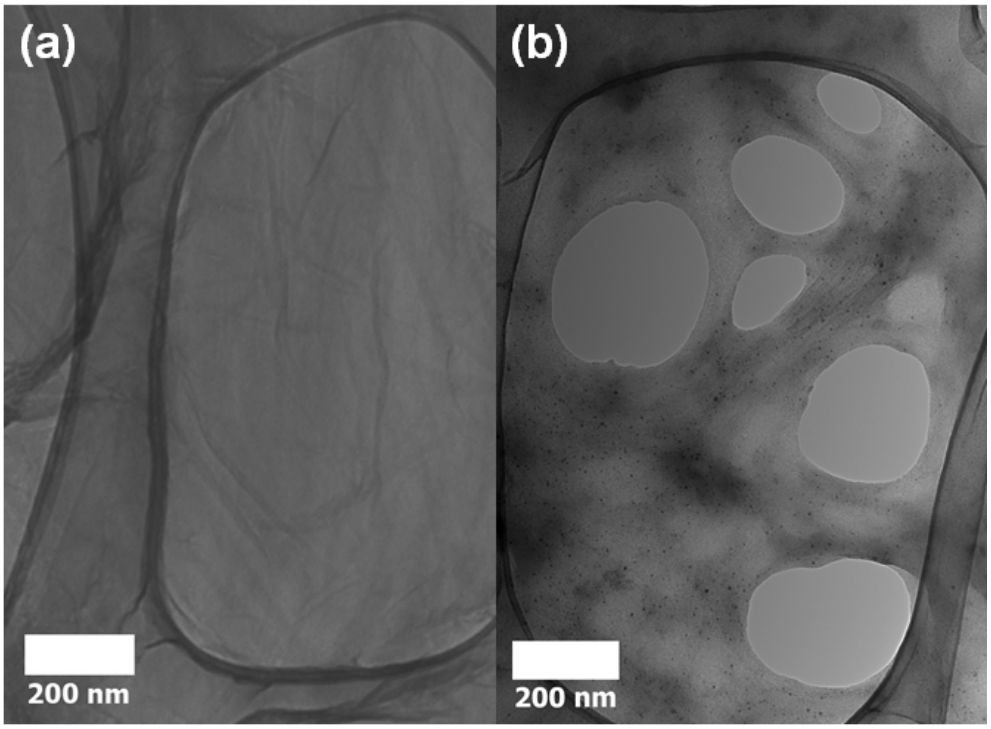

Figure 5-4. TEM images of GO nanosheets after (a) normal and (b) sonication-assisted Fenton reaction for 16h.

From a microscopic perspective, the transmission electron microscopic (TEM) images (**Figure 5-4**) disclose an enhanced capability of pore generation on GO nanosheets when the Fenton reaction was coupled with sonication. This could be attributed to not only the great enhancement of the mass transport for all reactants within the sonication field, but also the additional hydroxyl radicals generated *via* the sono-chemical effects.[224, 225]

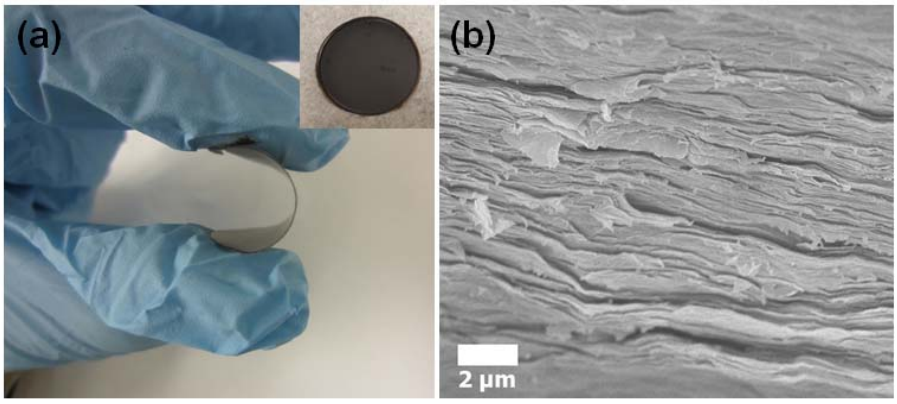

Figure 5-5. (a) The digital picture of GO membrane (insert: image of flat membrane) and (b) cross-section SEM image of GO membrane.

Lastly, the pGO suspension was filtered and cast onto a free-standing flexible membrane **(Figure 5-2 & Figure 5-5a)**, with the typical morphology of well-stacked nanosheets as shown in the cross-sectional scanning electron microscopic (SEM) image in **Figure 5-5b**).

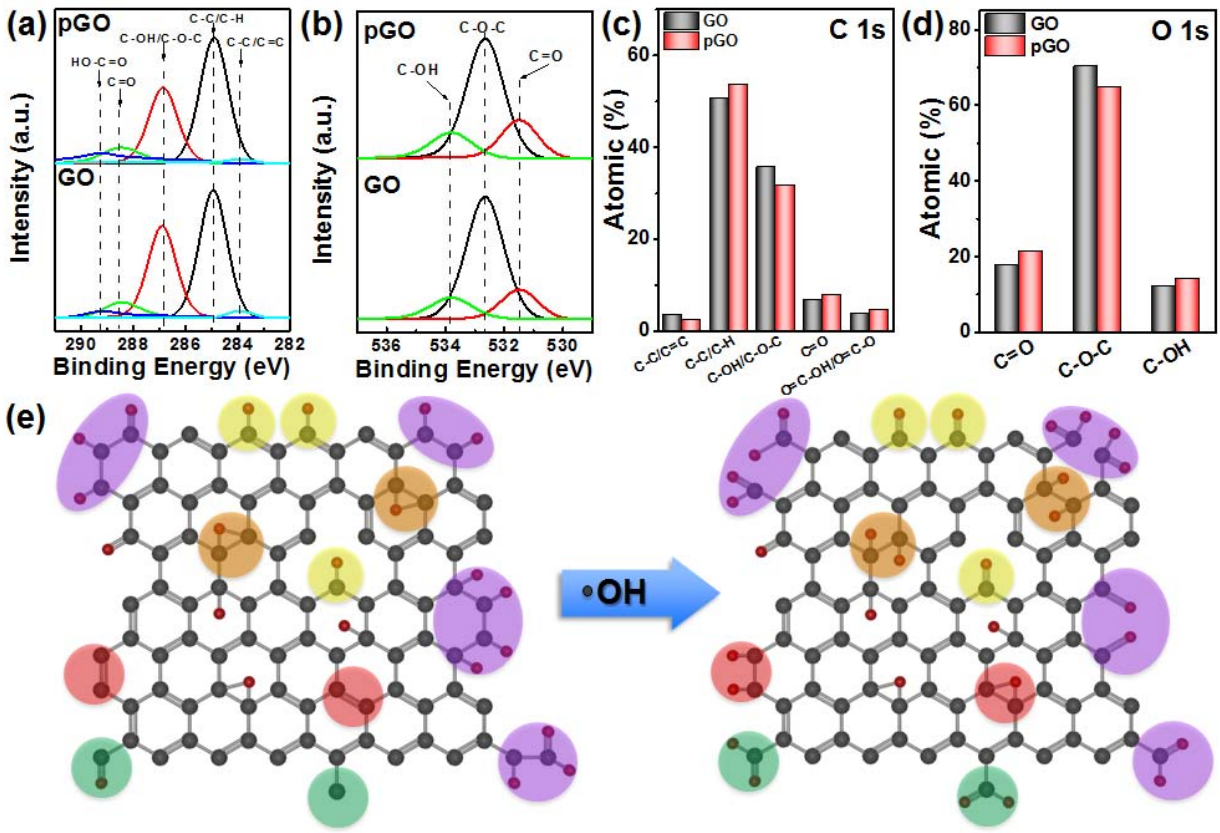

Figure 5-6. High resolution (a) C 1s and (b) O 1s XPS spectra of GO and pGO with the summary of atomic percentages of different chemical structures obtained from (c) C 1s and (d) O 1s spectra, (e) The proposed reaction mechanism of oxidation reaction of GO nanosheets by hydroxyl radicals during SA-Fenton reaction.

Table 5-2. Elemental composition of GO and pGO *via* EDX and XPS

Element	EDX		XPS	
	GO	pGO	GO	pGO
C	75.7%	74.3%	70.4%	70.0%
O	24.3%	25.7%	29.6%	30.0%

To elucidate the oxidization mechanism of GO nanosheets *via* SA-Fenton reaction, GO and pGO nanosheet films were investigated by X-ray photoelectron spectroscopy (XPS) shown in **Figure 5-6a, b**. According to the elemental composition obtained by both XPS survey and

energy-dispersive X-ray spectroscopy (EDX) in **Table 5-2**, the oxygen content increases slightly after subjecting GO to SA-Fenton reaction. In the high-resolution spectra of C 1s (**Figure 5-6a**), both pristine GO and pGO exhibit five typical peaks, namely sp^2-hybridized C=C (283.9 eV), sp^3–hybridized C-C/C-H (284.9 eV), epoxide (286.9 eV), carbonyl (288.4 eV), and carboxyl groups (289.2 eV), which are in agreement with literatures.[56, 59, 123, 226] Likewise, the three peaks at 531.5, 532.7 and 533.8 eV corresponding to C=O, C-O-C and C-OH, respectively, are found in the O 1s spectra of both pristine GO and pGO (**Figure 5-6b**).[56, 59, 211] Although the chemical bonds in pGO are similar to that of GO, the relative amounts of the different species within pGO differ from those in pristine GO, which could reveal the oxidization mechanism of GO when subjected to SA-Fenton reaction.

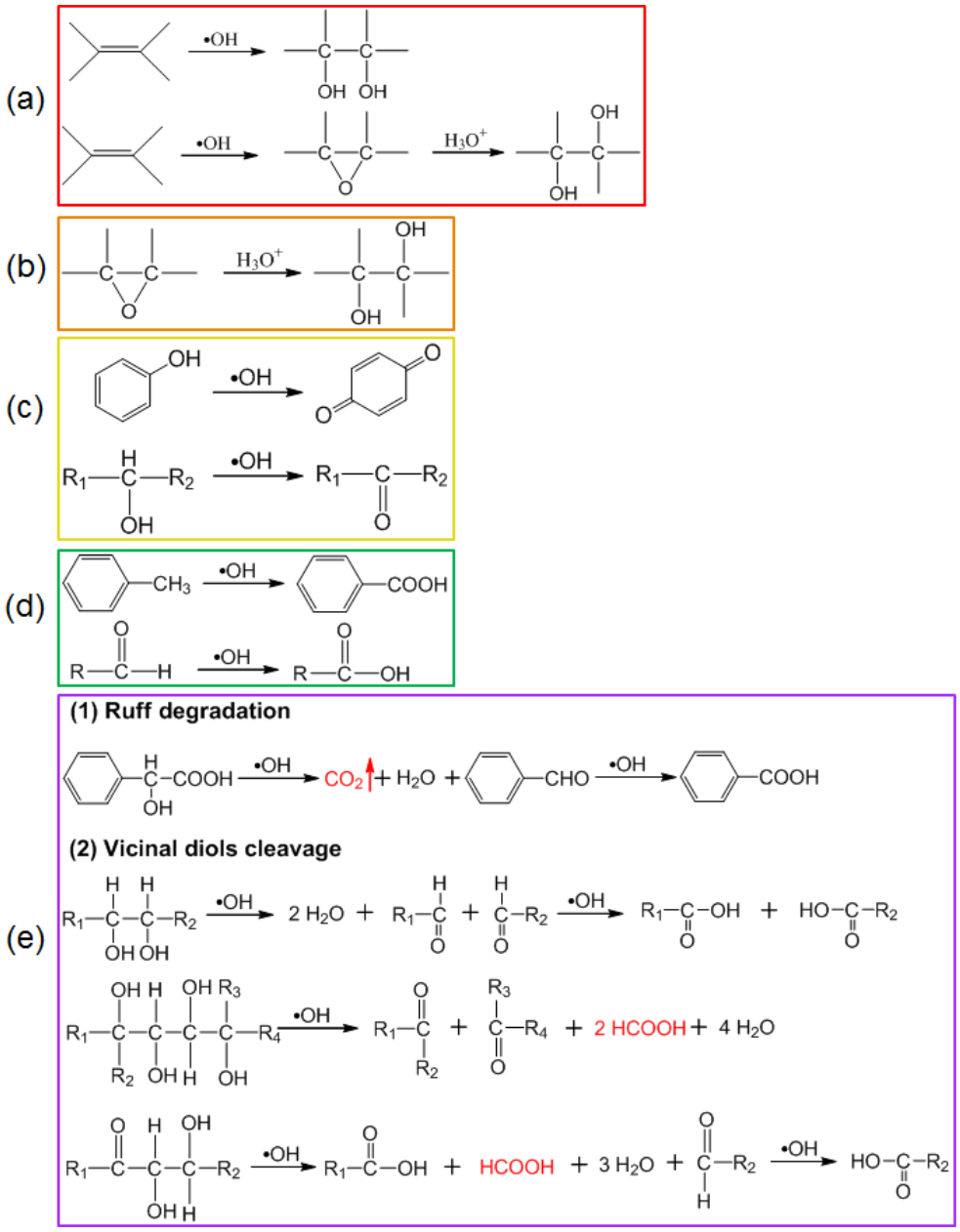

Figure 5-7. Proposed mechanism of oxidizing GO *via* SA-Fenton reaction. (a) C=C double bonds react with hydroxyl radicals by oxidative addition or hydroxylation reactions with epoxide as intermediates, resulting in C-C single bonds; (b) Epoxides react with water to form hydroxyl *via* ring opening reaction in acidic condition; (c) Phenols and alcohols are oxidized into quinones and ketones/aldehydes respectively; (d) The oxidation of either the side-chain adjacent to the aromatic moieties or the aldehyde groups at the edges of nanosheets into carboxylic groups; (e) The carbon atoms removal from the nanosheets by the oxidation of the side-chain carboxylic groups to release CO2 (*e.g.* Ruff degradation) and vicinal diols cleavage reaction to generate small molecules.

As summarized in **Figure 5-6c**, sp^2-hybridized C=C in pGO decreases in 33% while sp^3–hybridized C-C/C-H in pGO increases in 6% after the treatment. This suggests that the C=C double bonds undergo the possible oxidative addition or hydroxylation reactions with •OH radicals, resulting in the formation of C-C bonds as illustrated in red circles of **Figure 5-6e** and the chemical formula in **Figure 5-7a**.[227] The epoxide/alcohol groups of pGO in **Figure 5-6c** have apparently decreased by 11% as opposed to that of GO. However, by comprehensive examination of oxygen species by O 1s spectra, **Figure 5-6d** discloses that a 16% increase in alcohol/hydroxyl groups partially offsets the 11% decrease in epoxide/alcohol groups in **Figure 5-6c**. This increase could be explained by the hydroxylation through the ring-opening reaction of the epoxide groups, which are highlighted in orange in **Figure 5-6e** and illustrated in **Figure 5-7b**. According to **Figure 5-6c, d**, carbonyl groups increased 21% after the SA-Fenton treatment, which could be attributed to the oxidation of phenols and alcohols into quinones and ketones/aldehydes, respectively, by •OH radicals.[227] This is depicted in **Figure 5-7c** and denoted by yellow circles in **Figure 5-6e**. Besides, according to **Figure 5-6c**, the carboxylic groups and/or ester groups increased by 26%. This could be resulted from two possible mechanisms: the oxidation of either (i) the side-chain adjacent to the aromatic moieties or (ii) the aldehyde groups at the edges of nanosheets (highlighted in green in **Figure 5-6e** and the chemical formula in **Figure 5-7d**).[227, 228] Lastly, because of the highly oxidative nature of hydroxyl radical (E^o = 2.80 V), the dangling carboxylic groups on the edge could also be further oxidized, and release CO_2 and water *via* Ruff degradation as shown in **Figure 5-7e-1**.[51, 52] Considering the vicinal diols formed on the unsaturated C=C in **Figure 5-7a**, a possible cleavage reaction could occur during the SA-Fenton reaction, which results in the breaking of a C-C bond and the formation of ketone or carboxylic acid (**Figure 5-7e-2**). Moreover, when extra hydroxyl or α-hydroxy ketone groups is adjacent to the vicinal diols, a possible cleavage reaction can release smaller soluble molecules (*e.g.* formic acid) into the solution. These reactions lead to the loss of carbon atoms and the etched edges of GO nanosheets (purple highlights in **Figure 5-6e**). To sum up, with the further oxidation by •OH radicals, the reduced and lightly-oxidized species, such as C=C, epoxides, alcohol/phenol groups, were converted into highly-oxidized species, such as ketones, quinones, carboxylic groups and even CO_2. Arising from high-frequency sonication, the generation of extra •OH radicals as well as the improved mass transport of all reactants greatly enhanced and accelerated the oxidation and etching of GO nanosheets.

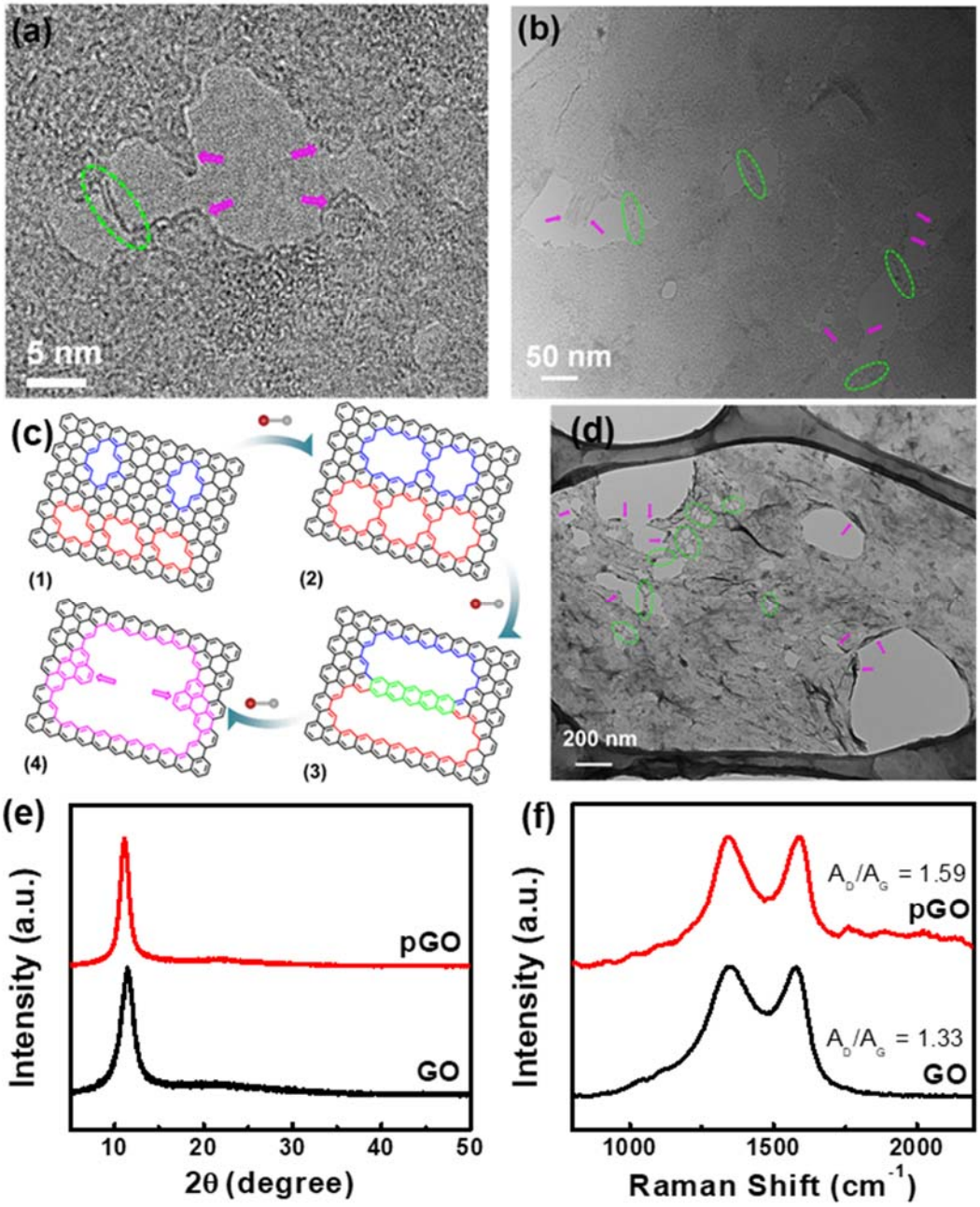

Figure 5-8. (a) HR-TEM and (b) TEM images of pGO nanosheets after 12h SA-Fenton reaction. (c) The proposed scheme of pore formation on GO nanosheets *via* hydroxyl radical etching; (d) TEM image of pGO nanosheets after 16h SA-Fenton reaction; (e) XRD patterns and (f) Raman spectra of free-standing GO and pGO membranes.

To visualize and detect the mechanism of the etching process and pore formation on GO nanosheets by •OH radicals, the HR-TEM image of a 12h-SA-Fenton-treated pGO nanosheet (**Figure 5-8a, b**) were investigated.

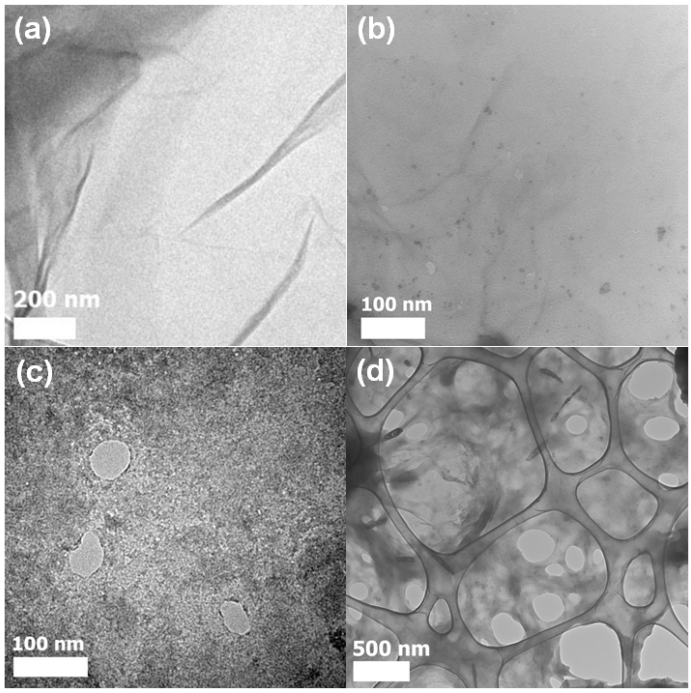

Figure 5-9. TEM images of GO nanosheets under the treatment of SA-Fenton reaction for (a) 0h, (b) 8h, (c) 12 h and (d) 16 h.

Additionally, TEM images that highlight the pore-formation process on GO nanosheets at different reaction times (**Figure 5-9**) were also considered. It can be observed that different nanostructures at different states of oxidation were simultaneously formed. As illustrated in the scheme of **Figure 5-8c**, the inner edges of the original pinholes (outlined in blue and red, **Figure 5-8c-1**) on the GO nanosheet are etched by •OH radicals, causing the pinholes to grow larger **(Figure 5-8c-2)**.[227] As the •OH radicals continue to etch the inner edges of pinholes and of the small pores, at stage (3) of **Figure 5-8c**, a thin “bridge” (outlined in green) will gradually form between adjacent pores (the green circles in the HR-TEM image). Eventually, this “bridge” collapses under the continuous attack of •OH radicals, resulting in the joining of two small adjacent pores into one large pore (outlined in magenta, **Figure 5-8c-4**). As “bridges” continue to be oxidized into water-soluble species, the small pores eventually merge into larger pores,

leaving the peninsula-like structures on the edge (magenta arrows in **Figure 5-8a-d**). It can be concluded that the mechanism of pore growth on the GO nanosheets can be likened to step-growth polymerization. The pinholes/defects, small pores and large pores are metaphorically monomers, oligomers and polymers, respectively, while the growth of pores is akin to the propagation of polymer chains. In step-growth polymerization, high molecular weight polymer chains eventually appear towards the end of the reaction. Likewise, as displayed in **Figure 5-8d & Figure 5-9d**, large amounts of macropores (> 50 nm) suddenly appear after the treatment of SA-Fenton reaction for 16 hours. Thus, it is reasonable to rationalize that those macropores originate from hundreds of micropores and mesopores. Besides, the SA-Fenton reaction should be terminated before 16 hours to avoid the undesired degradation of GO nanosheets.

Table 5-3. Summary of data derived from XRD patterns and Raman spectra

Sample	XRD			Raman	
	d-spacing, Å	L_c	# of Layers	I_D/I_G	A_D/A_G
GO	7.17	64.49	9.00	1.00	1.59
pGO	7.33	51.92	7.09	1.01	1.33

Both GO and pGO suspensions were cast into thin membranes *via* filtration through a GO-coated polyethersulfone membrane. The obtained GO and pGO membranes are brownish and flexible with the typical laminated sheets structures (**Figure 5-2 and Figure 5-5**). Although their macroscopic appearance is alike, their crystal structures are not identical. According to the XRD patterns of GO and pGO (**Figure 5-8e**), the major peaks at 11.7° and 11.1° were observed, corresponding to a d-spacing of 7.17 Å and 7.33 Å, respectively. In spite of the insignificant increase of d-spacing for pGO nanosheets, the stacking number of pGO layers is significantly less than that of pristine GO (7.09 *vs.* 9.00) according to the calculated results based on the Scherrer equation in **Table 5-3**. This implies that the further oxidation by hydroxyl radicals considerably enhances the exfoliation of GO layers. This could be attributed to the weakening of π-π stacking interaction between pGO nanosheets brought by the decrease of sp^2-hybridized carbon and the increase of pores on the nanosheets. Likewise, the intralayer structure of GO nanosheets also changed after SA-Fenton reaction, observed in the Raman spectra (**Figure**

5-8f). The area ratio of the D-band peak (~1344 cm^{-1}) and the G-band peak (~1584 cm^{-1}) for pGO is larger than that for pristine GO (1.59 *vs.* 1.33), indicating increased defects within the basal plane of pGO.[229,54] This is in agreement with the previous XPS analysis that the sp^2-hybridized carbons in the graphene network are transformed into the sp^3-hybridized carbons and oxygen-containing functional groups.[101, 227]

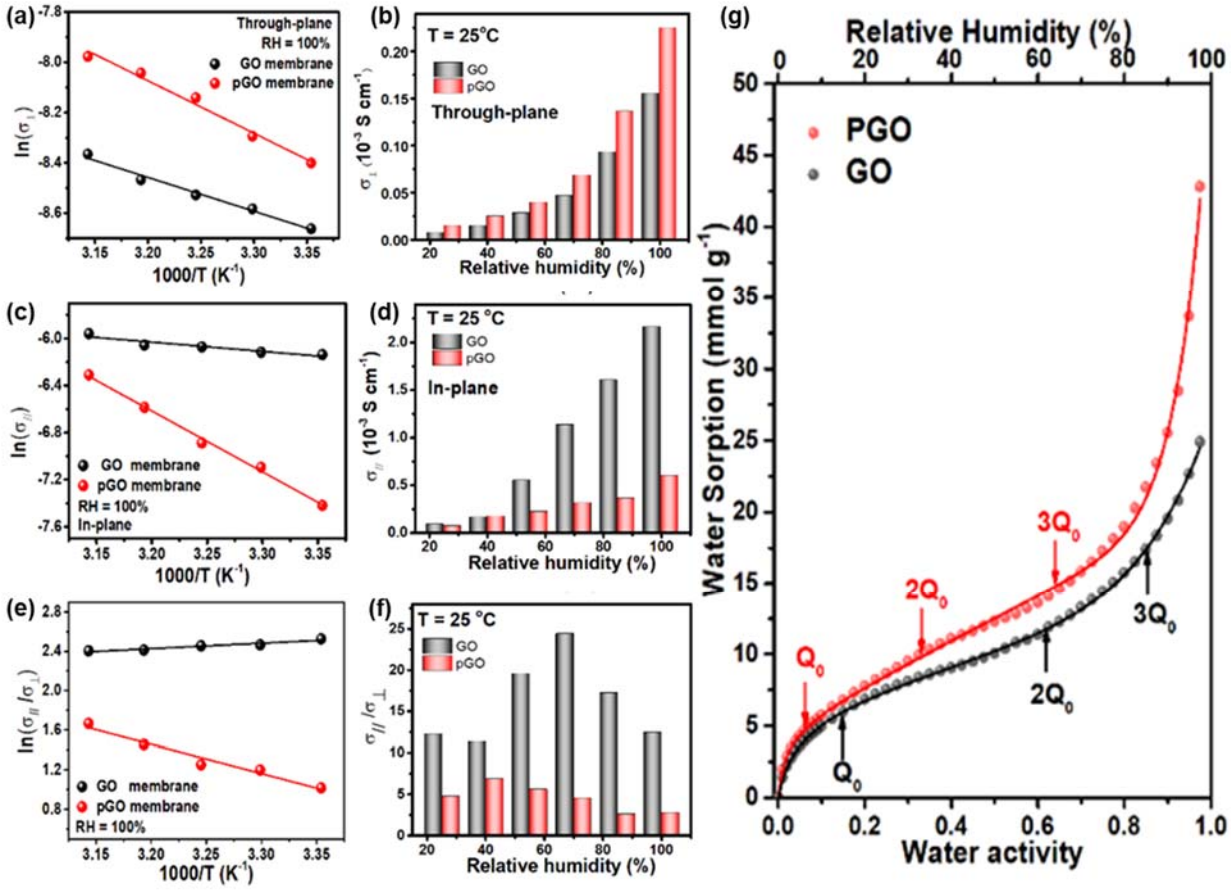

Figure 5-10. (a, b) Through-plane, (c, d) in-plane proton conductivity and associated (e, f) the degree of anisotropy as a function of temperature and relative humidity for GO and pGO membranes, (g) water adsorption isotherms of both GO and pGO membranes at room temperature.

Table 5-4. Proton mobility of GO and pGO membranes at 100% RH and room temperature

Membranes	IEC (mmol g^{-1})	Water Uptake (%)	Proton mobility $\times 10^5$ ($cm^2 V^{-1} s^{-1}$)	
			In-plane	Through-plane
GO	1.20 ± 0.03	142.4%	2.33	0.19
pGO	0.97 ± 0.14	345.0%	2.21	0.77

The proton conductivities of both pristine GO membrane and pGO membrane were measured under various environmental conditions. As depicted in **Figure 5-10**, proton conductivities, at both the parallel and perpendicular directions to the membrane, improve with the increase of the relative humidity and the temperature for all the membranes. In terms of the desirable through-plane proton conductivity, the obtained pGO membranes outperform the pristine GO membranes at all relative humidity and temperatures (**Figure 5-10a, b**). More specifically, the through-plane proton conductivity ($\sigma_{\perp}$) of pGO membrane improves by 47% and 55% as opposed to that of GO membrane under the fully hydrated condition at room temperature and 45°C, achieving 0.22 mS cm^{-1} and 0.34 mS cm^{-1}, respectively. Also, the through-plane proton mobility of pGO membrane at the 100% RH and room temperature is found to be 2.3 times higher than that of the GO membrane as displayed in **Table 5-4**. Given that the mobility is inversely proportional to the tortuosity of proton transport pathway,[111] the shortened proton transport pathway that accompanied the extra pore formation, within the nanosheets of pGO membrane is considered as the main contributor to the significant increase in the through-plane proton mobility and conductivity. In other words, the morphological change on the GO nanosheets has proven to be an effective strategy to selectively increase the through-plane proton conductivity for GO-based proton-conducting membranes. Interestingly, apart from the steady increase in the $\sigma_{\perp}$ as the temperature increases, the $\sigma_{\perp}$ increases dramatically at higher relative humidity (RH > 80 %). On the other hand, the pristine GO membranes demonstrate better in-plane conductivity ($\sigma_{\parallel}$) in comparison with pGO membranes at medium and high RH as well as different temperatures (**Figure 5-10c, d**).

Table 5-5. Summary of activation energies of in-plane and through-plane proton conductivities as well as the degree of anisotropic proton conductivity

Membranes	Activation Energy (kJ mol^{-1})				
	$Ea_{//}$	$Ea_{\perp}$	$Ea_{//} - Ea_{\perp}$*	$(Ea_{//} - Ea_{\perp})$**	Relative variation***
GO	6.56	11.18	-4.61	-4.62	0.22%
pGO	42.93	17.72	25.21	24.49	2.86%

Values are obtained from difference in the individual activation energies (Figure 5-10a, c)

****Values are directly obtained from the Arrhenius plot for anisotropy data (Figure 5-10e).***

***** The relative variation is based on the absolute values of $Ea_{//} - Ea_{\perp}$ and $(Ea_{//} - Ea_{\perp})$.***

As suggested by the activation energies listed in **Table 5-5,** the Grotthuss-type mechanism dominates the proton conduction at in-plane direction of the GO membrane while both Grotthuss-type and vehicle-type mechanisms contribute to its through-plane proton conductivity. For the pGO membrane, the activation energy increases to 42.93 and 17.72 kJ mol^{-1} for the in-plane and through-plane directions, respectively. The Grothuss mechanism, also known as proton hopping, can be considered the dominant mechanism when the activation energy is <3 kcal mol^{-1} (*i.e.* 12.55 kJ mol^{-1}).[45, 211, 230] Generally, the protons translate along neighboring lone-pair of H_2O molecules forming oxonium (H_3O^+) complexes in the process. Alternatively, the vehicle mechanism involves the migration of hydrated positive ions (*e.g.* H^+, Li^+, Na^+) that are bonded to a "vehicle" (*e.g.* H_2O, NH_3) forming complex ions, $[H^+(H_2O)_n]$.[231, 232] Thus, these results indicate the vehicle-type proton conduction occurs in both directions of the pGO membrane. It was observed that the $\sigma_{\|}$of pGO membrane enhanced steadily with RH until 100%, while that of the GO membrane started to substantially increase at the medium RH and continued increasing at high RH (**Figure 5-10c**).

Table 5-6. A comparison of the through-plane conductivity and anisotropy at room temperature of various works

Membrane Type	Thickness (μm)	Relative Humidity	$\sigma_{\perp}$ (mS cm^{-1})	Anisotropy	Ref.
GO	29	95%	0.18	10.51	This work
porous GO	34	95%	0.23	2.67	This work
GO	22	95%	0.86	N/A	[9]
Ozonated GO	22	95%	1.30	N/A	[9]
GO	18	95%	0.23	155	[233]
GO	42	95%	0.40	N/A	[8]
GO	Single-layer	95%	0.20	N/A	[126]
GO	~55	30%	0.40	5.63	[234]
GO	~55	95%	0.90	98	[234]
GO	22	30%	0.011	254.55	[207]

The trade-off between the in-plane and through-plane proton conductivities leads to the decrease of the degree of anisotropy ($\sigma_{\parallel}/\sigma_{\perp}$) for the pGO membrane at all environmental conditions (**Figure 5-10e, f**). At 25 °C, the maximum value of $\sigma_{\parallel}/\sigma_{\perp}$ decreases from 24.43 for the GO membrane at the medium RH of 70% to a near-isotropic value of 2.77, which possesses the lowest anisotropy reported thus far (**Table 5-6**), for the pGO membrane at 100% RH (**Figure 5-10f**). It is observed that the degree of anisotropy varies along with the temperature instead of being constant (**Figure 5-10e**), suggesting that the temperature has a certain effect on the degree of anisotropy itself. More interestingly, in **Figure 5-10e,** the degree of anisotropy is increasing with the temperature for the GO membrane, whereas that has a descending trend for the pGO membrane. This surprising change of anisotropy-temperature relationship can be justified by the required activation energy for proton conduction. As obtained from Arrhenius plots in **Figure 5-10a, c** and summarized in **Table 5-5**, the activation energies of in-plane proton conductivity for both samples differ from their through-plane counterparts, supporting the

anisotropic effects of temperature on proton conduction in GO-based membranes. Moreover, the anisotropic change can also be attributed to the stacking microstructure, as previously seen in the SEM (**Figure 5-5b**). Furthermore, this effect could be directly visualized from the following deduced equation, suggesting that the degree of anisotropic proton-conduction in GO-based membranes also follows the similar Arrhenius law:

$$\boldsymbol{ln}(\boldsymbol{\sigma}_{\parallel}/\boldsymbol{\sigma}_{\perp}) = \boldsymbol{ln}(\boldsymbol{A}_{\parallel}/\boldsymbol{A}_{\perp}) - \frac{(\boldsymbol{Ea}_{\parallel} - \boldsymbol{Ea}_{\perp})}{\boldsymbol{R}} \cdot \frac{\mathbf{1}}{\boldsymbol{T}} \quad \textbf{(5-8)}$$

where $\boldsymbol{\sigma}_{\parallel}/\boldsymbol{\sigma}_{\perp}$ is the degree of anisotropic proton conduction in GO and pGO membranes; $\boldsymbol{A}_{\parallel}$ and $\boldsymbol{A}_{\perp}$ are pre-exponential factors for in-plane and through-plane proton conduction, respectively, and are considered to be constant within the measuring temperature range; $\boldsymbol{Ea}_{\parallel}$ and $\boldsymbol{Ea}_{\perp}$ are the activation energies for in-plane and through-plane proton conduction, respectively; ***R*** is the universal gas constant and ***T*** is the temperature. The effectiveness of the equation is manifested by the fact that the value of $(\boldsymbol{Ea}_{\parallel} - \boldsymbol{Ea}_{\perp})$ calculated by the above Arrhenius law (**Figure 5-10e**) is in agreement with the difference of $\boldsymbol{Ea}_{\parallel}$ and $\boldsymbol{Ea}_{\perp}$ obtained individually (**Table 5-5**). Thus, the degree of anisotropy becomes independent of the temperature only when the apparent activation energies are identical in both directions. As listed in **Table 5-5**, the activation energy of in-plane proton conductivity is lower than its through-plane counterpart for the GO membrane, explaining the slight decrease of the degree of anisotropy with the temperature in **Figure 5-10e**. In contrast, the large positive difference between $\boldsymbol{Ea}_{\parallel}$ and $\boldsymbol{Ea}_{\perp}$ (25.21 kJ mol^{-1}) for the pGO membrane resulted in a significant increase of the degree of anisotropy (**Figure 5-10e**). Therefore, according to the above relation, it is reasonable to assume that the pGO membrane could further become isotropically proton-conductive ($\boldsymbol{\sigma}_{\parallel}/\boldsymbol{\sigma}_{\perp}$ < 1.2) at temperatures as low as 2 °C.

On the other hand, the degree of anisotropy varies dramatically with another environmental parameter, *i.e.* relative humidity. As illustrated in **Figure 5-10f**, both the pristine GO and the pGO membranes show a volcano-shape relationship of the degree of anisotropy as function of RH. This relationship is an intriguing and curious phenomenon for GO-based proton conducting membranes. The degree of anisotropy for the GO membrane peaked at a medium RH (~70%) while that for pGO membrane peaked around 40% RH. To further understand the relationship of the degree of anisotropy with RH, water sorption isotherms of both GO and pGO membranes were obtained by dynamic vapor sorption (DVS) measurement and plotted in **Figure 5-10g**.

Table 5-7. Summary of parameters and corresponding coefficient of determination from fitting Park's model to the DVS isotherms for GO and pGO membranes

Membranes	Q_0 (mmol g^{-1})	K_L	K_H (mmol g^{-1})	K_A (mmol g^{-1})	n	R^2
GO	5.88	23.02	9.41	1.70	6.83	0.9994
pGO	4.91	54.36	15.59	2.17	14.65	0.9980

Similar to other proton-conducting membranes, these two isotherms can be perfectly fitted by Park's model (**Table 5-7**).[221-223, 235] Hence, the water sorption behavior can be described as the combination of three different mechanisms of water absorption, namely water adsorption on specific sites (Langmuir model) form a water monolayer at low RH, non-specific sorption *via* Henry's law to form multilayer water, and water-molecule aggregation (clustering) at high RH.[221-223, 235] As summarized in the **Table 5-7**, the specific sites capacity (Q_0) of pGO membrane, *i.e.* the monolayer water is found to be significantly smaller than that of pristine GO membrane.

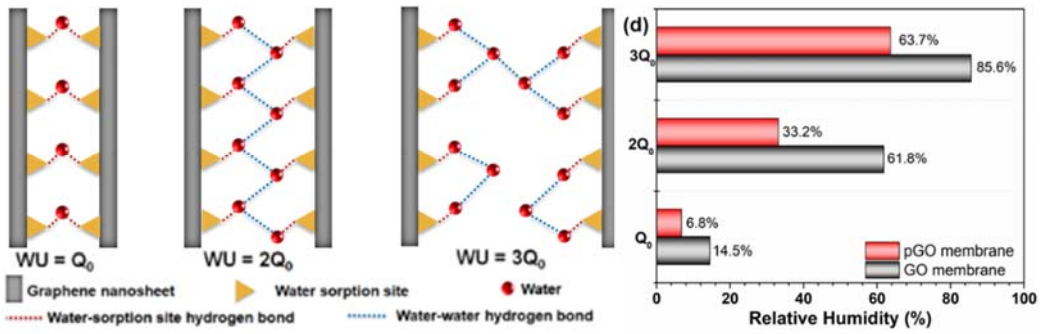

Figure 5-11. Schematic depicting the assumptions associated with using Park's Model for fitting the DVS isotherm when (a) WU = Q_0, (b) WU = $2Q_0$, and (c) WU = $3Q_0$. (d) Bar graph of active Q_0 at different relative humidity for GO and pGO membrane.

This is likely related to the reduction of the nanosheet size and addition of large holes on the nanosheets, where the continuous sandwich-like water monolayer adsorption is reduced

(**Figure 5-11a**).[236] Correspondingly, the required RH for the saturation of the water monolayer on specific water sorption site is only 6.8% for pGO membrane as opposed to 14.5% for GO membrane (**Figure 5-11d**). When the RH is raised, the water molecules will start to fill in the interlayer space of nanosheets and gradually form multilayer water. Meanwhile, the water-water hydrogen bonds start to form while the number of hydrogen bonds of the water-functional groups remain the same. When the second layer of water molecules forms, the oriented hydrogen-bond network (HBN) forms (**Figure 5-11b**). Such HBN orientation demonstrates a high aspect ratio along with the GO/pGO nanosheet, *i.e.* high structural anisotropy. With increasing amounts of water molecules adsorbed into the membrane at high RH, the water molecules tend to fill in the interlayer spaces in a distinct bimodal distribution, *i.e.* close to the nanosheets and a low population in the center (**Figure 5-11c**).[236-238] When the adsorbed water reaches the amount of $\mathbf{3Q_0}$, the actual number of water layers will exceed three layers (**Figure 5-11c**). The water molecules at the center, between the interlayers, are less bonded or oriented by the specific sites on the nanosheets, which are akin to bulk water with near-isotropic structure and properties, resulting in the anisotropy decrease of HBN. Therefore, when bilayer water (WU = $\mathbf{2Q_0}$) is formed in GO and pGO membranes, the anisotropy of HBN reaches its peak. The corresponding RHs at which GO and pGO form the bilayer water are found to be 33.2 % and 61.8 % according to **Figure 5-10g & Figure 5-11d**, respectively, explaining the anisotropy peaks in the proton conductivity at 40% and 70% RH for pGO and GO membranes.

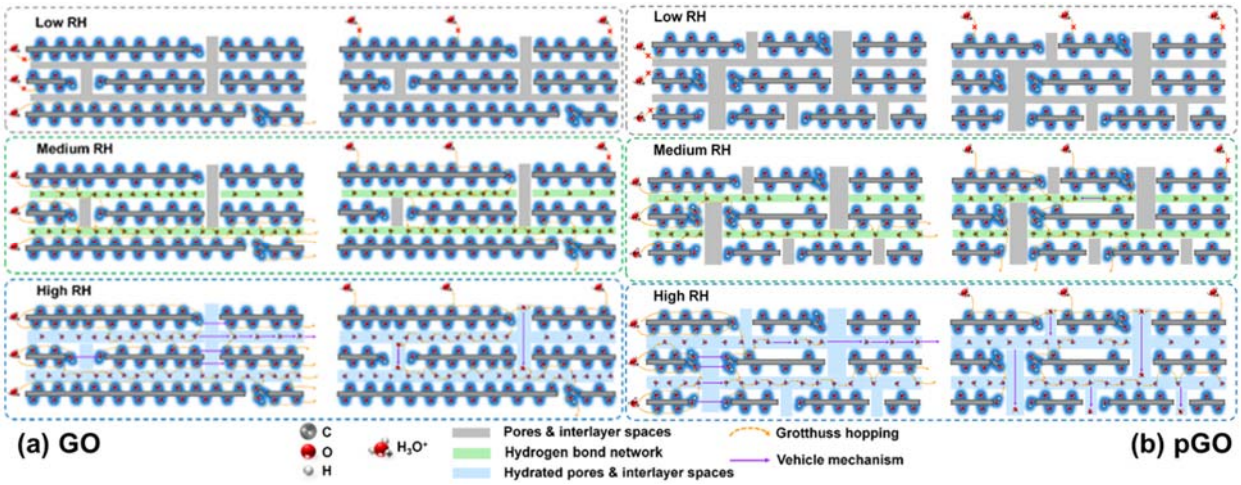

Figure 5-12. Proton conducting mechanisms at in-plane (left) and through-plane (right) directions of pGO membranes at low, medium and high RH conditions.

When the analyzed chemical structure and the morphological changes are followed, the RH-dependent degree of anisotropic proton conduction can be described by the schematics in **Figure 5-12**. Under a low RH environment, the gaps in the pores and in the interlayers of a pristine GO membrane are vacant (**Figure 5-12a**), causing insignificant proton conduction in both directions. However, in the in-plane direction, the high-density epoxy groups on the GO surface behave as the charge carriers, allowing protons to travel along the surface *via* hopping.[126] Likewise, pores on nanosheets and the interlayers in the pGO membrane are also void at low RH conditions (**Figure 5-12b**). However, the increased amount and size of pores frequently interrupt the chain of proton-hopping *via* the epoxy groups, leading to a decreased in-plane proton conductivity and degree of anisotropy.

When RH increases, the sub-nanometer interlayers of nanosheets begin to be filled with water molecules, especially between the hydrophilic regions of two GO nanosheets. Those highly hydrophilic oxygenated groups on the surface, mainly epoxy groups start to form an oriented HBN together with the water molecules. This oriented HBN plays an essential role in the anisotropic proton conduction in the GO membrane. As depicted in the **Figure 5-12a**, protons tend to hop through the HBN along the in-plane direction. As the distance between water molecules are shorter than that between epoxy groups, the frequency of hydrogen-bonding rearrangement among water molecules is much faster and the associated activation energy is reported to be lower.[239] Therefore, instead of hopping between epoxy groups, protons tend to migrate through the hydrogen bonded “water interlayer”. This sub-nanometer “water interlayer” also has a high aspect ratio, favoring the in-plane proton conduction. Moreover, the backbone of graphene nanosheets is highly impermeable to most small molecules, including water molecules. Thus, protons must migrate to the edge of pores or gaps between adjacent nanosheets to reach the next layer instead of travelling through the nanosheets. Meanwhile, with only the assistance of hydrophilic function groups such as hydroxyl groups, protons could travel through the nanosheet *via* “proton shuttling”.[240] Considering that a GO membrane with a thickness of 20 μm consists of up to 20,000 layers of GO nanosheets, the possibility to form a continuous HBN through all 20,000 layers to allow proton migration from one side to the other side is quite small. Accordingly, any GO layers with clean edges or insufficient epoxy-bonded water will also hinder or block the through-plane ion transport, leading to a low through-plane proton conductivity. Therefore, it is reasonable that the degree of anisotropic proton conduction increases significantly at medium RH. Likewise, the sub-nanometer interlayers within the pGO membrane change into the “water interlayers” at medium RH (**Figure 5-12b)**. But it is not as continuous as that in the pristine GO membrane. This is not only attributed to the existence of

extra pores on the pGO nanosheets, but also due to the reduced amount of epoxy groups on the surface, which serve as hoping sites and charge carriers. Thus, the discontinuous HBN significantly lowers the chance for a proton to freely migrate along the in-plane direction. As depicted in **Figure 5-12b**, a proton has to travel through one or more layers *via* the edge of nanosheets to complete the in-plane conduction pathway. Therefore, the anisotropic proton conduction *via* the “water interlayers” is noticeably hindered, leading to the low in-plane proton conductivity. At the same time, due to more pores and more hydrophilic groups at the edges, the through-plane proton conducting pathway is significantly shortened and the chance of a proton to migrate through the membrane is significantly increased. As a result, the increase in the degree of anisotropy at medium RH for pGO membrane is quite limited. Moreover, the discontinuous HBN within pGO membrane requires a lesser amount of absorbed water molecules from the environment in comparison with the GO membrane. This could explain why the peak of anisotropic proton conduction in a pGO membrane appears at lower RH as opposed to that in a GO membrane.

When both GO and pGO membranes are placed in a humid environment, the excessive water molecules will accumulate and fill the nano-size pores and gaps (**Figure 5-12**). According to TEM images, since the pore sizes are much larger than the length of hydrogen bonds formed between the oxygenated groups at the edges and water molecules, the excessive water molecules within the pores are considered as the “free water”. Thus, a proton can bond with a water molecule to form a hydronium ion and carry the proton to travel across pores or gaps *via* the vehicle mechanism. As a result, the in-plane proton conductivity is further increased for the GO membranes. Meanwhile, the free water molecules in the pores could also carry protons to travel through one or more layers of GO nanosheets, resulting in a significantly decreased, proton conduction pathway. Moreover, the free water molecules could also behave as oxygenated groups at the “clean” edges of the GO nanosheets, which can complete the HBN and enable more protons to participate in the through-plane proton conduction. Consequently, the through-plane proton conductivity increases significantly, and the degree of anisotropy decreases at high RH. For pGO membranes, free water molecules start to fill in the numerous and enlarged pores at relatively lower RH environments as opposed to GO membranes Those free water molecules complement the discontinuous HBN to complete an in-plane proton conduction pathway for facilitating protons *via* the vehicle mechanism (**Figure 5-12b**). In consequence, this is reflected by the increased in-plane proton conductivity at high RH with high activation energy. Similarly, for the through-plane direction of pGO membranes, the “free water” molecules which accumulated in the numerous pores and enlarged gaps act as the charge

carriers to migrate protons through pGO nanosheets *via* the vehicle mechanism. In comparison with GO membranes, the extra nanopores on the pGO nanosheets significantly shorten the proton conducting pathway, *i.e.* the tortuosity, which is in agreement with the mobility results in **Table 5-4**. Besides, it provides protons with more conducting pathways to travel through the membrane, implying an increased chance for a proton to complete the proton conduction through the membrane. As bulk water is isotropically proton-conducting, the more "free water" that is absorbed into the pGO membrane, the lower the degree of anisotropy is achieved for pGO membrane at high RH in **Figure 5-12b.**

5.3.2 Alcohol Fuel Cell Sensor Application

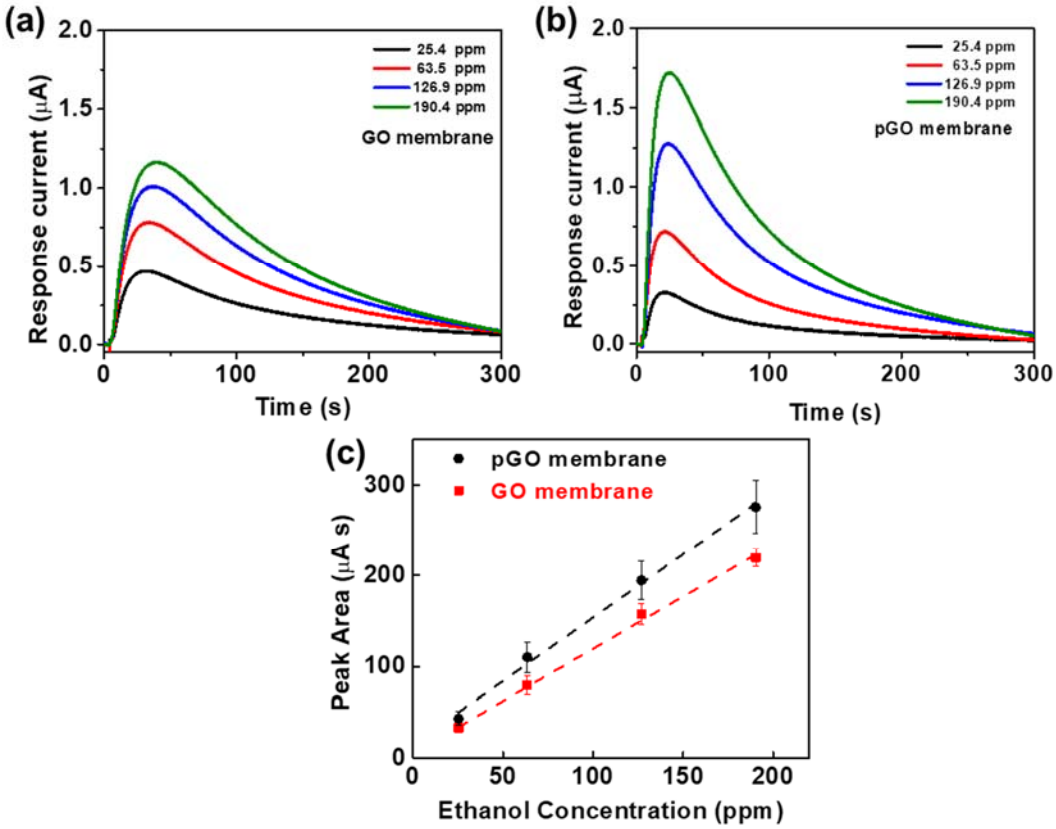

Figure 5-13. Response curves of (a) GO-based, and (b) pGO-based AFCSs, to ethanol vapor with different concentrations; (c) linear curve of peak areas as a function of ethanol vapor concentration.

To validate the potential of the pGO membrane as a practical and reliable proton-conductive membrane, alcohol fuel cell sensors (AFCSs) based on both GO and pGO

membranes were fabricated and compared. The typical response curves of AFCSs fabricated with GO and pGO membranes to ethanol vapor are displayed in **Figure 5-13**, showing a larger peak area for the pGO membrane-based AFCS as opposed to the GO membrane-based AFCS. This is attributed to the higher through-plane conductivity of pGO over that of the GO membrane. **Figure 5-13a, b** illustrate the response variation of pGO-based and GO-based AFCSs along with the change of ethanol vapor's concentration, respectively. Although both AFCSs show responses towards ethanol vapor as low as 25.4 ppm, the responses of pGO-membrane-based AFCS are superior to those of GO-membrane-based AFCS at all ranges of ethanol vapor concentration. To compare the alcohol sensitivity level of each membrane, according to the literature,[209, 210] the integrated peak area under each response curve was calculated and depicted in the inset of **Figure 5-13c**. Similarly, both pGO and GO membrane based ACFSs appear to have a linear relation with ethanol vapor concentration, whereas, the larger slope of pGO-based AFCS compared to that of GO-based AFCS indicates a better sensitivity from the former sensor.

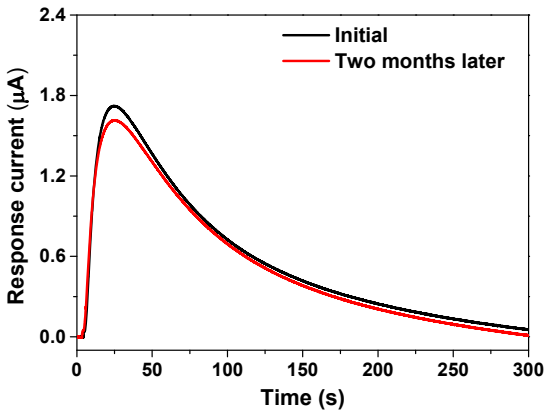

Figure 5-14. Ethanol response curves (at 190.4ppm) of AFCS equipped with a pGO membrane measured at initial and two months after the initial test

Practically, after two months, the pGO sensor demonstrates a near-invariable response from the initial test (**Figure 5-14**), which attests to its excellent stability. The desired superior sensitivity for pGO-based AFCS is attributed to the enhanced through-plane proton conductivity of the near-isotropic proton-conducting pGO membrane.

5.4 Chapter Conclusion

In this chapter, a reformed strategy to selectively improve the through-plane proton conductivity of a GO membrane is proposed and fulfilled *via* decreasing the degree of anisotropic proton conductivity with the pore formation on the GO nanosheets by SA-Fenton reaction. The environmentally benign, effective and scalable method to prepare porous GO nanosheets combines hydroxyl radical etching and sonication radiation, resulting in a pore-formation process akin to the step-growth polymerization. The obtained pGO membrane shows a much lower degree of anisotropy than that of the pristine GO membrane at all testing environmental conditions. In fact, the pGO membrane was found to possess a near-isotropic proton conduction at 100% RH and room temperature. Moreover, the unveiled Arrhenius' relationship of the degree of anisotropy with temperature and the volcano-shape relationship of that with RH suggest the degree of anisotropic of proton conductivity for pGO membrane could be further reduced at low temperature and high RH. It is also found that the interesting anisotropy behavior for both pGO and GO membrane in different environments is strongly correlated to the water interlayer bonded in the oriented HBN between nanosheets. Lastly the selective enhancement in the through-plane proton conductivity of the pGO membrane is evidenced by its retained, low ethanol detection limit, and superior ethanol selectivity and response in AFCS that employed pGO membrane as the solid proton-conductive electrolyte.

Chapter 6: Superior Proton Conductivity in Phytic Acid-doped Porous Graphene Oxide

6.1 Introduction

Graphene oxide (GO) is a prominent two-dimensional material that is comprised of sp^2-hybridized carbon atoms and oxygenated functional groups decorated on its basal plane and edges. Bestowed with an abundance of oxygen-functional groups, this atom-thick material is electrically insulating, highly dispersible in water, and allows for facile processing and abundant active sites for further chemical modifications.[241-243] GO nanosheets can self-assemble into free-standing membranes equipped with intrinsic pores on the nanosheets and interlayer galleries that act as selective sieves to promote fast transport within the channels. These characteristics of GO membranes prompted researchers to evaluate their applications in electrochemical storage and conversion devices[196, 244-249], chemical detection,[250] water purification,[243, 251-257] gas separation,[258, 259] and healthcare.[260] However, challenging drawbacks of GO such as relatively low proton conductivity, self-aggregation and long proton pathways have hindered this material from being utilized commercially.

To overcome these drawbacks, two general approaches have been proposed to enhance the proton conductivity of GO membranes *via* either surface modification of GO itself or doping small proton-conducting moieties. One example of GO surface modifications, which entails the reduction of the proton pathway, include employing steam to hydrothermally etch GO sheets; this modification resulted in a partially reduced porous graphene oxide with etched edges and the occasional defect on the basal plane.[33] In another report, Gao *et al.* prepared ozonated GO, which possessed a greater number of oxygen-containing functional groups and pinholes, as well as smaller sheet sizes.[9] More recently, Meguro *et al.* oxidized GO by subjecting commercial GO to Hummer's method, which yielded a deeply oxidized GO with increased carbon defects.[261] In the previous chapter, we reported on an environmentally benign and scalable method of utilizing sonication-assisted Fenton reaction to initiate hydroxyl radicals that can further oxidize GO.[262] In the aforementioned examples, additional pores, which were formed on the GO surface, enhanced the proton mobility, and ultimately improved through-plane proton conductivity. The other approach to improving the proton conductivity include doping small molecules,[56, 59, 123] or grafting functional groups onto the GO matrix, such as sulphates,

phosphates, *etc.*[261, 263-270] Incorporating phosphates has been shown to be quite advantageous due to its high charge carrier concentration, excellent proton conductivity with minor dependence on water, and good thermal stability.[271] Phosphate groups can assume either roles of proton acceptor and proton donor *via* self-dissociation; this property is particularly useful for increasing the density of protons at low relative humidity (RH) and for maintaining the hydrogen bond networks.[272] For example, phosphoric acid is typically doped into polybenzimadazole[273] or imbibed into metal organic frameworks (MOFs)[274] as a proton-conduction group even in anhydrous conditions.[275, 276] The drawbacks of phosphoric acid functionalization include acid leaching, membrane degradation and stack durability; these disadvantages will limit the practical use of phosphorylated GO matrices.[277]

Phytic acid (PA), also known as inositol hexakisphosphate, is an organic phosphate compound that is commonly derived from plant food products and seeds. Due to its low cost, natural and renewable source, abundance, limited toxicity, excellent biocompatibility and chemical/thermal stabilities, it is often incorporated into other food products, chemicals, biosensors, anticorrosion coatings, cation exchange resin, pharmaceuticals, energy storage and conversion, and other scientific research fields.[271, 278-281] PA contains six phosphoric groups, which has attracted many researchers into incorporating this moiety into membranes. Zhen *et al.* impregnated a MOF, MIL-101, with PA *via* a vacuum-assisted method, then utilized it as a filler for Nafion in order to generate a hybrid proton exchange membrane.[271] Although the thermal stability decreased slightly, all of the hybrid membranes exhibited higher proton conductivities than pristine Nafion. In another study, Cai *et al.* prepared a hexaphosphoric MOF called JUC-200 through reacting zinc with PA as the ligand.[282] JUC-200 was then incorporated into polyvinyl alcohol as the proton conductor for the water/acid-stable composite membrane. Lastly, the amphiphilic properties of PA originating from its hydrophobic aromatic domains (inositol triphosphate) and hydrophilic functional groups (phosphoric acid) can form strong π-stacking interactions, which makes PA quite compatible with GO.[283, 284]

Given these considerations, we employed sonication-assisted (SA) Fenton reaction, followed by PA functionalization on GO. In the final step of the SA-Fenton reaction, the dialysis step was omitted since PA can chelate and remove the residual iron ions in the subsequent filtration step. The use of PA is favorable towards creating a functionalized GO that possesses the following unique combination of advantages. Firstly, PA, which contains 12 acidic (exchangeable) protons on six phosphate groups, holds the highest number of phosphate groups content (except for phosphoric acid).[271, 278, 280, 281] It acts as a powerful chelating and

cross-linking agent, which can strengthen the stability of multilayered films,[279, 285] while it can also aid in the purification of residual metallic ions (*i.e.* residual Fe ions from the Fenton reaction). For any persistent, residual iron ions that remained in the matrix, PA can form an iron-phytate complex that lacks iron-coordinated water, and disables the formation of more hydroxyl radicals through the Fenton and Haber-Weiss cycle.[286, 287] Lastly, PA is abundant and will preserve the environmental benignity of the SA-Fenton reaction. The resulting free-standing phytic acid-doped porous graphene oxide membrane (PA-pGO) manifested substantial enhancements in the proton conductivity compared to pristine GO. More specifically, the through-plane conductivity reached up to 0.37 mS cm^{-1} at 25 °C and 100 %RH, which correspond to an improvement of 177% and 265% over pGO and GO, respectively. The practicality of a PA-pGO membrane was evaluated in an alcohol fuel cell sensor, which exhibited a superior response especially in comparison to the GO and pGO membranes. These successful results testify that PA-functionalization is an effective approach to reliably enhance pGO membranes and the feasibility of using PA-pGO membrane as a reliable solid electrolyte membrane in future energy storage systems and gas sensors.

6.2 Experimental Section

Graphite powder (2-15 μm) was procured from Alfa Aesar (MA, USA). Sulfuric acid (H_2SO_4, 98%), potassium permanganate ($KMnO_4$, 99%), sodium nitrate ($NaNO_3$, 99%), hydrogen peroxide (H_2O_2, 30%), hydrochloric acid (HCl, 37%), iron (II) sulfate heptahydrate ($FeSO_4 \cdot 7H_2O$, 99%), and phytic acid solution ($C_6H_{18}O_{24}P_6$, 50 wt% in H_2O) were purchased from Sigma-Aldrich (ON, Canada).

6.2.1 Graphene Oxide (GO) Synthesis

GO was prepared by Modified Hummers method.[17] Typically, graphite powder (2 g) was mixed with $NaNO_3$ (1 g) in concentrated sulfuric acid (46 mL), while held in an ice bath. After complete dispersion, $KMnO_4$ (6 g) was slowly added in 2 g aliquots, under vigorous mixing. Meanwhile, the temperature was maintained below 20 ^{0}C. The ice bath was then removed, while allowing the mixture to stir for another 2 h. DDI water (140 mL) was gradually added resulting in a violent effervescence. The mixture was allowed to stir for another 30 mins. Subsequently, the mixture was further diluted with DDI water (120 mL), then reacted with H_2O_2 (40 mL), resulting in a bright, golden yellow color. For purification, the GO solution is initially

filtered and washed with diluted HCl (2 L, 5%), followed by a wash with copious amounts of water *via* centrifugation (at 4000 rpm) until a pH of 4.0 was achieved. The resulting GO solution was diluted to approximately 10mg mL^{-1} for further use.

6.2.2 Synthesis of Porous Graphene Oxide (pGO)

The synthesis of pGO was based on the previous chapter[262] that utilizes sonication assisted (SA) Fenton reaction to generate hydroxyl radicals to further oxidize GO. In this process, $FeSO_4 \cdot 7H_2O$ (0.5 mg) was dissolved into DDI water (1 mL) and drop-wise added to the GO solution (0.4 g mL^{-1}, 100mL) under vigorous stirring, then left to stir for another 30 min. Diluted H_2O_2 solution (1.6%, 20 mL) was also drop-wise added into the GO solution under vigorous stirring, and then left to stir for 1h. The resultant solution was placed in a high frequency sonicator (44 kHz) for 12 h to accelerate the oxidation process that yielded pGO (solution). As a control, the PA-GO membrane utilized a GO solution that was prepared similarly, but omitting the addition of H_2O_2 and sonication.

6.2.3 Synthesis of Phytic Acid-doped Graphene Oxide (PA-GO) and Phytic Acid-doped Porous Graphene Oxide (PA-pGO)

Phytic acid (421 nL) was firstly diluted in DDI water (1 mL) and mixed for 15 min before dropwise-adding into the pGO solution under vigorous stirring. The mixture was mixed for another 30 min to ensure a thorough dispersion.

6.2.4 Membrane Fabrication

PA-GO and PA-pGO membranes were prepared through vacuum filtration casting. Initially, GO (1 mg mL^{-1}, 5 mL) was dispersed then pre-deposited onto a filter membrane (Polyether sulfone, PES, 200 nm) to ensure ethanol impermeability. Subsequently, either a PA-GO or PA-pGO suspension was poured on top and left to cast. GO and pGO membranes were prepared similarly with their respective suspensions (0.4 mg mL^{-1}, 100 mL) and were also casted on a PES membrane.

6.2.5 Physicochemical and Electrochemical Characterizations

The microscopic images were taken by a scanning electron microscopy (SEM, LEO FESEM1530) and a transmission electron microscope TEM (TEM, JEOL 2010F). The elemental maps were produced by energy-dispersive X-ray spectroscopy (EDX, LEO FESEM1530), while the elemental composition was semi-quantitatively measured by EDX and X-ray photoelectron spectroscopy (XPS, Thermo Scientific Al K-α X-ray source). The chemical structure of the functional groups was characterized by XPS and Fourier-transformed infrared spectroscopy (FTIR, Thermo Nicolet NEXUS 670). The crystal structure and defect density were measured by X-ray diffraction (XRD, Rigaku Miniflex 500) and a Raman microscope (Bruker Senterra, 532 nm laser).

The through-plane conductivity was measured *via* AC electrochemical impedance spectroscopy (EIS, Princeton Versastat MC Potentiostat). More specifically, the EIS was conducted between 100 kHZ to 1 Hz with a perturbation signal amplitude of 100 mV in various environmental conditions. After the membranes were synthesized, their thickness were measured with a micro-caliper. Thereafter, the proton conductivity was measured by sandwiching the membrane between two overlapping Pt current collectors. The sandwiched membrane was placed within an environmental chamber where the membrane was left to equilibrate at each environmental condition prior to measuring conductivity. The environmental conditions consisted of varying the relative humidity (RH) at room temperature (25%, 40%, 55%, 70%, 85%, 100%), followed by varying the temperature at 100 %RH (25 ^{o}C, 30 ^{o}C, 35 ^{o}C, 40 ^{o}C, 45 ^{o}C, 50 ^{o}C). The conductivity was measured *via* **Equation (3-11)**. The activation energy was derived from the Arrhenius relationship provided in **Equation (3-12)**. Therefore, the activation energy can be derived from the slope when the proton conductivity is plotted on a plot of $ln\ \sigma_0$ *vs.* $1000/T$.

6.3 Results and Discussion

6.3.1 Physicochemical Characterizations & Functionalization

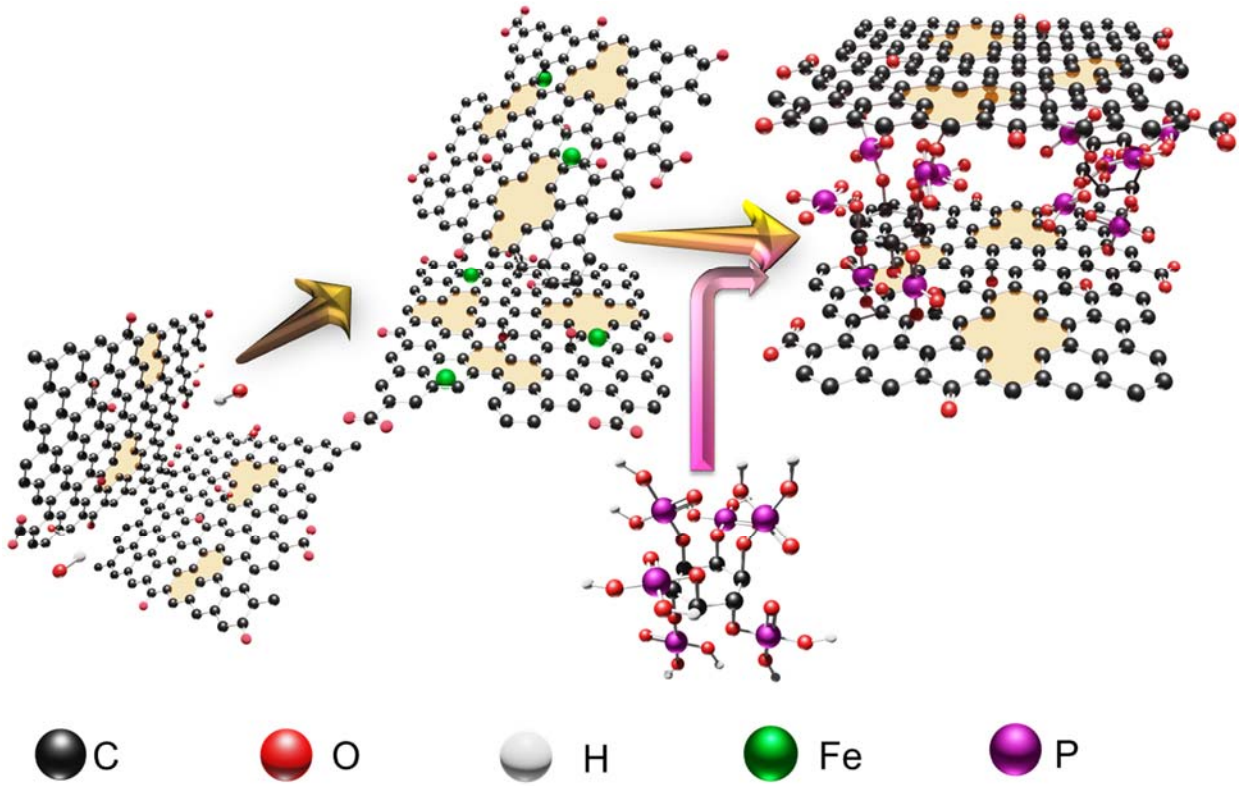

Figure 6-1. Preparation of PA-pGO membrane *via* Fenton reaction and functionalized with phytic acid

Figure 6-1 depicts the preparation procedure of the proton conducting phytic acid-porous graphene oxide (PA-pGO) membranes. Sonication-assisted Fenton (SA-Fenton) reaction was employed on graphene oxide (GO) to generate a porous graphene oxide (pGO) solution. The Fenton reaction generated highly oxidizing hydroxyl radicals from H_2O_2 in the presence of trace amounts of the Fe^{2+}/Fe^{3+} redox-couple. These radicals induced further oxidation and formation of additional pores on the GO nanosheets. The post-oxidation process involved vigorously mixing dilute phytic acid (PA) into the solution. Notably, the final step of dialyzing the pGO solution was omitted in favor of allowing the added PA to chelate and to remove residual Fe^{2+}/Fe^{3+} ions in the subsequent filtration process. Prior to the filtration process, a PA-pGO suspension was synthesized.

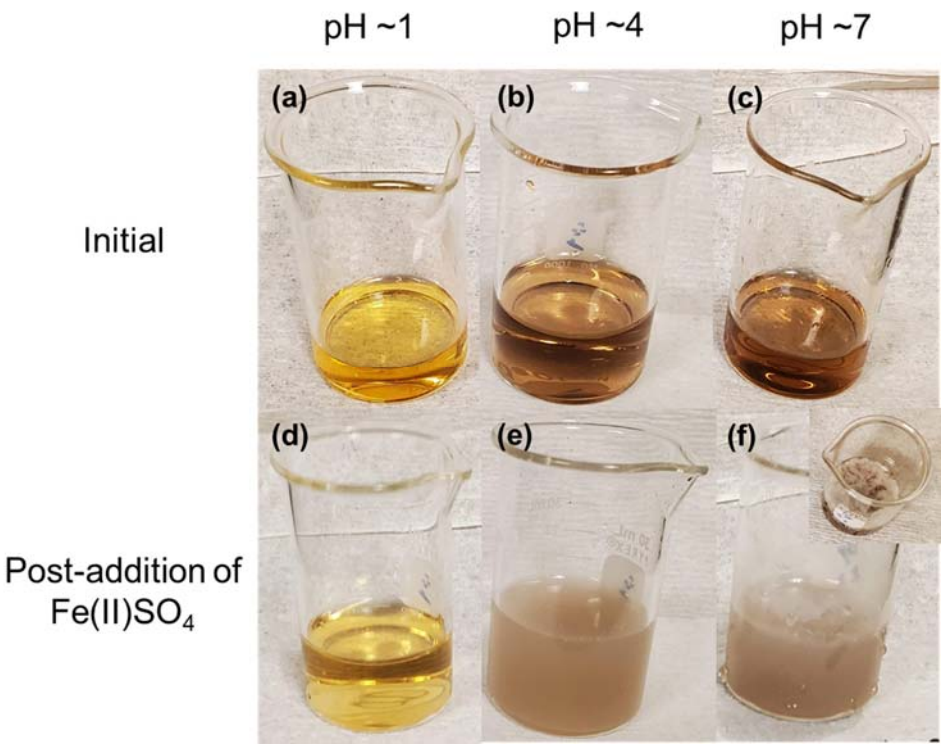

Figure 6-2. Photographs of dilute phytic acid with pH adjusted to (a) pH ≈ 1, (b) pH ≈ 4, and (c) pH ≈ 7 (inset: immediate reaction to addition of $Fe(II)SO_4$), and (d-f) the corresponding states when concentrated $Fe(II)SO_4$ solution was added.

To affirm that iron phytate-complexes were actually forming, a supplementary investigation was conducted, as shown in **Figure 6-2**. It is widely known that treating iron-ion containing compounds (*i.e.* $Fe(II)SO_4$) with hydroxide ions (*i.e.* NaOH) will result in the formation of a bluish-green, insoluble precipitate, iron(II) hydroxide. Thus, this investigation was initiated by mixing equal amounts of PA solution and DDI water (**Figure 6-2a**). Dilute NaOH solution was titrated into PA until the pH ≈ 4 (**Figure 6-2b**) and pH ≈ 7 (**Figure 6-2c**), wherein the solution color changed from a transparent yellow to a light, translucent brown and a dark, transparent brown color, respectively. Afterwards, concentrated $Fe(II)SO_4$ solution was drop-wise added into each phytic acid solution under vigorous mixing. The PA solutions at pH ≈ 1 and pH ≈ 4 readily dissipated, however its addition into the PA solution at pH ≈ 7 generated white cloud-like swirls on the solution-air interface, but readily dissipated after a few more seconds (**Figure 6-2f, inset**). After significant amounts of concentrated $Fe(II)SO_4$ solution was added, the PA solution at pH ≈ 1 remained a transparent yellow solution, (**Figure 6-2d**), whereas the solution at pH ≈ 4 became cloudy brown (**Figure 6-2e**), and at pH ≈ 7, the solution became cloudy brown with

white froth-like precipitate at the liquid-air interface (**Figure 6-2f**). At a pH ≈ 4, iron-phytate complexes were formed and were able to be removed *via* filtration.[288]

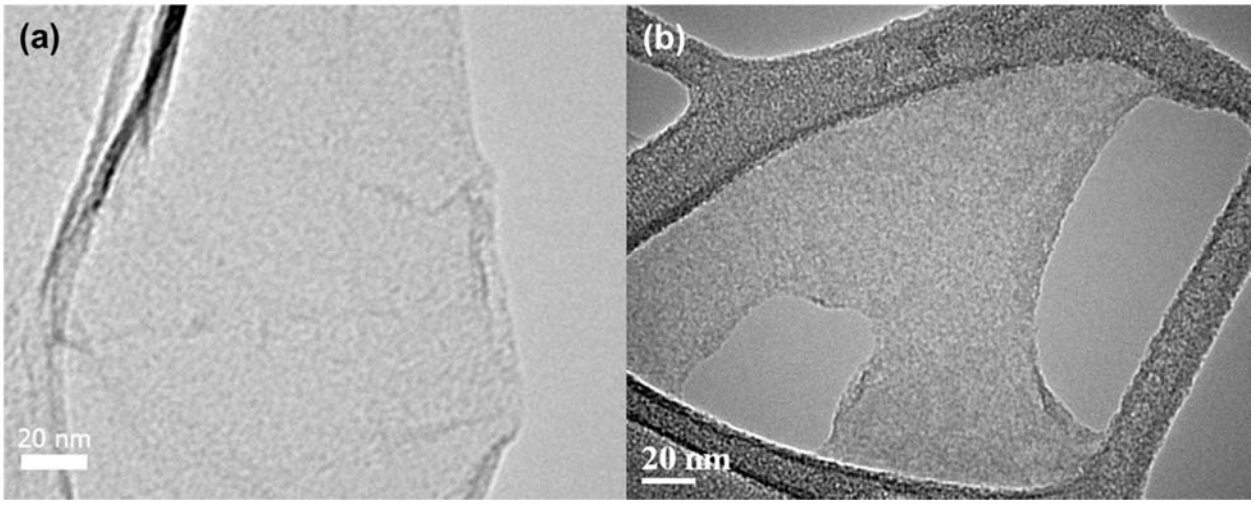

Figure 6-3. TEM Images of (a) GO and (b) pGO nanosheets

Supplementary transition electron microscopic (TEM) images of GO and pGO were taken as shown in **Figure 6-3. Figure 6-3a** showed no apparent pores on the GO sheets, whereas the ancillary pores were detected in **Figure 6-3b**, which affirmed the presence of pGO in the pGO containing samples.

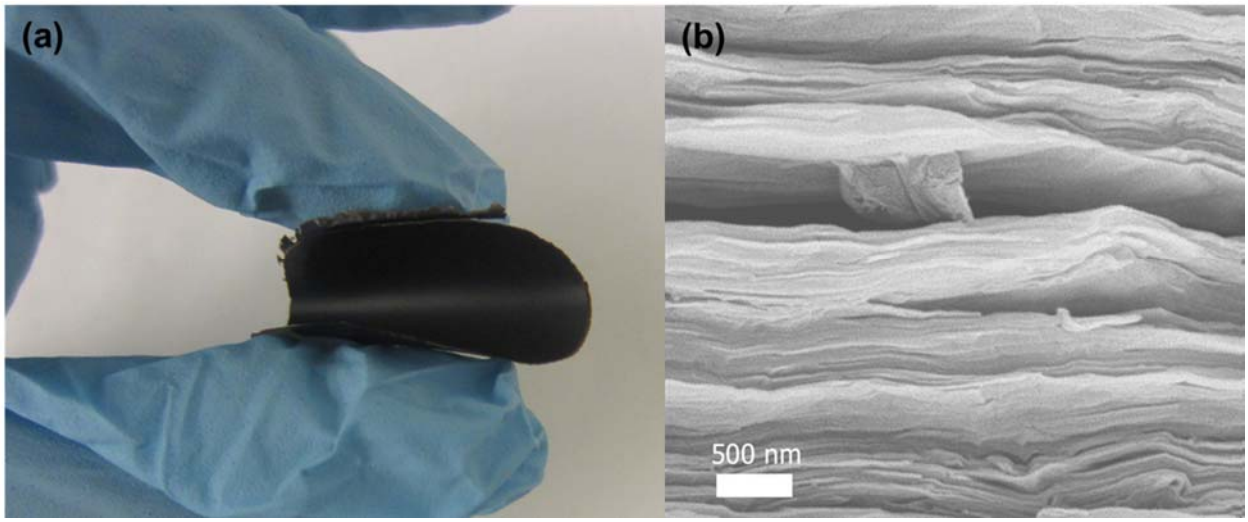

Figure 6-4. Photograph and SEM cross-section of GO membrane

The sample suspensions were filtered and casted into free-standing flexible membranes. A GO membrane was bended as demonstrated in **Figure 6-4a.** A typical staking morphology in a cross-sectional scanning electron microscopic (SEM) image is shown in **Figure 6-4b**.

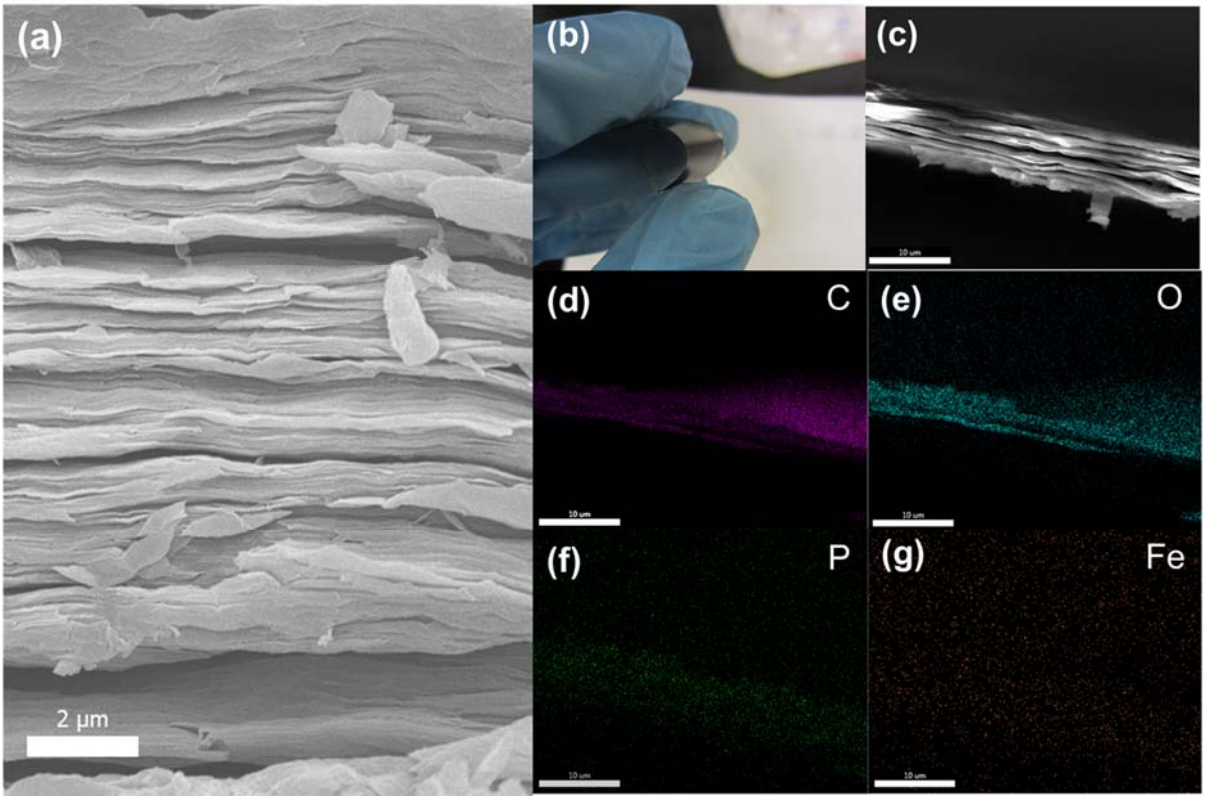

Figure 6-5. (a) Cross-sectional SEM, and (b) photographic image of flexible PA-pGO membrane. SEM and corresponding EDX maps of (d) carbon, (e) oxygen, (f) phosphorous, (g) and iron of the cross-section of PA-pGO membrane.

The PA-pGO suspension was filtration-casted into a free-standing flexible membrane exhibiting a stacked sheet morphology that was typical of GO membranes (**Figure 6-5a**).[125, 211, 262, 289] The digital picture of the PA-pGO in **Figure 6-5b** demonstrates a comparable bendability to a GO membrane (**Figure 6-4a**), indicating that the SA-Fenton reaction and PA functionalization did not affect its flexible behavior.

To confirm the presence and distribution of the various functional groups on PA-pGO nanosheets, a cross-sectional energy dispersive x-ray spectroscopy (EDX) mapping of PA-pGO was taken and shown in **Figure 6-5c-g**. P, which can only be found in the phosphate groups of PA, was homogenously distributed on the membrane, which confirmed that the functional group was present. Albeit possessing a weaker signal, the main distribution of P (**Figure 6-5f**) remains consistent with the shape of the membrane in the SEM image (**Figure 6-5c**) and to the color patterns outlined in the EDX spectra of C (**Figure 6-5d**) and O (**Figure 6-5e**). Although iron was required for the Fenton reaction, the lack of a coherent pattern in the EDX map of Fe (**Figure**

6-5g) attests to the successful formation of iron-phytate complex and its removal in the subsequent filtration process.

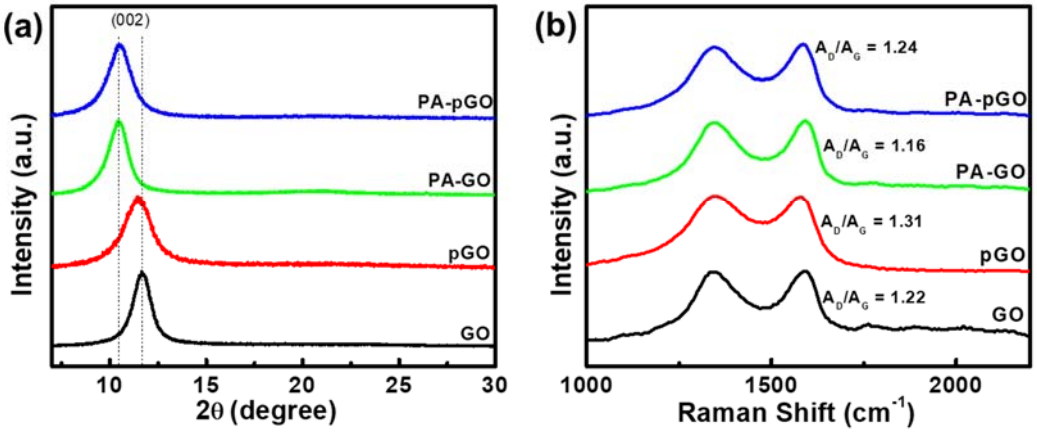

Figure 6-6. (a) XRD and (b) Raman spectra of GO, pGO, PA-GO and PA-pGO membranes

Table 6-1. Summary of values calculated from XRD Spectra

Sample	XRD			
	d-spacing, Å	FWHM	L_c	# of Layers
GO	7.58	0.02	72.93	9.62
pGO	7.87	0.03	54.93	6.31
PA-GO	8.34	0.02	58.91	7.06
PA-pGO	8.47	0.03	51.67	6.10

The structural differences among GO, pGO, PA-GO and PA-pGO were examined by X-ray diffraction (XRD) and Raman spectroscopy **(Figure 6-6 and Table 6-1)**. The XRD spectra reveals a major peak located at 11.66°, then a downshift to 11.12°, 10.60°, and 10.44° for GO, pGO, PA-GO and PA-pGO, respectively (**Figure 6-6a**). These observations translate to a d-spacing of 7.58 Å, 7.87 Å, 8.34 Å and 8.47 Å, respectively **(Table 6-1)**. Based on the Scherrer

equation, the stacking number of layers significantly decreased (9.62 for GO), firstly from the •OH radical oxidation (6.31 for pGO), then from PA-doping (7.06 and 6.10 for PA-GO and PA-pGO, respectively). Consistent with our previous work,[262] the oxidation *via* hydroxyl radicals enhanced the exfoliation of the GO layers, which weakened the π- π stacking between GO nanosheets and decreased the number of layers. Furthermore, the phytate intercalating between the nanosheets expanded the interlayer distance, which further weakened the π- π stacking, allowing us to effectively reduce the number of layers.

The Raman spectra (**Figure 6-6b**) indicated a perceptible change in the intra-layer structure in post-SA-Fenton reaction and PA doping processes. The ratio between the integrated area underneath the D-band (A_D, ~1340 cm^{-1}) to that of the G-band (A_G, ~1580 cm^{-1}), or the A_D/A_G ratio, is typically used to gauge the degree of defects and structural disorder.[99] In this case, the A_D/A_G ratio decreased after •OH radical oxidation, from 1.24 to 1.16 corresponding to GO and pGO, respectively. This can be rationalized by the further oxidation after subjecting GO to SA-Fenton reaction to induce more defects on the basal plane of pGO, which is in agreement with the XPS data (**Figure 6-7b, e**) that showed a decrease in the sp^2-hybridized C=C and an increase in the sp^3-hybridized C-C/C-H.[262] The addition of PA on the other hand, increased the areal ratio from 1.24 to 1.31 for GO to PA-GO and from 1.16 to 1.22 for pGO and PA-GO. The increase in the A_D/A_G is consistent with literature,[290-292] and can be attributed to the relatively large amount of phosphates that were added in contrast to the relatively fewer number of six-membered aromatic rings in PA.[293] Altogether, the XRD and Raman spectra confirms the successful oxidation of GO and functionalization of PA in PA-pGO membranes.

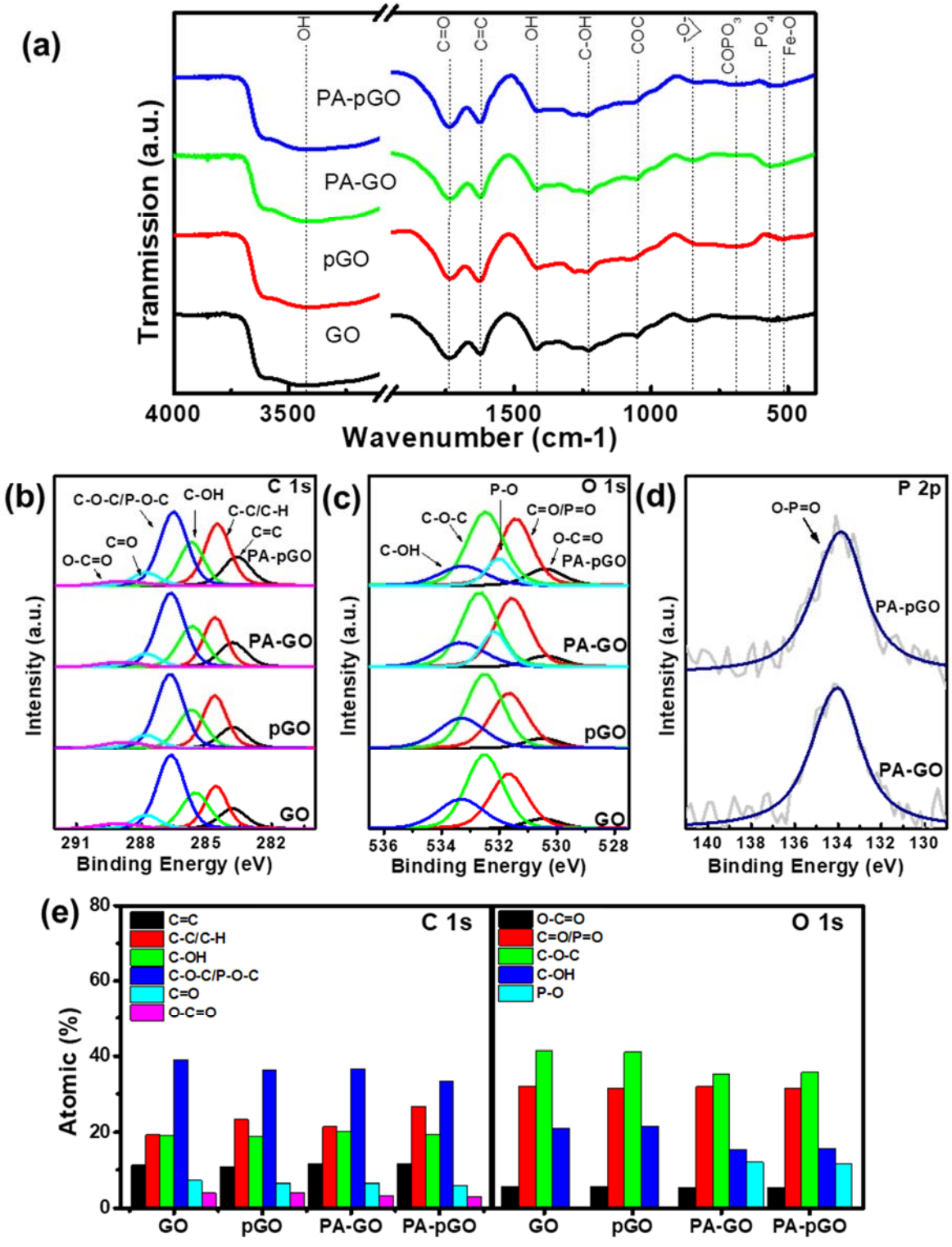

Figure 6-7. (a) FTIR and XPS spectra of (b) C 1s, (c) O 1s, and (d) P 2p for GO, pGO, PA-GO, and PA-pGO films

Table 6-2. Elemental composition of GO, pGO, PA-GO, and PA-pGO *via* EDX and XPS

Element	EDX				XPS			
	GO	pGO	PA-GO	PA-pGO	GO	pGO	PA-GO	PA-pGO
C	72.23%	67.30%	67.06%	65.77%	70.52%	69.46%	69.71%	69.52%
O	27.77%	32.66%	32.60%	33.93%	29.48%	29.75%	30.08%	30.34%
P	0.00%	0.00%	0.29%	0.22%	0.00%	0.00%	0.10%	0.07%
Fe	0.00%	0.04%	0.05%	0.08%	0.00%	0.79%	0.11%	0.07%

To confirm the effectual functionalization of PA onto GO and pGO, the Fourier-transformed infrared spectra (FTIR) of GO, pGO, PA-GO and PA-pGO membranes were collected and presented in **Figure 6-7a**. In the FTIR spectrum of GO, the characteristic peaks located at 3404, 1735, 1625, 1416, 1228, 1050, and 840 cm^{-1}, can be ascribed to the stretching of free hydroxyl (O-H), carboxyl (C=O), sp^2 carbon (C=C), deformation vibration of hydroxyl (O-H), and stretching of carbon-hydroxyl (C-OH), epoxide (COC), and epoxy ring, respectively.[56, 123, 211, 294-297] In the pGO spectrum, one additional peak located at 530 cm^{-1} was due to Fe-O bonds; the spectra confirmed the presence of residual iron.[298, 299] However, this peak disappeared in the PA-GO and PA-pGO spectra, which points to the removal of iron. In its stead, two newly emerged, but weak bands were found at 670 and 540 cm^{-1} which corresponded to $COPO_3$ and phosphate (PO_4^{3-}), respectively.[283, 300, 301] The appearance of these new peaks corresponding to P-containing functional groups indicated the successful functionalization of PA onto GO and pGO.

To understand the mechanism responsible for the PA functionalization, X-ray photoelectron spectroscopy (XPS) was employed on the free-standing membranes as shown in **Figure 6-7b-d**. The elemental composition obtained by XPS survey and EDX are presented in **Table 6-2**. Starting from GO, the pGO exhibited a slightly increased oxygen content, which was similar to the results of our previous report.[262] However, the increased iron content due to the lack of dialysis to remove the iron ions. In contrast to that of GO, PA-GO revealed not only a higher oxygen content, but also a higher phosphorus and iron content. The increase in the O, P, and Fe can be attributed to the addition of $Fe(II)SO_4$ and PA, which contained six phosphate groups. The PA-pGO manifested similar trends when compared to pGO (as GO to PA-GO) and

to PA-pGO (as to GO and pGO). Proceeding to the high-resolution spectra of C 1s in **Figure 6-7b**, the GO, pGO, PA-GO, and PA-pGO membranes showed the typical six peaks, namely sp^2-hybridized C=C (283.8 eV), sp^3-hybridized C-C/C-H (284.5 eV), C-OH (285.6 eV), C-O-C/P-O-C (286.6 eV), C=O (287.8 eV), and O-C=O (288.9 eV), which are in agreement with literature.[56, 211, 262, 296, 302-305] Four and five major peaks were identified in the O 1s spectra of the GO and pGO, and PA-GO and PA-pGO membranes, respectively (**Figure 6-7c**). The major peaks can be attributed to: O-C=O (530.5 eV), C=O/P=O (531.6 eV), C-O-C (532.7 eV), C-OH (533.3 eV) and P-O (532.1 eV), of which the P-containing groups only pertained to the PA-containing samples.[56, 211, 262, 296, 304, 306, 307] Lastly, only one major peak was identified in the P 2p spectra for PA-GO and PA-pGO, which corresponded to O-P=O (133.9 eV).[308, 309] Although the chemical bonds were similar throughout the different membranes, the differences will confirm the oxidation from the SA-Fenton reaction and unravel the mechanism to the PA functionalization.

When comparing the atomic percentage of functional groups in pGO and GO (**Figure 6-7e)**, there is a slight decrease in the sp^2-hybridized C=C, while the sp^3-hybridized C-C/C-H increases. This difference can be attributed to the oxidative addition/hydroxylation reaction with the •OH radicals on the C=C bonds, which resulted in the formation of many C-C/C-H bonds.[227, 262] The C 1s spectrum showed a slight decrease in C-O-C, C-OH and C=O groups while O-C=O faintly increased in percentage. The slight decrease in the C-O-C can be attributed to the hydroxylation in the ring-opening reaction on the epoxide groups, which generated hydroxyl groups. The phenols and alcohols can also undergo oxidation by the •OH radicals to form quinones and ketones/aldehydes, respectively.[227, 305]. Lastly, the aldehyde groups can be further oxidized into ester and/or carboxylic groups, which explains the slight increase in the O-C=O.[56, 227, 228] The differences that were observed between GO and pGO were apparent between PA-GO and PA-pGO.

In the C 1s spectrum of **Figure 6-7e**, there is a negligible change in the sp^2-hybridized C=C between GO and PA-GO, but a significant increase in the sp^3-hybridized C-C/C-H, which was attributed to the addition of PA, which at its center contains an inositol. A decrease in the C-O-C/P-O-C combined with an increase in the alcohols was due to the epoxide ring opening reaction in acidic aqueous media.[262] The slight decrease in the C=O and O-C=O was rationalized by a significant increase in the sp^3-hybridized C-C/C-H that originated from the addition of PA.

Considering the O 1s spectrum (**Figure 6-7e**), there was a large decrease in C-OH, but a negligible change in O-C=O that was due to the esterification of hydroxyl groups in acidic media, which produced ester groups to link the PA to the GO nanosheet. However, the mere addition of P-containing functional groups from PA offsets the increase in the O-C=O, which explained the insignificant change in C=O/P=O. As described previously, the decrease in C-O-C was resulted from the epoxide ring opening reaction. P-O was significantly increased from the addition of PA. The trends that was observed between GO and PA-GO was detected between pGO and PA-pGO, which demonstrated that the functionalization of PA was not significantly different between GO and pGO.

6.3.2 Electrochemical Characterizations

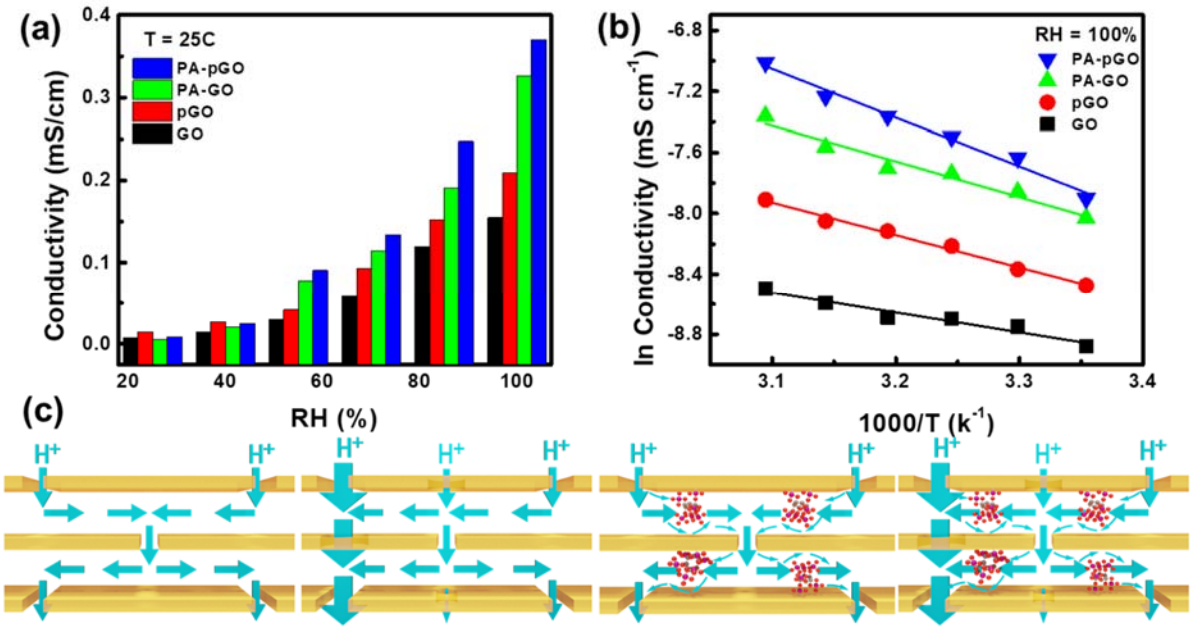

Figure 6-8. Through-plane conductivity as a function of (a) temperature, and (b) relative humidity. (c) Schematic of through-plane conductivity in GO, pGO, PA-GO, and PA-pGO membranes

The through-plane proton conductivity was measured at various environmental conditions by varying sequentially either the temperature or the relative humidity. Generally, the proton conductivities of GO, pGO, PA-GO and PA-pGO membranes (**Figure 6-8a, b**) improved with either an increase in the relative humidity or temperature. The pGO membrane

outperformed the GO membrane at all relative humidity and temperatures. For example, the through-plane conductivity of the pGO membrane was enhanced by 35% (0.21 mS cm^{-1}) and 80% (0.37 mS cm^{-1}), compared to that of the GO membrane under fully hydrated conditions and at 25 °C and 50 °C, respectively. As depicted in **Figure 6-8c**, this enhancement was explained by the shortened proton transport pathway that accompanied the enlargement and extra pore formation.[262] Subsequently, the PA-functionalized membranes outperformed their non-PA containing counterparts at all relative humidity and temperatures (**Figure 6-8a, b**). For instance, the through-plane conductivity of the PA-GO membrane outmatched that of the GO membrane by 133% (0.33 mS cm^{-1}) and by a significant 211% (0.63 mS cm^{-1}) under humidified conditions, at 25 °C and 50 °C, respectively (**Figure 6-8c**). This betterment was attributed to phosphonic groups on PA, which are known to possess high proton conductivity, even at low RH.[271, 300] The proton conductivity of PA-pGO exceedingly surpassed that of GO. In particular, the through-plane conductivity of the PA-pGO membrane was enhanced by 165% (0.37 mS cm^{-1}) and 342% (0.90 mS cm^{-1}) under fully humidified conditions, at 25 °C and 50 °C, respectively. The superior performance in the proton conductivity proved that the synergistic effects were derived from SA-Fenton reaction and PA-functionalization (**Figure 6-8c**); this approach was efficacious in enhancing the proton conductivity of GO-based membranes.

Table 6-3. Summary of activation energies calculated from the through-plane proton conductivity of GO, pGO, PA-GO, and PA-pGO membranes

Membranes	GO	pGO	PA-GO	PA-pGO
Activation Energy ($kJ\ mol^{-1}$)	10.9	17.8	19.4	26.5

Figure 6-8b presents a general trend for the GO, pGO, PA-GO and pGO membranes showing that the through-plane conductivity increased linearly as the temperature increased from 24 °C to 50 °C. To analyze the mechanism of proton conduction, Arrhenius plots for each membrane and their corresponding activation energy were calculated and summarized. Generally, Grothuss mechanism, which is also known as proton-hopping, dominates the proton conductivity when the activation energy is less than 12.55 kJ mol^{-1}.[45, 230] Alternatively, the vehicle mechanism involves the shuttling of positive ions, (*e.g.* protons) *via* a "vehicle" (*e.g.*

H_2O).[310] As indicated by **Table 6-3**, both the Grothuss-type mechanism and vehicle mechanism contributed to the proton conduction of GO, while the vehicle-type mechanism dominated the process for the pGO, PA-GO and PA-pGO membranes. The activation energy increased with either SA-Fenton oxidation or PA functionalization.

6.3.3 Alcohol Fuel Cell Sensor

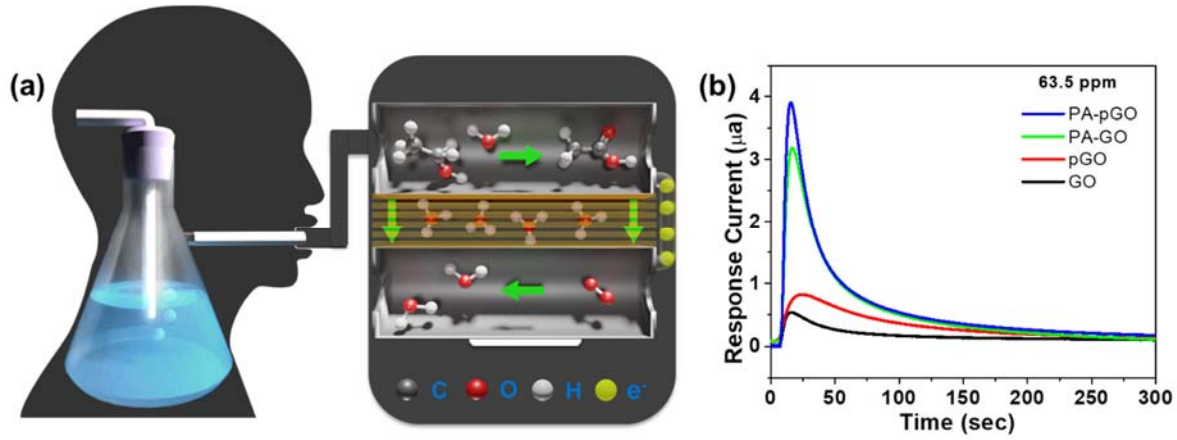

Figure 6-9. (a) Graphic of a breath simulator connected to an alcohol fuel cell breathalyzer. (b) Response curves of GO, pGO, PA-GO, and PA-pGO to ethanol vapor at 63.5 ppm

In order to evaluate the practical applicability of the free-standing GO, pGO, PA-GO and PA-pGO membranes, alcohol fuel cell sensors (AFCSs) based on each membrane were prepared and evaluated. Briefly as depicted in **Figure 6-9a**, warm ethanol breath was simulated by bubbling a fixed amount of air through an ethanol standard solution and injected into the housing electrochemical gas sensor, which simulates the intrinsic operation of a breathalyzer. The ethanol molecules diffused through the gas diffusion layer and adsorb onto a Pt/C catalyst triggering an ethanol oxidation reaction at the anode, and thereby producing protons, electrons and acetic acid. The electrons migrated through the external circuit to the cathode, whereas the protons (H_3O^+) migrated simultaneously through the electrolyte and the membrane to the cathode. Subsequently, oxygen reduction reaction utilized the protons, electrons, and oxygen from the air to generate water. The electrons that flowed through the external circuit were recorded by a connected multimeter to produce a response curve similar to that seen in **Figure**

6-9b. A typical response curve, like that displayed in **Figure 6-9b,** is comprised of a starting point, a peak indicating as to when the alcohol was initially detected, followed by the decay (recovery time). At 63.5 ppm, two small peaks representing the sensitivity of the GO and pGO membrane was observed in **Figure 6-9b**. Furthermore, a relatively large peak was attributed to PA-GO, and yet a larger peak was observed for PA-pGO, wherein increasing peak sizes were due to the increasing proton conductivities of pGO, PA-GO and PA-pGO, respectively. These results confirmed the superior response of GO membranes that had undergone SA-Fenton oxidation and PA functionalization.

6.4 Conclusion

The phytic acid-functionalized, porous graphene oxide (PA-pGO) membranes were fabricated *via* applying GO to the combination of sonication-assisted Fenton (SA-Fenton) reaction and functionalization with phytic acid (PA). The environmentally friendly procedure of preparing pGO utilizes •OH radical oxidation assisted by sonication radiation to increase the concentration of oxygen functional groups and pores on the GO sheets. This is followed by mixing the abundant and also environmentally benign PA prior to casting GO into a membrane. The PA capitalized on chelating and removing residual Fe ions, while enhancing the proton conductivity *via* anchoring phytate groups onto the surface of the GO nanosheet. The resultant PA-pGO membrane demonstrated superior proton conductivities in the through-plane direction up to 0.37 mS cm^{-1} and 0.90 mS cm^{-1}, which translated to a 265% and 342% enhancement over the GO membrane at 100 %RH and 25 ^{o}C and at 50 ^{o}C, respectively. Lastly, the synergistic effects of SA-Fenton oxidation and PA-functionalization were evidenced by the superior ethanol response in AFCS that employed the PA-pGO membrane as the solid proton-conductive electrolyte.

Chapter 7: Conclusion and Future Work

7.1 Summary and Conclusions

The primary objective of this thesis is to enhance the ionic conductivity of GO-based membranes. The secondary objectives include enhancing, or at least maintaining the chemical, mechanical, and chemical stability, and accommodating for the shift towards solid-state electrolyte membranes. Ensuring environmentally safe, inexpensive and scalable methods were also considered.

Ionic conductivity, specifically hydroxide-ion conductivity, was enhanced by functionalizing GO with an ionic liquid, 1-hexyl-3-methylimidazolium. Proton conductivity, especially the through-plane conductivity, was improved by utilizing two approaches. The first approach was based on further oxidizing GO *via* sonication-assisted (SA)-Fenton reaction, while the second approach involved functionalizing GO with phytic acid. Supercapacitor, Zn-air battery and alcohol fuel cell sensor prototypes developed using these technologies indicating a working proof-of-concept was feasible. The enhanced conductivity was attributed to the shorter diffusion pathways and increased oxygen functional groups. These developments open the door towards future commercialization of GO membranes.

7.1.1 Imidazole-doped Graphene Oxide for Enhanced Hydroxide Conductivity

Acquiring reliable and efficient wearable electronics requires the development of flexible electrolyte membranes (EMs) for energy storage systems with high performance and minimum dependency on the operating conditions. Herein, a freestanding graphene oxide (GO) EM is functionalized with 1-hexyl-3-methylimidazolium chloride (HMIM) molecules *via* both covalent and noncovalent bonds induced by esterification reactions and electrostatic πcation−π stacking, respectively. Compared to the commercial polymeric membrane, the thin HMIM/GO membrane demonstrates not only slightest performance sensitivity to the operating conditions but also a superior hydroxide conductivity of 0.064 ± 0.0021 S cm^{-1} at 30% RH and room temperature, which was 3.8 times higher than that of the commercial membrane at the same conditions. To study the practical application of the HMIM/GO membranes in wearable electronics, a fully solid-state, thin, flexible zinc−air battery and supercapacitor are made exhibiting high battery performance and capacitance at low humidified and room temperature environment, respectively, favored by the bonded HMIM molecules on the surface of GO nanosheets. The

results of this study disclose the strong potential of manipulating the chemical structure of GO to work as a lightweight membrane in wearable energy storage devices, possessing highly stable performance at different operating conditions, especially at low relative humidity and room temperature.

7.1.2 Near-Isotropic Proton-Conducting Porous Graphene Oxide Membrane

Graphene oxide (GO) membrane is an ideal separator for multiple applications due to its morphology, selectivity, controllable oxidation, and high aspect ratio of 2D nanosheet. However, the anisotropic ion conducting nature caused by its morphology is not favorable towards the through-plane conductivity, which is vital for the solid-state electrolytes in the electrochemical devices. Here, we present a strategy to selectively enhance the through-plane proton conductivity of a GO membrane by tuning down the degree of anisotropy using pore formation on the nanosheets by SA-Fenton reaction. The obtained porous GO (pGO) membrane is the first reported near-isotropic proton-conducting GO membrane, showing the degree of anisotropy as low as 2.77 and 47% enhancement of through-plane proton conductivity as opposed to the pristine GO membrane at 25^{o}C and 100 % relative humidity. The anisotropic behavior exhibited an Arrhenius relationship with temperature while the water interlayer formation between nanosheets played a pivotal role in the anisotropic behavior under different relative humidity (RH). In increasing RH, water molecules tend to orient in a bimodal distribution clinching onto the nanosheets and forming a sub-nanometer, high-aspect-ratio, water interlayer, resulting in its peak anisotropy. Further increase in RH fills the interlayer gap, resulting in behaviors akin to near-isotropic, bulk water. Implementation of the pGO membrane, as the solid proton-conductive electrolyte, in an alcohol fuel cell sensor was demonstrated, showcasing excellent selectivity and response, as well as linearity and sensitivity for ethanol detection with limits as low as 25 ppm. The amalgamation of excellent performance, high customizability, facile scalability, low cost, and environmental friendliness in the present method holds considerable potential for transforming anisotropic GO membranes into near-isotropic ion conductors for the furthering of membrane development and electronic sensory applications.

7.1.3 Superior Proton Conductivity in Phytic acid-doped Porous Graphene Oxide

Graphene oxide (GO) contains several oxygenated functional groups attached to its basal plane that allows for facile processing and an abundance of active sites for functionalization. Attempts have been made at surface modifications that include increasing the porosity and the oxygen functional groups on the basal planes and edges. The proton conductivity was lacking in these modifications for practical applications. Herein, a free-standing phytic-acid-doped porous graphene oxide (PA-pGO) was prepared by combining SA-Fenton reaction and PA functionalization to immensely enhance the through-plane proton conductivity. PA not only offers an abundance of phosphate groups to improve proton conductivity, but also acts as a powerful chelating agent to remove or deactivate residual iron ions left from the SA-Fenton reaction. Compared to GO and even the pGO membrane, the PA-pGO membranes demonstrates a superior protonic conductivity of 0.37 mS/ cm^{-1} at room temperature and at 100 %RH, which translated to 2.65 and 1.77 times higher conductivity than that of GO and pGO at the same conditions. To evaluate the feasibility of the GO membranes in practical applications, alcohol fuel cell sensor prototypes employing PA-pGO membranes as the proton-conducting electrolyte were developed highlighting the excellent selectivity and response. The results of this study revealed promising potential of functionalizing the structure of pGO to further enhance the proton conductivity especially at room temperature operations.

7.2 Future Work

The achievements reported in this thesis serves as a step towards the larger goal of commercializing graphene oxide (GO) composite membranes that can rival the current industry standards. It is suggested that the future work should either build upon or address any shortcomings in these processes. Further investigations should include 1) improving the mechanical stability in aqueous solvents (*e.g.* water), 2) accelerating and/or scaling up pGO production, and 3) capitalizing on anchored metal ions for greater phytate stability.

7.2.1 Enhancing the Mechanical Stability in Aqueous Solvents (*i.e.* water)

One of defining features of GO is its numerous oxygen-containing functional groups and surface defects located on the basal planes and edges, which enable its highly-favored

hydrophilicity. The preparation of pGO exploited this attribute by further increasing the number of surface defects and oxygen-containing functional groups. As an expected result, rate and capacity of the water uptake significantly increased (as compared to GO). This result was rationalized by the water molecules penetrating and filling the void spaces in pGO more easily than that of GO (at lower humidity). This superior attribute also implies that the process is reversible, since pGO was prepared by concentrating the pGO solution *via* filtration, *i.e.* pGO will disintegrate more easily in water. Consequently, dynamic vapor sorption was favored over the traditional method of measuring water uptake. By the traditional water uptake method, the processing of membranes requires soaking overnight in order to obtain the weight of a water-saturated membrane. By the time the pGO was ready to be weighed, the pGO membrane was hardly a membrane anymore. For applications that involved prolonged use of membranes in humidified environments (*i.e.* PEMFCs), efforts should focus on investigating additives that will improve the water stability of GO-based membranes, without compromising their ionic conductivity (*e.g.* cross-liking agents).

7.2.2 Accelerating and/or Scaling up pGO Production

The simplicity, scalability, environmental benignity, and low cost of preparing pGO set the tracks for scaling-up production from lab-scale to pilot-plant. One particular process in the pGO preparation involves concentrating and molding the pGO solution into a pGO membrane. This process is tedious and takes about 3 days for GO, and about one week for pGO. This long process is due to the GO (and smaller pGO) sheets filling up the pores of the filter membrane. As more pores were filled, there were fewer channels for water to filtrate through. Prior to scaling-up, it is highly recommended that the concentrating portion be quickened. One possible solution, inspired by Akbari *et al.*,[54] would be using hydrogel beads to concentrate the GO solution prior to doctor blading or filtration-casting the remaining nematic GO dispersion to form the membrane.

7.2.3 Capitalizing on Residual Metal Ions and Optimizing the Phytate Loading

In chapter 5, phytic acid (PA) is known to be a powerful chelator that is capable of binding to residual metal ions, especially those that were used in the previous SA-Fenton reaction. In this case, the iron ions that were floating in the solution were chelated by the PA

and removed in the subsequent filtration process. Herein, we propose the alteration of the procedure to first electrostatically anchor the iron ions to GO, then chelate the PA onto the iron ions. The iron ions act as additional active sites for PA to functionalize GO. Afterwards, an optimization for the PA doping can be conducted to maximize the proton conductivity, while ensuring that acid leaching is completely prevented (as is the case with excessing phosphoric acid doping).

References

1. Administration, U. S. E. I. Eia Projects Nearly 50% Increase in World Energy Usage by 2050, Led by Growth in Asia. https://www.eia.gov/todayinenergy/detail.php?id=41433 (accessed 2020/02).

2. Donarelli, M.; Ottaviano, L., 2d Materials for Gas Sensing Applications: A Review on Graphene Oxide, Mos2, Ws2 and Phosphorene. *Sensors* **2018**, *18*, 3638.

3. Brodie, B. C., Xiii. On the Atomic Weight of Graphite. *Philos. Trans. R. Soc. London* **1859**, 249-259.

4. Dreyer, D. R.; Park, S.; Bielawski, C. W.; Ruoff, R. S., The Chemistry of Graphene Oxide. *Chem. Soc. Rev.* **2010**, *39*, 228-240.

5. He, H.; Riedl, T.; Lerf, A.; Klinowski, J., Solid-State Nmr Studies of the Structure of Graphite Oxide. *The Journal of physical chemistry* **1996**, *100*, 19954-19958.

6. Joshi, R.; Alwarappan, S.; Yoshimura, M.; Sahajwalla, V.; Nishina, Y., Graphene Oxide: The New Membrane Material. *Applied Materials Today* **2015**, *1*, 1-12.

7. Nicolaï, A.; Sumpter, B. G.; Meunier, V., Tunable Water Desalination across Graphene Oxide Framework Membranes. *Physical Chemistry Chemical Physics* **2014**, *16*, 8646-8654.

8. Bayer, T.; Bishop, S.; Nishihara, M.; Sasaki, K.; Lyth, S., Characterization of a Graphene Oxide Membrane Fuel Cell. *Journal of Power Sources* **2014**, *272*, 239-247.

9. Gao, W.; Wu, G.; Janicke, M. T.; Cullen, D. A.; Mukundan, R.; Baldwin, J. K.; Brosha, E. L.; Galande, C.; Ajayan, P. M.; More, K. L., Ozonated Graphene Oxide Film as a Proton - Exchange Membrane. *Angewandte Chemie International Edition* **2014**, *53*, 3588-3593.

10. Musico, Y. L. F.; Santos, C. M.; Dalida, M. L. P.; Rodrigues, D. F., Surface Modification of Membrane Filters Using Graphene and Graphene Oxide-Based Nanomaterials for Bacterial Inactivation and Removal. *ACS Sustainable Chemistry & Engineering* **2014**, *2*, 1559-1565.

11. Chen, D.; Feng, H.; Li, J., Graphene Oxide: Preparation, Functionalization, and Electrochemical Applications. *Chemical reviews* **2012**, *112*, 6027-6053.

12. Kim, S.; Zhou, S.; Hu, Y.; Acik, M.; Chabal, Y. J.; Berger, C.; De Heer, W.; Bongiorno, A.; Riedo, E., Room-Temperature Metastability of Multilayer Graphene Oxide Films. *Nat. Mater.* **2012**, *11*, 544-549.

13. Shaffault, P. J., *Prakt. Chem.* **1841**, *21*, 155.

14. Brodie, B. C., On the Atomic Weight of Graphite. *Philosophical Transactions of the Royal Society of London* **1859**, *149*, 249-259.

15. Staudenmaier, L., Method for the Preparation of Graphitic Acid. *Ber Dtsch Chem Ges* **1898**, *31*, 1481-1487.

16. Marcano, D. C.; Kosynkin, D. V.; Berlin, J. M.; Sinitskii, A.; Sun, Z.; Slesarev, A.; Alemany, L. B.; Lu, W.; Tour, J. M., Improved Synthesis of Graphene Oxide. *ACS nano* **2010**, *4*, 4806-4814.

17. Hummers Jr, W. S.; Offeman, R. E., Preparation of Graphitic Oxide. *Journal of the american chemical society* **1958**, *80*, 1339-1339.

18. Hatakeyama, K.; Hakuta, Y.; Sugiyama, J.-i.; Shimizu, Y., A Simple Ozone Bubbling Procedure for the Preparation of Graphene Oxide. *Japanese Journal of Applied Physics* **2019**, *58*, SIIA05.

19. Liu, F.; Wang, C.; Sui, X.; Riaz, M. A.; Xu, M.; Wei, L.; Chen, Y., Synthesis of Graphene Materials by Electrochemical Exfoliation: Recent Progress and Future Potential. *Carbon Energy* **2019**, *1*, 173-199.

20. Zhang, G.; Wen, M.; Wang, S.; Chen, J.; Wang, J., Insights into Electrochemical Behavior and Anodic Oxidation Processing of Graphite Matrix in Aqueous Solutions of Sodium Nitrate. *J. Appl. Electrochem.* **2016**, *46*, 1163-1176.

21. Munuera, J.; Paredes, J.; Villar-Rodil, S.; Martínez-Alonso, A.; Tascón, J., A Simple Strategy to Improve the Yield of Graphene Nanosheets in the Anodic Exfoliation of Graphite Foil. *Carbon* **2017**, *115*, 625-628.

22. Cao, J.; He, P.; Mohammed, M. A.; Zhao, X.; Young, R. J.; Derby, B.; Kinloch, I. A.; Dryfe, R. A., Two-Step Electrochemical Intercalation and Oxidation of Graphite for the Mass Production of Graphene Oxide. *J. Am. Chem. Soc.* **2017**, *139*, 17446-17456.

23. Pei, S.; Wei, Q.; Huang, K.; Cheng, H.-M.; Ren, W., Green Synthesis of Graphene Oxide by Seconds Timescale Water Electrolytic Oxidation. *Nature communications* **2018**, *9*, 1-9.

24. Sahoo, S. K.; Ratha, S.; Rout, C. S.; Mallik, A., Physicochemical Properties and Supercapacitor Behavior of Electrochemically Synthesized Few Layered Graphene Nanosheets. *J. Solid State Electrochem.* **2016**, *20*, 3415-3428.

25. Li, C.; Xu, Y.-T.; Zhao, B.; Jiang, L.; Chen, S.-G.; Xu, J.-B.; Fu, X.-Z.; Sun, R.; Wong, C.-P., Flexible Graphene Electrothermal Films Made from Electrochemically Exfoliated Graphite. *J. Mater. Sci.* **2016**, *51*, 1043-1051.

26. Hamra, A.; Lim, H.; Chee, W.; Huang, N., Electro-Exfoliating Graphene from Graphite for Direct Fabrication of Supercapacitor. *Appl. Surf. Sci.* **2016**, *360*, 213-223.

27. Tian, S.; Yang, S.; Huang, T.; Sun, J.; Wang, H.; Pu, X.; Tian, L.; He, P.; Ding, G.; Xie, X., One-Step Fast Electrochemical Fabrication of Water-Dispersible Graphene. *Carbon* **2017**, *111*, 617-621.

28. Li, X.; Zhao, Z.; Pan, C., Electrochemical Exfoliation of Carbon Dots with the Narrowest Full Width at Half Maximum in Their Fluorescence Spectra in the Ultraviolet Region Using Only Water as Electrolyte. *Chem. Commun. (Cambridge, U. K.)* **2016**, *52*, 9406-9409.

29. Muthurasu, A.; Dhandapani, P.; Ganesh, V., Facile and Simultaneous Synthesis of Graphene Quantum Dots and Reduced Graphene Oxide for Bio-Imaging and Supercapacitor Applications. *New Journal of Chemistry* **2016**, *40*, 9111-9124.

30. Hossain, S. T.; Wang, R., Electrochemical Exfoliation of Graphite: Effect of Temperature and Hydrogen Peroxide Addition. *Electrochim. Acta* **2016**, *216*, 253-260.

31. Hsieh, C.-T.; Hsueh, J.-H., Electrochemical Exfoliation of Graphene Sheets from a Natural Graphite Flask in the Presence of Sulfate Ions at Different Temperatures. *Rsc Advances* **2016**, *6*, 64826-64831.

32. Yu, P.; Tian, Z.; Lowe, S. E.; Song, J.; Ma, Z.; Wang, X.; Han, Z. J.; Bao, Q.; Simon, G. P.; Li, D., Mechanically-Assisted Electrochemical Production of Graphene Oxide. *Chem. Mater.* **2016**, *28*, 8429-8438.

33. Han, T. H.; Huang, Y.-K.; Tan, A. T.; Dravid, V. P.; Huang, J., Steam Etched Porous Graphene Oxide Network for Chemical Sensing. *Journal of the American Chemical Society* **2011**, *133*, 15264-15267.

34. Koinuma, M.; Ogata, C.; Kamei, Y.; Hatakeyama, K.; Tateishi, H.; Watanabe, Y.; Taniguchi, T.; Gezuhara, K.; Hayami, S.; Funatsu, A., Photochemical Engineering of Graphene Oxide Nanosheets. *The Journal of Physical Chemistry C* **2012**, *116*, 19822-19827.

35. Eftekhari, A.; Shulga, Y. M.; Baskakov, S. A.; Gutsev, G. L., Graphene Oxide Membranes for Electrochemical Energy Storage and Conversion. *Int. J. Hydrogen Energy* **2018**, *43*, 2307-2326.

36. Gómez-Navarro, C.; Weitz, R. T.; Bittner, A. M.; Scolari, M.; Mews, A.; Burghard, M.; Kern, K., Electronic Transport Properties of Individual Chemically Reduced Graphene Oxide Sheets. *Nano Lett.* **2007**, *7*, 3499-3503.

37. Eda, G.; Chhowalla, M., Chemically Derived Graphene Oxide: Towards Large - Area Thin - Film Electronics and Optoelectronics. *Adv. Mater. (Weinheim, Ger.)* **2010**, *22*, 2392-2415.

38. Loh, K. P.; Bao, Q.; Eda, G.; Chhowalla, M., Graphene Oxide as a Chemically Tunable Platform for Optical Applications. *Nature Chem.* **2010**, *2*, 1015.

39. Bayer, T.; Selyanchyn, R.; Fujikawa, S.; Sasaki, K.; Lyth, S., Spray-Painted Graphene Oxide Membrane Fuel Cells. *Journal of Membrane Science* **2017**, *541*, 347-357.

40. Thimmappa, R.; Fawaz, M.; Devendrachari, M. C.; Gautam, M.; Kottaichamy, A. R.; Shafi, S. P.; Thotiyl, M. O., Anisotropic Amplification of Proton Transport in Proton Exchange Membrane Fuel Cells. *Chemical Physics Letters* **2017**, *679*, 1-5.

41. Kumar, R.; Mamlouk, M.; Scott, K., A Graphite Oxide Paper Polymer Electrolyte for Direct Methanol Fuel Cells. *International Journal of Electrochemistry* **2011**, *2011*.

42. Thimmappa, R.; Devendrachari, M. C.; Kottaichamy, A. R.; Tiwari, O.; Gaikwad, P.; Paswan, B.; Thotiyl, M. O., Stereochemistry-Dependent Proton Conduction in Proton Exchange Membrane Fuel Cells. *Langmuir* **2016**, *32*, 359-365.

43. Gautama, M.; Devendracharia, M. C.; Thimmappa, R.; Kottaichamya, A. R.; Shafia, S. P.; Gaikwada, P.; Makri Nimbegondi Kotreshb, H.; Thotiyla, M. O., Polarity Governed Selective Amplification of through Plane Proton Shuttling in Proton Exchange Membrane Fuel Cell. **2017**.

44. Karim, M. R.; Hatakeyama, K.; Matsui, T.; Takehira, H.; Taniguchi, T.; Koinuma, M.; Matsumoto, Y.; Akutagawa, T.; Nakamura, T.; Noro, S.-i., Graphene Oxide Nanosheet with High Proton Conductivity. *Journal of the American Chemical Society* **2013**, *135*, 8097-8100.

45. Hatakeyama, K.; Karim, M. R.; Ogata, C.; Tateishi, H.; Funatsu, A.; Taniguchi, T.; Koinuma, M.; Hayami, S.; Matsumoto, Y., Proton Conductivities of Graphene Oxide Nanosheets: Single, Multilayer, and Modified Nanosheets. *Angewandte Chemie* **2014**, *126*, 7117-7120.

46. Smirnov, V.; Denisov, N.; Dremova, N.; Vol'fkovich, Y.; Rychagov, A.; Sosenkin, V.; Belay, K.; Gutsev, G.; Shulga, N. Y.; Shulga, Y. M., A Comparative Analysis of Graphene Oxide Films as Proton Conductors. *Applied Physics A* **2014**, *117*, 1859-1863.

47. Nair, R.; Wu, H.; Jayaram, P.; Grigorieva, I.; Geim, A., Unimpeded Permeation of Water through Helium-Leak–Tight Graphene-Based Membranes. *Science* **2012**, *335*, 442-444.

48. Paneri, A.; Heo, Y.; Ehlert, G.; Cottrill, A.; Sodano, H.; Pintauro, P.; Moghaddam, S., Proton Selective Ionic Graphene-Based Membrane for High Concentration Direct Methanol Fuel Cells. *J. Membr. Sci.* **2014**, *467*, 217-225.

49. Lv, W.; You, C.-H.; Wu, S.; Li, B.; Zhu, Z.-P.; Wang, M.; Yang, Q.-H.; Kang, F., Ph-Mediated Fine-Tuning of Optical Properties of Graphene Oxide Membranes. *Carbon* **2012**, *50*, 3233-3239.

50. Krueger, M.; Berg, S.; Stone, D. A.; Strelcov, E.; Dikin, D. A.; Kim, J.; Cote, L. J.; Huang, J.; Kolmakov, A., Drop-Casted Self-Assembling Graphene Oxide Membranes for Scanning Electron Microscopy on Wet and Dense Gaseous Samples. *ACS Nano* **2011**, *5*, 10047-10054.

51. Hu, M.; Mi, B., Enabling Graphene Oxide Nanosheets as Water Separation Membranes. *Environ. Sci. Technol.* **2013**, *47*, 3715-3723.

52. Dikin, D. A.; Stankovich, S.; Zimney, E. J.; Piner, R. D.; Dommett, G. H.; Evmenenko, G.; Nguyen, S. T.; Ruoff, R. S., Preparation and Characterization of Graphene Oxide Paper. *Nature* **2007**, *448*, 457.

53. Tsou, C.-H.; An, Q.-F.; Lo, S.-C.; De Guzman, M.; Hung, W.-S.; Hu, C.-C.; Lee, K.-R.; Lai, J.-Y., Effect of Microstructure of Graphene Oxide Fabricated through Different Self-Assembly Techniques on 1-Butanol Dehydration. *J. Membr. Sci.* **2015**, *477*, 93-100.

54. Akbari, A.; Sheath, P.; Martin, S. T.; Shinde, D. B.; Shaibani, M.; Banerjee, P. C.; Tkacz, R.; Bhattacharyya, D.; Majumder, M., Large-Area Graphene-Based Nanofiltration Membranes by Shear Alignment of Discotic Nematic Liquid Crystals of Graphene Oxide. *Nature communications* **2016**, *7*, 1-12.

55. Shen, J.; Han, K.; Martin, E. J.; Wu, Y. Y.; Kung, M. C.; Hayner, C. M.; Shull, K. R.; Kung, H. H., Upper-Critical Solution Temperature (Ucst) Polymer Functionalized Graphene Oxide as Thermally Responsive Ion Permeable Membrane for Energy Storage Devices. *J. Mat. Chem. A* **2014**, *2*, 18204-18207.

56. Zarrin, H.; Sy, S.; Fu, J.; Jiang, G.; Kang, K.; Jun, Y.-S.; Yu, A.; Fowler, M.; Chen, Z., Molecular Functionalization of Graphene Oxide for Next-Generation Wearable Electronics. *ACS Applied Materials & Interfaces* **2016**, *8*, 25428-25437.

57. Pandey, R. P.; Shukla, G.; Manohar, M.; Shahi, V. K., Graphene Oxide Based Nanohybrid Proton Exchange Membranes for Fuel Cell Applications: An Overview. *Adv. Colloid Interface Sci.* **2017**, *240*, 15-30.

58. Ansari, S.; Kelarakis, A.; Estevez, L.; Giannelis, E. P., Oriented Arrays of Graphene in a Polymer Matrix by in Situ Reduction of Graphite Oxide Nanosheets. *Small* **2010**, *6*, 205-209.

59. Zarrin, H.; Higgins, D.; Jun, Y.; Chen, Z.; Fowler, M., Functionalized Graphene Oxide Nanocomposite Membrane for Low Humidity and High Temperature Proton Exchange Membrane Fuel Cells. *The Journal of Physical Chemistry C* **2011**, *115*, 20774-20781.

60. Xing, P.; Robertson, G. P.; Guiver, M. D.; Mikhailenko, S. D.; Wang, K.; Kaliaguine, S., Synthesis and Characterization of Sulfonated Poly (Ether Ether Ketone) for Proton Exchange Membranes. *J. Membr. Sci.* **2004**, *229*, 95-106.

61. Kumar, R.; Mamlouk, M.; Scott, K., Sulfonated Polyether Ether Ketone–Sulfonated Graphene Oxide Composite Membranes for Polymer Electrolyte Fuel Cells. *RSC Advances* **2014**, *4*, 617-623.

62. Zhu, J.; Chen, C.; Lu, Y.; Zang, J.; Jiang, M.; Kim, D.; Zhang, X., Highly Porous Polyacrylonitrile/Graphene Oxide Membrane Separator Exhibiting Excellent Anti-Self-Discharge Feature for High-Performance Lithium–Sulfur Batteries. *Carbon* **2016**, *101*, 272-280.

63. Zheng, Y.; Zheng, S.; Xue, H.; Pang, H., Metal - Organic Frameworks/Graphene - Based Materials: Preparations and Applications. *Adv. Funct. Mater.* **2018**, *28*, 1804950.

64. Bakangura, E.; Wu, L.; Ge, L.; Yang, Z.; Xu, T., Mixed Matrix Proton Exchange Membranes for Fuel Cells: State of the Art and Perspectives. *Prog. Polym. Sci.* **2016**, *57*, 103-152.

65. Zhu, Q.-L.; Xu, Q., Metal–Organic Framework Composites. *Chem. Soc. Rev.* **2014**, *43*, 5468-5512.

66. Salunkhe, R. R.; Kaneti, Y. V.; Kim, J.; Kim, J. H.; Yamauchi, Y., Nanoarchitectures for Metal–Organic Framework-Derived Nanoporous Carbons toward Supercapacitor Applications. *Acc. Chem. Res.* **2016**, *49*, 2796-2806.

67. Wang, F.; Wu, X.; Yuan, X.; Liu, Z.; Zhang, Y.; Fu, L.; Zhu, Y.; Zhou, Q.; Wu, Y.; Huang, W., Latest Advances in Supercapacitors: From New Electrode Materials to Novel Device Designs. *Chem. Soc. Rev.* **2017**, *46*, 6816-6854.

68. Bian, Z.; Xu, J.; Zhang, S.; Zhu, X.; Liu, H.; Hu, J., Interfacial Growth of Metal Organic Framework/Graphite Oxide Composites through Pickering Emulsion and Their Co2 Capture Performance in the Presence of Humidity. *Langmuir* **2015**, *31*, 7410-7417.

69. Pang, H.; Li, X.; Zhao, Q.; Xue, H.; Lai, W.-Y.; Hu, Z.; Huang, W., One-Pot Synthesis of Heterogeneous Co3o4-Nanocube/Co (Oh) 2-Nanosheet Hybrids for High-Performance Flexible Asymmetric All-Solid-State Supercapacitors. *Nano Energy* **2017**, *35*, 138-145.

70. Castarlenas, S.; Téllez, C.; Coronas, J., Gas Separation with Mixed Matrix Membranes Obtained from Mof Uio-66-Graphite Oxide Hybrids. *J. Membr. Sci.* **2017**, *526*, 205-211.

71. Lin, B.; Shang, H.; Chu, F.; Ren, Y.; Yuan, N.; Jia, B.; Zhang, S.; Yu, X.; Wei, Y.; Ding, J., Ionic Liquid-Tethered Graphene Oxide/Ionic Liquid Electrolytes for Highly Efficient Dye Sensitized Solar Cells. *Electrochim. Acta* **2014**, *134*, 209-214.

72. Wang, C.; Lin, B.; Qiao, G.; Wang, L.; Zhu, L.; Chu, F.; Feng, T.; Yuan, N.; Ding, J., Polybenzimidazole/Ionic Liquid Functionalized Graphene Oxide Nanocomposite Membrane for Alkaline Anion Exchange Membrane Fuel Cells. *Mater. Lett.* **2016**, *173*, 219-222.

73. Chu, F.; Lin, B.; Feng, T.; Wang, C.; Zhang, S.; Yuan, N.; Liu, Z.; Ding, J., Zwitterion-Coated Graphene-Oxide-Doped Composite Membranes for Proton Exchange Membrane Applications. *J. Membr. Sci.* **2015**, *496*, 31-38.

74. Smitha, B.; Sridhar, S.; Khan, A., Solid Polymer Electrolyte Membranes for Fuel Cell Applications—a Review. *Journal of membrane science* **2005**, *259*, 10-26.

75. Miyamoto, A.; Kuwaki, Y.; Sano, T.; Hatakeyama, K.; Quitain, A.; Sasaki, M.; Kida, T., Solid Electrolyte Gas Sensor Based on a Proton-Conducting Graphene Oxide Membrane. *ACS omega* **2017**, *2*, 2994-3001.

76. Energy, U. S. D. o. Fuel Cells. https://energy.gov/eere/fuelcells (accessed 2017.03.10).

77. Becker, H. I. Low Voltage Electrolytic Capacitor. 1957.

78. International, S., Mazda Introduces Supercapacitor-Type Regenerative Braking. *Automotive Engineering magazine* 2013.

79. Technologies, M. Ultracapacitor Overview. (accessed 2017.03.10).

80. Robinett, M. I.; Snyder, D. Rechargeable Portable Light with Multiple Charging Systems. 2003.

81. Ridden, P. Helium Bluetooth Speakers Powered by Supercapacitors. http://www.gizmag.com/helium-capacitor-powered-speakers/29938/ (accessed July 20).

82. Zhang, L. L.; Zhou, R.; Zhao, X., Graphene-Based Materials as Supercapacitor Electrodes. *Journal of Materials Chemistry* **2010**, *20*, 5983-5992.

83. Kang, J.; Wen, J.; Jayaram, S. H.; Yu, A.; Wang, X., Development of an Equivalent Circuit Model for Electrochemical Double Layer Capacitors (Edlcs) with Distinct Electrolytes. *Electrochimica Acta* **2014**, *115*, 587-598.

84. Zhong, C.; Deng, Y.; Hu, W.; Qiao, J.; Zhang, L.; Zhang, J., A Review of Electrolyte Materials and Compositions for Electrochemical Supercapacitors. *Chemical Society Reviews* **2015**.

85. Marin S. Halper, J. C. E. *Supercapacitors: A Brief Overview*; MITRE Nanosystems Group: McLean, Virginia, US, march 2006, 2006; p 41.

86. Conway, B. E., *Electrochemical Supercapacitors: Scientific Fundamentals and Technological Applications*. Springer Science & Business Media: 2013.

87. Goldstein, J.; Brown, I.; Koretz, B., New Developments in the Electric Fuel Ltd. Zinc/Air System. *J. Power Sources* **1999**, *80*, 171-179.

88. Cheiky, M. C.; Danczyk, L. G.; Scheffler, R. L. *Zinc-Air Powered Electric Vehicle Systems Integration Issues*; 0148-7191; SAE Technical Paper: 1991.

89. Wang, Y.-J.; Fang, B.; Zhang, D.; Li, A.; Wilkinson, D. P.; Ignaszak, A.; Zhang, L.; Zhang, J., A Review of Carbon-Composited Materials as Air-Electrode Bifunctional Electrocatalysts for Metal–Air Batteries. *Electrochemical Energy Reviews* **2018**, *1*, 1-34.

90. Defant, J. C.; Hamerly, M. E.; Segal, D. S.; Cohen, S., Wrist Worn Mobile Alcohol and Offender Monitoring System. Google Patents: 2018.

91. Ozoemena, K. I., Nanostructured Platinum-Free Electrocatalysts in Alkaline Direct Alcohol Fuel Cells: Catalyst Design, Principles and Applications. *RSC advances* **2016**, *6*, 89523-89550.

92. Ozoemena, K. I.; Musa, S.; Modise, R.; Ipadeola, A. K.; Gaolatlhe, L.; Peteni, S.; Kabongo, G., Fuel Cell-Based Breath-Alcohol Sensors: Innovation-Hungry Old Electrochemistry. *Current Opinion in Electrochemistry* **2018**, *10*, 82-87.

93. Zhou, W.; Wang, Z. L., *Scanning Microscopy for Nanotechnology: Techniques and Applications*. Springer science & business media: 2007.

94. Reimer, L., *Transmission Electron Microscopy: Physics of Image Formation and Microanalysis*. Springer: 2013; Vol. 36.

95. Spence, J. C., *High-Resolution Electron Microscopy*. OUP Oxford: 2013.

96. Connolly, J. R., Introduction to X-Ray Powder Diffraction. *Material in this document is* **2007**.

97. Langford, J. I.; Wilson, A., Scherrer after Sixty Years: A Survey and Some New Results in the Determination of Crystallite Size. *Journal of applied crystallography* **1978**, *11*, 102-113.

98. Hassan, F. M.; Chabot, V.; Li, J.; Kim, B. K.; Ricardez-Sandoval, L.; Yu, A., Pyrrolic-Structure Enriched Nitrogen Doped Graphene for Highly Efficient Next Generation Supercapacitors. *Journal of Materials Chemistry A* **2013**, *1*, 2904-2912.

99. Mallet-Ladeira, P.; Puech, P.; Toulouse, C.; Cazayous, M.; Ratel-Ramond, N.; Weisbecker, P.; Vignoles, G. L.; Monthioux, M., A Raman Study to Obtain Crystallite Size of Carbon Materials: A Better Alternative to the Tuinstra–Koenig Law. *Carbon* **2014**, *80*, 629-639.

100. Tuinstra, F.; Koenig, J. L., Raman Spectrum of Graphite. *The Journal of Chemical Physics* **1970**, *53*, 1126-1130.

101. Amadei, C. A.; Stein, I. Y.; Silverberg, G. J.; Wardle, B. L.; Vecitis, C. D., Fabrication and Morphology Tuning of Graphene Oxide Nanoscrolls. *Nanoscale* **2016**, *8*, 6783-6791.

102. Ferrari, A. C.; Robertson, J., Interpretation of Raman Spectra of Disordered and Amorphous Carbon. *Physical review B* **2000**, *61*, 14095.

103. Goldstein, J. I.; Newbury, D. E., Scanning Electron Microscopy and X-Ray Microanalysis. **2003**.

104. Hofmann, S., *Auger-and X-Ray Photoelectron Spectroscopy in Materials Science: A User-Oriented Guide*. Springer Science & Business Media: 2012; Vol. 49.

105. Griffiths, P. R.; De Haseth, J. A., *Fourier Transform Infrared Spectrometry*. John Wiley & Sons: 2007; Vol. 171.

106. Danks, T. N.; Slade, R. C.; Varcoe, J. R., Alkaline Anion-Exchange Radiation-Grafted Membranes for Possible Electrochemical Application in Fuel Cells. *Journal of Materials Chemistry* **2003**, *13*, 712-721.

107. Ltd, S. M. S. Dynamic Vapor Sorption (Dvs). https://www.surfacemeasurementsystems.com/solutions/dynamic_vapor_sorption/.

108. Park, G.; Membranes, I. S., Science, Engineering and Applications; Bungay, Pm; Lonsdale, Hk; De Pinho, Mn, Eds. Reidel: Dordrecht: 1986.

109. Bungay, J. K., *Synthetic Membranes:: Science, Engineering and Applications*. Springer Science & Business Media: 2012; Vol. 181.

110. Instruments, G. *Basics of Electrochemical Impdeance Spectroscopy*; Gamry Instruments: 734 Louis Drive, Warminister, PA, USA, 2010; p 17.

111. Knauth, P.; Pasquini, L.; Maranesi, B.; Pelzer, K.; Polini, R.; Di Vona, M., Proton Mobility in Sulfonated Polyetheretherketone (Speek): Influence of Thermal Crosslinking and Annealing. *Fuel Cells* **2013**, *13*, 79-85.

112. Simon, P.; Gogotsi, Y.; Dunn, B., Where Do Batteries End and Supercapacitors Begin? *Science* **2014**, *343*, 1210-1211.

113. Zhang, S.; Pan, N., Supercapacitors Performance Evaluation. *Advanced Energy Materials* **2015**, *5*, 1401401.

114. Cai, X.; Peng, M.; Yu, X.; Fu, Y.; Zou, D., Flexible Planar/Fiber-Architectured Supercapacitors for Wearable Energy Storage. *Journal of Materials Chemistry C* **2014**, *2*, 1184-1200.

115. Choi, K. H.; Cho, S. J.; Kim, S. H.; Kwon, Y. H.; Kim, J. Y.; Lee, S. Y., Thin, Deformable, and Safety - Reinforced Plastic Crystal Polymer Electrolytes for High - Performance Flexible Lithium - Ion Batteries. *Advanced Functional Materials* **2014**, *24*, 44-52.

116. Vlad, A.; Singh, N.; Galande, C.; Ajayan, P. M., Design Considerations for Unconventional Electrochemical Energy Storage Architectures. *Advanced Energy Materials* **2015**, *5*, 1402115.

117. Park, J.; Park, M.; Nam, G.; Lee, J. s.; Cho, J., All - Solid - State Cable - Type Flexible Zinc–Air Battery. *Advanced Materials* **2015**, *27*, 1396-1401.

118. Kim, B. C.; Hong, J. Y.; Wallace, G. G.; Park, H. S., Recent Progress in Flexible Electrochemical Capacitors: Electrode Materials, Device Configuration, and Functions. *Advanced Energy Materials* **2015**, *5*, 1500959.

119. Lee, J. S.; Tai Kim, S.; Cao, R.; Choi, N. S.; Liu, M.; Lee, K. T.; Cho, J., Metal–Air Batteries with High Energy Density: Li–Air Versus Zn–Air. *Advanced Energy Materials* **2011**, *1*, 34-50.

120. Gu, S.; Wang, J.; Zhang, B.; Kaspar, R. B.; Yan, Y., Hydroxide Exchange Membranes and Ionomers. *Edited by Bradley Ladewig, San P. Jiang, and Yushan Yan* **2015**.

121. Kim, D. S.; Labouriau, A.; Guiver, M. D.; Kim, Y. S., Guanidinium-Functionalized Anion Exchange Polymer Electrolytes Via Activated Fluorophenyl-Amine Reaction. *Chemistry of Materials* **2011**, *23*, 3795-3797.

122. Yu, G.; Hu, L.; Vosgueritchian, M.; Wang, H.; Xie, X.; McDonough, J. R.; Cui, X.; Cui, Y.; Bao, Z., Solution-Processed Graphene/Mno2 Nanostructured Textiles for High-Performance Electrochemical Capacitors. *Nano letters* **2011**, *11*, 2905-2911.

123. Zarrin, H.; Fu, J.; Jiang, G.; Yoo, S.; Lenos, J.; Fowler, M.; Chen, Z., Quaternized Graphene Oxide Nanocomposites as Fast Hydroxide Conductors. *ACS nano* **2015**, *9*, 2028-2037.

124. Yang, X.; Zhang, F.; Zhang, L.; Zhang, T.; Huang, Y.; Chen, Y., A High - Performance Graphene Oxide - Doped Ion Gel as Gel Polymer Electrolyte for All - Solid - State Supercapacitor Applications. *Advanced Functional Materials* **2013**, *23*, 3353-3360.

125. Scott, K., Freestanding Sulfonated Graphene Oxide Paper: A New Polymer Electrolyte for Polymer Electrolyte Fuel Cells. *Chemical Communications* **2012**, *48*, 5584-5586.

126. Hatakeyama, K.; Karim, M. R.; Ogata, C.; Tateishi, H.; Funatsu, A.; Taniguchi, T.; Koinuma, M.; Hayami, S.; Matsumoto, Y., Proton Conductivities of Graphene Oxide Nanosheets: Single, Multilayer, and Modified Nanosheets. *Angewandte Chemie International Edition* **2014**, *53*, 6997-7000.

127. Yuan, M.; Erdman, J.; Tang, C.; Ardebili, H., High Performance Solid Polymer Electrolyte with Graphene Oxide Nanosheets. *Rsc Advances* **2014**, *4*, 59637-59642.

128. Varcoe, J. R., Investigations of the Ex Situ Ionic Conductivities at 30 C of Metal-Cation-Free Quaternary Ammonium Alkaline Anion-Exchange Membranes in Static Atmospheres of Different Relative Humidities. *Physical Chemistry Chemical Physics* **2007**, *9*, 1479-1486.

129. Ghandi, K., A Review of Ionic Liquids, Their Limits and Applications. *Green and sustainable chemistry* **2014**, *4*, 44.

130. Armand, M.; Endres, F.; MacFarlane, D. R.; Ohno, H.; Scrosati, B., Ionic-Liquid Materials for the Electrochemical Challenges of the Future. In *Materials for Sustainable Energy: A Collection of Peer-Reviewed Research and Review Articles from Nature Publishing Group;* World Scientific: 2011; pp 129-137.

131. William, S.; Hummers, J.; Offeman, R. E., Preparation of Graphitic Oxide. *J. Am. Chem. Soc* **1958**, *80*, 1339-1339.

132. Cançado, L.; Takai, K.; Enoki, T.; Endo, M.; Kim, Y.; Mizusaki, H.; Jorio, A.; Coelho, L.; Magalhaes-Paniago, R.; Pimenta, M., General Equation for the Determination of the Crystallite Size L a of Nanographite by Raman Spectroscopy. *Applied Physics Letters* **2006**, *88*, 163106.

133. Huh, S. H., Thermal Reduction of Graphene Oxide. *Physics and Applications of Graphene-Experiments* **2011**, 73-90.

134. Xue, Y.; Liu, Y.; Lu, F.; Qu, J.; Chen, H.; Dai, L., Functionalization of Graphene Oxide with Polyhedral Oligomeric Silsesquioxane (Poss) for Multifunctional Applications. *The journal of physical chemistry letters* **2012**, *3*, 1607-1612.

135. He, H.; Gao, C., General Approach to Individually Dispersed, Highly Soluble, and Conductive Graphene Nanosheets Functionalized by Nitrene Chemistry. *Chemistry of Materials* **2010**, *22*, 5054-5064.

136. Niyogi, S.; Bekyarova, E.; Itkis, M. E.; Zhang, H.; Shepperd, K.; Hicks, J.; Sprinkle, M.; Berger, C.; Lau, C. N.; Deheer, W. A., Spectroscopy of Covalently Functionalized Graphene. *Nano letters* **2010**, *10*, 4061-4066.

137. Wang, D.; Li, Y.; Hasin, P.; Wu, Y., Preparation, Characterization, and Electrocatalytic Performance of Graphene-Methylene Blue Thin Films. *Nano Research* **2011**, *4*, 124-130.

138. Ferrari, A. C.; Basko, D. M., Raman Spectroscopy as a Versatile Tool for Studying the Properties of Graphene. *Nature nanotechnology* **2013**, *8*, 235.

139. Haubner, K.; Murawski, J.; Olk, P.; Eng, L. M.; Ziegler, C.; Adolphi, B.; Jaehne, E., The Route to Functional Graphene Oxide. *ChemPhysChem* **2010**, *11*, 2131-2139.

140. Yan, W.; Huang, Y.; Xu, Y.; Huang, L.; Chen, Y., Rapid and Effective Functionalization of Graphene Oxide by Ionic Liquid. *Journal of nanoscience and nanotechnology* **2012**, *12*, 2270-2277.

141. Seethalakshmi, K.; Rani, E. J. V.; Padmavathy, R.; Radha, N., Ft-Ir Spectral Analysis of Imidazolium Chloride. *Int. J. Cur. Res. Rev* **2012**, *4*, 31-36.

142. Guo, M.; Fang, J.; Xu, H.; Li, W.; Lu, X.; Lan, C.; Li, K., Synthesis and Characterization of Novel Anion Exchange Membranes Based on Imidazolium-Type Ionic Liquid for Alkaline Fuel Cells. *Journal of Membrane Science* **2010**, *362*, 97-104.

143. Compton, O. C.; Dikin, D. A.; Putz, K. W.; Brinson, L. C.; Nguyen, S. T., Electrically Conductive "Alkylated" Graphene Paper Via Chemical Reduction of Amine - Functionalized Graphene Oxide Paper. *Advanced materials* **2010**, *22*, 892-896.

144. Geng, D.; Yang, S.; Zhang, Y.; Yang, J.; Liu, J.; Li, R.; Sham, T.-K.; Sun, X.; Ye, S.; Knights, S., Nitrogen Doping Effects on the Structure of Graphene. *Applied Surface Science* **2011**, *257*, 9193-9198.

145. Chetsanga, C. J.; Makaroff, C., Alkaline Opening of Imidazole Ring of 7-Methylguanosine. 2. Further Studies on Reaction Mechanisms and Products. *Chemico-biological interactions* **1982**, *41*, 235-249.

146. Yang, H.; Shan, C.; Li, F.; Han, D.; Zhang, Q.; Niu, L., Covalent Functionalization of Polydisperse Chemically-Converted Graphene Sheets with Amine-Terminated Ionic Liquid. *Chemical Communications* **2009**, 3880-3882.

147. Park, S.; An, J.; Piner, R. D.; Jung, I.; Yang, D.; Velamakanni, A.; Nguyen, S. T.; Ruoff, R. S., Aqueous Suspension and Characterization of Chemically Modified Graphene Sheets. *Chemistry of materials* **2008**, *20*, 6592-6594.

148. Georgakilas, V.; Otyepka, M.; Bourlinos, A. B.; Chandra, V.; Kim, N.; Kemp, K. C.; Hobza, P.; Zboril, R.; Kim, K. S., Functionalization of Graphene: Covalent and Non-Covalent Approaches, Derivatives and Applications. *Chemical reviews* **2012**, *112*, 6156-6214.

149. Bayer, T.; Bishop, S. R.; Perry, N. H.; Sasaki, K.; Lyth, S. M., Tunable Mixed Ionic/Electronic Conductivity and Permittivity of Graphene Oxide Paper for Electrochemical Energy Conversion. *ACS applied materials & interfaces* **2016**, *8*, 11466-11475.

150. Wang, J. T.-W.; Hsu, S. L.-C., Enhanced High-Temperature Polymer Electrolyte Membrane for Fuel Cells Based on Polybenzimidazole and Ionic Liquids. *Electrochimica Acta* **2011**, *56*, 2842-2846.

151. Xie, Z.-L.; Jeličić, A.; Wang, F.-P.; Rabu, P.; Friedrich, A.; Beuermann, S.; Taubert, A., Transparent, Flexible, and Paramagnetic Ionogels Based on Pmma and the Iron-Based Ionic Liquid 1-Butyl-3-Methylimidazolium Tetrachloroferrate (Iii)[Bmim][Fecl4]. *Journal of Materials Chemistry* **2010**, *20*, 9543-9549.

152. Kudo, S.; Zhou, Z.; Yamasaki, K.; Norinaga, K.; Hayashi, J.-i., Sulfonate Ionic Liquid as a Stable and Active Catalyst for Levoglucosenone Production from Saccharides Via Catalytic Pyrolysis. *Catalysts* **2013**, *3*, 757-773.

153. Wang, Y.-J.; Qiao, J.; Baker, R.; Zhang, J., Alkaline Polymer Electrolyte Membranes for Fuel Cell Applications. *Chemical Society Reviews* **2013**, *42*, 5768-5787.

154. Bi, H.; Yin, K.; Xie, X.; Ji, J.; Wan, S.; Sun, L.; Terrones, M.; Dresselhaus, M. S., Ultrahigh Humidity Sensitivity of Graphene Oxide. *Scientific reports* **2013**, *3*, 2714.

155. Buchsteiner, A.; Lerf, A.; Pieper, J., Water Dynamics in Graphite Oxide Investigated with Neutron Scattering. *The Journal of Physical Chemistry B* **2006**, *110*, 22328-22338.

156. Fu, J.; Zhang, J.; Song, X.; Zarrin, H.; Tian, X.; Qiao, J.; Rasen, L.; Li, K.; Chen, Z., A Flexible Solid-State Electrolyte for Wide-Scale Integration of Rechargeable Zinc–Air Batteries. *Energy & Environmental Science* **2016**, *9*, 663-670.

157. Ren, X.; Price, S. C.; Jackson, A. C.; Pomerantz, N.; Beyer, F. L., Highly Conductive Anion Exchange Membrane for High Power Density Fuel-Cell Performance. *ACS applied materials & interfaces* **2014**, *6*, 13330-13333.

158. Sequeira, C.; Santos, D., *Polymer Electrolytes: Fundamentals and Applications*. Elsevier: 2010.

159. Premchand, Y.; Di Vona, M.; Knauth, P., Proton-Conducting Nanocomposites and Hybrid Polymers. In *Nanocomposites;* Springer: 2008; pp 71-117.

160. Cooper, K., Characterizing through-Plane and in-Plane Ionic Conductivity of Polymer Electrolyte Membranes. *ECS Transactions* **2011**, *41*, 1371-1380.

161. Soboleva, T.; Xie, Z.; Shi, Z.; Tsang, E.; Navessin, T.; Holdcroft, S., Investigation of the through-Plane Impedance Technique for Evaluation of Anisotropy of Proton Conducting Polymer Membranes. *Journal of Electroanalytical Chemistry* **2008**, *622*, 145-152.

162. Xu, J. J.; Ye, H.; Huang, J., Novel Zinc Ion Conducting Polymer Gel Electrolytes Based on Ionic Liquids. *Electrochemistry communications* **2005**, *7*, 1309-1317.

163. Xu, Y.; Zhang, Y.; Guo, Z.; Ren, J.; Wang, Y.; Peng, H., Flexible, Stretchable, and Rechargeable Fiber - Shaped Zinc–Air Battery Based on Cross - Stacked Carbon Nanotube Sheets. *Angewandte Chemie International Edition* **2015**, *54*, 15390-15394.

164. Vassal, N.; Salmon, E.; Fauvarque, J.-F., Electrochemical Properties of an Alkaline Solid Polymer Electrolyte Based on P (Ech-Co-Eo). *Electrochimica Acta* **2000**, *45*, 1527-1532.

165. Stoller, M. D.; Ruoff, R. S., Best Practice Methods for Determining an Electrode Material's Performance for Ultracapacitors. *Energy & Environmental Science* **2010**, *3*, 1294-1301.

166. Wu, G.; Lin, S.; Yang, C., Preparation and Characterization of High Ionic Conducting Alkaline Non-Woven Membranes by Sulfonation. *Journal of membrane science* **2006**, *284*, 120-127.

167. Wu, G.; Lin, S.; Yang, C., Alkaline Zn-Air and Al-Air Cells Based on Novel Solid Pva/Paa Polymer Electrolyte Membranes. *Journal of Membrane Science* **2006**, *280*, 802-808.

168. Wu, G.; Lin, S.; You, J.; Yang, C., Study of High-Anionic Conducting Sulfonated Microporous Membranes for Zinc-Air Electrochemical Cells. *Materials Chemistry and Physics* **2008**, *112*, 798-804.

169. Zhang, J.; Fu, J.; Song, X.; Jiang, G.; Zarrin, H.; Xu, P.; Li, K.; Yu, A.; Chen, Z., Laminated Cross - Linked Nanocellulose/Graphene Oxide Electrolyte for Flexible Rechargeable Zinc–Air Batteries. *Advanced Energy Materials* **2016**, *6*, 1600476.

170. Huang, Y.-F.; Wu, P.-F.; Zhang, M.-Q.; Ruan, W.-H.; Giannelis, E. P., Boron Cross-Linked Graphene Oxide/Polyvinyl Alcohol Nanocomposite Gel Electrolyte for Flexible Solid-State Electric Double Layer Capacitor with High Performance. *Electrochimica Acta* **2014**, *132*, 103-111.

171. Jiang, M.; Zhu, J.; Chen, C.; Lu, Y.; Ge, Y.; Zhang, X., Poly (Vinyl Alcohol) Borate Gel Polymer Electrolytes Prepared by Electrodeposition and Their Application in Electrochemical Supercapacitors. *ACS applied materials & interfaces* **2016**, *8*, 3473-3481.

172. Xu, M.; Ivey, D.; Xie, Z.; Qu, W., Rechargeable Zn-Air Batteries: Progress in Electrolyte Development and Cell Configuration Advancement. *Journal of Power Sources* **2015**, *283*, 358-371.

173. Zhu, C.; Zhai, J.; Wen, D.; Dong, S., Graphene Oxide/Polypyrrole Nanocomposites: One-Step Electrochemical Doping, Coating and Synergistic Effect for Energy Storage. *J. Mater. Chem.* **2012**, *22*, 6300-6306.

174. Brisebois, P.; Siaj, M., Harvesting Graphene Oxide–Years 1859 to 2019: A Review of Its Structure, Synthesis, Properties and Exfoliation. *J. Mater. Chem.* **2020**, *8*, 1517-1547.

175. Staudenmaier, L., Verfahren Zur Darstellung Der Graphitsäure. *Ber. Dtsch. Chem. Ges.* **1898**, *31*, 1481-1487.

176. Hofmann, U.; König, E., Untersuchungen Über Graphitoxyd. *Z. Anorg. Allg. Chem.* **1937**, *234*, 311-336.

177. Dimiev, A. M.; Tour, J. M., Mechanism of Graphene Oxide Formation. *ACS Nano* **2014**, *8*, 3060-3068.

178. Shao, G.; Lu, Y.; Wu, F.; Yang, C.; Zeng, F.; Wu, Q., Graphene Oxide: The Mechanisms of Oxidation and Exfoliation. *J. Mater. Sci.* **2012**, *47*, 4400-4409.

179. Pan, S.; Aksay, I. A., Factors Controlling the Size of Graphene Oxide Sheets Produced Via the Graphite Oxide Route. *ACS Nano* **2011**, *5*, 4073-4083.

180. Wojtoniszak, M.; Mijowska, E., Controlled Oxidation of Graphite to Graphene Oxide with Novel Oxidants in a Bulk Scale. *J. Nanopart. Res.* **2012**, *14*, 1248.

181. Peng, L.; Xu, Z.; Liu, Z.; Wei, Y.; Sun, H.; Li, Z.; Zhao, X.; Gao, C., An Iron-Based Green Approach to 1-H Production of Single-Layer Graphene Oxide. *Nat. Commun.* **2015**, *6*, 1-9.

182. Yu, C.; Wang, C.-F.; Chen, S., Facile Access to Graphene Oxide from Ferro-Induced Oxidation. *Sci. Rep.* **2016**, *6*, 17071.

183. Ambrosi, A.; Pumera, M., Electrochemically Exfoliated Graphene and Graphene Oxide for Energy Storage and Electrochemistry Applications. *Chem. - Eur. J.* **2016**, *22*, 153-159.

184. Zhu, C.; Liu, L.; Fan, M.; Liu, L.; Dai, B.; Yang, J.; Sun, D., Microbial Oxidation of Graphite by Acidithiobacillus Ferrooxidans Cfmi-1. *RSC Adv.* **2014**, *4*, 55044-55047.

185. Liu, L.; Zhu, C.; Fan, M.; Chen, C.; Huang, Y.; Hao, Q.; Yang, J.; Wang, H.; Sun, D., Oxidation and Degradation of Graphitic Materials by Naphthalene-Degrading Bacteria. *Nanoscale* **2015**, *7*, 13619-13628.

186. Zhu, C.; Hao, Q.; Huang, Y.; Yang, J.; Sun, D., Microbial Oxidation of Dispersed Graphite by Nitrifying Bacteria 2011.2. *Nanoscale* **2013**, *5*, 8982-8985.

187. Joshi, R.; Carbone, P.; Wang, F.-C.; Kravets, V. G.; Su, Y.; Grigorieva, I. V.; Wu, H.; Geim, A. K.; Nair, R. R., Precise and Ultrafast Molecular Sieving through Graphene Oxide Membranes. *Science* **2014**, *343*, 752-754.

188. Li, H.; Song, Z.; Zhang, X.; Huang, Y.; Li, S.; Mao, Y.; Ploehn, H. J.; Bao, Y.; Yu, M., Ultrathin, Molecular-Sieving Graphene Oxide Membranes for Selective Hydrogen Separation. *Science* **2013**, *342*, 95-98.

189. Kim, H. W.; Yoon, H. W.; Yoon, S.-M.; Yoo, B. M.; Ahn, B. K.; Cho, Y. H.; Shin, H. J.; Yang, H.; Paik, U.; Kwon, S., Selective Gas Transport through Few-Layered Graphene and Graphene Oxide Membranes. *Science* **2013**, *342*, 91-95.

190. Chen, L.; Shi, G.; Shen, J.; Peng, B.; Zhang, B.; Wang, Y.; Bian, F.; Wang, J.; Li, D.; Qian, Z., Ion Sieving in Graphene Oxide Membranes Via Cationic Control of Interlayer Spacing. *Nature* **2017**.

191. Huang, H.; Song, Z.; Wei, N.; Shi, L.; Mao, Y.; Ying, Y.; Sun, L.; Xu, Z.; Peng, X., Ultrafast Viscous Water Flow through Nanostrand-Channelled Graphene Oxide Membranes. *Nat. Commun.* **2013**, *4*, 2979.

192. Abraham, J.; Vasu, K. S.; Williams, C. D.; Gopinadhan, K.; Su, Y.; Cherian, C. T.; Dix, J.; Prestat, E.; Haigh, S. J.; Grigorieva, I. V., Tunable Sieving of Ions Using Graphene Oxide Membranes. *Nat. Nanotechnol.* **2017**, *12*, 546.

193. Mi, B., Graphene Oxide Membranes for Ionic and Molecular Sieving. *Science* **2014**, *343*, 740-742.

194. Yang, Q.; Su, Y.; Chi, C.; Cherian, C.; Huang, K.; Kravets, V.; Wang, F.; Zhang, J.; Pratt, A.; Grigorenko, A., Ultrathin Graphene-Based Membrane with Precise Molecular Sieving and Ultrafast Solvent Permeation. *Nat. Mater.* **2017**, nmat5025.

195. Zhang, J.; Fu, J.; Song, X.; Jiang, G.; Zarrin, H.; Xu, P.; Li, K.; Yu, A.; Chen, Z., Laminated Cross - Linked Nanocellulose/Graphene Oxide Electrolyte for Flexible Rechargeable Zinc–Air Batteries. *Adv. Energy Mater.* **2016**, *6*.

196. Huang, J.-Q.; Zhuang, T.-Z.; Zhang, Q.; Peng, H.-J.; Chen, C.-M.; Wei, F., Permselective Graphene Oxide Membrane for Highly Stable and Anti-Self-Discharge Lithium–Sulfur Batteries. *ACS nano* **2015**, *9*, 3002-3011.

197. Dai, W.; Shen, Y.; Li, Z.; Yu, L.; Xi, J.; Qiu, X., Speek/Graphene Oxide Nanocomposite Membranes with Superior Cyclability for Highly Efficient Vanadium Redox Flow Battery. *J. Mater. Chem. A* **2014**, *2*, 12423-12432.

198. Veca, L. M.; Meziani, M. J.; Wang, W.; Wang, X.; Lu, F.; Zhang, P.; Lin, Y.; Fee, R.; Connell, J. W.; Sun, Y. P., Carbon Nanosheets for Polymeric Nanocomposites with High Thermal Conductivity. *Adv. Mater. (Weinheim, Ger.)* **2009**, *21*, 2088-2092.

199. Jung, I.; Dikin, D. A.; Piner, R. D.; Ruoff, R. S., Tunable Electrical Conductivity of Individual Graphene Oxide Sheets Reduced at "Low" Temperatures. *Nano Lett.* **2008**, *8*, 4283-4287.

200. Yousefi, N.; Gudarzi, M. M.; Zheng, Q.; Aboutalebi, S. H.; Sharif, F.; Kim, J.-K., Self-Alignment and High Electrical Conductivity of Ultralarge Graphene Oxide–Polyurethane Nanocomposites. *J. Mater. Chem.* **2012**, *22*, 12709-12717.

201. Willcox, J. A.; Kim, H. J., Molecular Dynamics Study of Water Flow across Multiple Layers of Pristine, Oxidized, and Mixed Regions of Graphene Oxide. *ACS Nano* **2017**, *11*, 2187-2193.

202. Boukhvalov, D. W.; Katsnelson, M. I.; Son, Y.-W., Origin of Anomalous Water Permeation through Graphene Oxide Membrane. *Nano Lett.* **2013**, *13*, 3930-3935.

203. Zheng, S.; Tu, Q.; Urban, J. J.; Li, S.; Mi, B., Swelling of Graphene Oxide Membranes in Aqueous Solution: Characterization of Interlayer Spacing and Insight into Water Transport Mechanisms. *ACS Nano* **2017**.

204. Tateishi, H.; Hatakeyama, K.; Ogata, C.; Gezuhara, K.; Kuroda, J.; Funatsu, A.; Koinuma, M.; Taniguchi, T.; Hayami, S.; Matsumoto, Y., Graphene Oxide Fuel Cell. *J. Electrochem. Soc.* **2013**, *160*, F1175-F1178.

205. Thimmappa, R.; Devendrachari, M. C.; Kottaichamy, A. R.; Tiwari, O.; Gaikwad, P.; Paswan, B.; Thotiyl, M. O., Stereochemistry-Dependent Proton Conduction in Proton Exchange Membrane Fuel Cells. *Langmuir* **2015**, *32*, 359-365.

206. Gautam, M.; Devendrachari, M. C.; Thimmappa, R.; Kottaichamy, A. R.; Shafi, S. P.; Gaikwad, P.; Kotresh, H. M. N.; Thotiyl, M. O., Polarity Governed Selective Amplification of through Plane Proton Shuttling in Proton Exchange Membrane Fuel Cells. *Phys. Chem. Chem. Phys.* **2017**, *19*, 7751-7759.

207. Gao, W.; Singh, N.; Song, L.; Liu, Z.; Reddy, A. L. M.; Ci, L.; Vajtai, R.; Zhang, Q.; Wei, B.; Ajayan, P. M., Direct Laser Writing of Micro-Supercapacitors on Hydrated Graphite Oxide Films. *Nature nanotechnology* **2011**, *6*, 496-500.

208. Borini, S.; White, R.; Wei, D.; Astley, M.; Haque, S.; Spigone, E.; Harris, N.; Kivioja, J.; Ryhanen, T., Ultrafast Graphene Oxide Humidity Sensors. *ACS nano* **2013**, *7*, 11166-11173.

209. Jiang, G.; Goledzinowski, M.; Comeau, F. J.; Zarrin, H.; Lui, G.; Lenos, J.; Veileux, A.; Liu, G.; Zhang, J.; Hemmati, S., Free - Standing Functionalized Graphene Oxide Solid Electrolytes in Electrochemical Gas Sensors. *Adv. Funct. Mater.* **2016**.

210. Zhang, J.; Jiang, G.; Goledzinowski, M.; Comeau, F. J.; Li, K.; Cumberland, T.; Lenos, J.; Xu, P.; Li, M.; Yu, A., Green Solid Electrolyte with Cofunctionalized Nanocellulose/Graphene Oxide Interpenetrating Network for Electrochemical Gas Sensors. *Small Methods* **2017**.

211. Jiang, G.; Goledzinowski, M.; Comeau, F. J.; Zarrin, H.; Lui, G.; Lenos, J.; Veileux, A.; Liu, G.; Zhang, J.; Hemmati, S., Free - Standing Functionalized Graphene Oxide Solid Electrolytes in Electrochemical Gas Sensors. *Advanced Functional Materials* **2016**, *26*, 1729-1736.

212. Chiu, Y.-D.; Wu, C.-W.; Chiang, C.-C., Tilted Fiber Bragg Grating Sensor with Graphene Oxide Coating for Humidity Sensing. *Sensors* **2017**, *17*, 2129.

213. Pandey, R. P.; Thakur, A. K.; Shahi, V. K., Sulfonated Polyimide/Acid-Functionalized Graphene Oxide Composite Polymer Electrolyte Membranes with Improved Proton Conductivity and Water-Retention Properties. *ACS Appl. Mater. Interfaces* **2014**, *6*, 16993-17002.

214. Fenton, H., Lxxiii.—Oxidation of Tartaric Acid in Presence of Iron. *Journal of the Chemical Society, Transactions* **1894**, *65*, 899-910.

215. Solís-Fernández, P.; Paredes, J.; Villar-Rodil, S.; Guardia, L.; Fernández-Merino, M.; Dobrik, G.; Biró, L.; Martínez-Alonso, A.; Tascón, J., Global and Local Oxidation Behavior of Reduced Graphene Oxide. *J. Phys. Chem. C* **2011**, *115*, 7956-7966.

216. Fischbein, M. D.; Drndić, M., Electron Beam Nanosculpting of Suspended Graphene Sheets. *Appl. Phys. Lett.* **2008**, *93*, 113107.

217. Bell, D. C.; Lemme, M. C.; Stern, L. A.; Williams, J. R.; Marcus, C. M., Precision Cutting and Patterning of Graphene with Helium Ions. *Nanotechnology* **2009**, *20*, 455301.

218. Solís-Fernández, P.; Paredes, J.; Villar-Rodil, S.; Guardia, L.; Fernández-Merino, M.; Dobrik, G.; Biró, L.; Martínez-Alonso, A.; Tascón, J., Global and Local Oxidation Behavior of Reduced Graphene Oxide. *J. Phys. Chem. C* **2011**, *115*, 7956-7966.

219. Koenig, S. P.; Wang, L.; Pellegrino, J.; Bunch, J. S., Selective Molecular Sieving through Porous Graphene. *Nat. Nanotechnol.* **2012**, *7*, 728-732.

220. Xu, Y.; Zhao, L.; Bai, H.; Hong, W.; Li, C.; Shi, G., Chemically Converted Graphene Induced Molecular Flattening of 5, 10, 15, 20-Tetrakis (1-Methyl-4-Pyridinio) Porphyrin and Its Application for Optical Detection of Cadmium (Ii) Ions. *Journal of the American Chemical Society* **2009**, *131*, 13490-13497.

221. Fatyeyeva, K.; Chappey, C.; Poncin-Epaillard, F.; Langevin, D.; Valleton, J.-M.; Marais, S., Composite Membranes Based on Nafion® and Plasma Treated Clay Charges: Elaboration and Water Sorption Investigations. *J. Membr. Sci.* **2011**, *369*, 155-166.

222. Follain, N. g.; Roualdes, S. p.; Marais, S. p.; Frugier, J. r. m.; Reinholdt, M.; Durand, J., Water Transport Properties of Plasma-Modified Commercial Anion-Exchange Membrane for Solid Alkaline Fuel Cells. *J. Phys. Chem. C* **2012**, *116*, 8510-8522.

223. Mecheri, B.; Felice, V.; Zhang, Z.; D'Epifanio, A.; Licoccia, S.; Tavares, A. C., Dsc and Dvs Investigation of Water Mobility in Nafion/Zeolite Composite Membranes for Fuel Cell Applications. *J. Phys. Chem. C* **2012**, *116*, 20820-20829.

224. Bokare, A. D.; Choi, W., Review of Iron-Free Fenton-Like Systems for Activating H 2 O 2 in Advanced Oxidation Processes. *J. Hazard. Mater.* **2014**, *275*, 121-135.

225. Bagal, M. V.; Gogate, P. R., Wastewater Treatment Using Hybrid Treatment Schemes Based on Cavitation and Fenton Chemistry: A Review. *Ultrason. Sonochem.* **2014**, *21*, 1-14.

226. Zhou, X.; Zhang, Y.; Wang, C.; Wu, X.; Yang, Y.; Zheng, B.; Wu, H.; Guo, S.; Zhang, J., Photo-Fenton Reaction of Graphene Oxide: A New Strategy to Prepare Graphene Quantum Dots for DNA Cleavage. *ACS Nano* **2012**, *6*, 6592-6599.

227. Li, W.; Bai, Y.; Zhang, Y.; Sun, M.; Cheng, R.; Xu, X.; Chen, Y.; Mo, Y., Effect of Hydroxyl Radical on the Structure of Multi-Walled Carbon Nanotubes. *Synthetic metals* **2005**, *155*, 509-515.

228. Bai, H.; Jiang, W.; Kotchey, G. P.; Saidi, W. A.; Bythell, B. J.; Jarvis, J. M.; Marshall, A. G.; Robinson, R. A.; Star, A., Insight into the Mechanism of Graphene Oxide Degradation Via the Photo-Fenton Reaction. *The Journal of Physical Chemistry C* **2014**, *118*, 10519-10529.

229. Mallet-Ladeira, P.; Puech, P.; Weisbecker, P.; Vignoles, G. L.; Monthioux, M., Behavior of Raman D Band for Pyrocarbons with Crystallite Size in the 2–5 Nm Range. *Appl. Phys. A: Mater. Sci. Process.* **2014**, *114*, 759-763.

230. Agmon, N., The Grotthuss Mechanism. *Chemical Physics Letters* **1995**, *244*, 456-462.

231. Kreuer, K. D.; Rabenau, A.; Weppner, W., Vehicle Mechanism, a New Model for the Interpretation of the Conductivity of Fast Proton Conductors. *Angew. Chem., Int. Ed. Engl.* **1982**, *21*, 208-209.

232. Paddison, S. J.; Paul, R.; Zawodzinski Jr, T. A., A Statistical Mechanical Model of Proton and Water Transport in a Proton Exchange Membrane. *J. Electrochem. Soc.* **2000**, *147*, 617.

233. Bayer, T.; Selyanchyn, R.; Fujikawa, S.; Sasaki, K.; Lyth, S. M., Spray-Painted Graphene Oxide Membrane Fuel Cells. *Journal of Membrane Science* **2017**, *541*, 347-357.

234. Tateishi, H.; Hatakeyama, K.; Ogata, C.; Gezuhara, K.; Kuroda, J.; Funatsu, A.; Koinuma, M.; Taniguchi, T.; Hayami, S.; Matsumoto, Y., Graphene Oxide Fuel Cell. *Journal of The Electrochemical Society* **2013**, *160*, F1175.

235. Park, G. S., Transport Principles-Solution, Diffusion and Permeation in Polymer Membranes. In *Synthetic Membranes: Science, Engineering and Applications;* P. M. Bungay, H. K. L., M. N. de Pinho, Eds.; Nato Asi Series Series C: Mathematical and Physical Sciences; Springer, Dordrecht: 1986; Vol. 181, pp 57-107.

236. Lian, B.; De Luca, S.; You, Y.; Alwarappan, S.; Yoshimura, M.; Sahajwalla, V.; Smith, S.; Leslie, G.; Joshi, R., Extraordinary Water Adsorption Characteristics of Graphene Oxide. *Chem. Sci.* **2018**, *9*, 5106-5111.

237. Medhekar, N. V.; Ramasubramaniam, A.; Ruoff, R. S.; Shenoy, V. B., Hydrogen Bond Networks in Graphene Oxide Composite Paper: Structure and Mechanical Properties. *ACS Nano* **2010**, *4*, 2300-2306.

238. Ban, S.; Xie, J.; Wang, Y.; Jing, B.; Liu, B.; Zhou, H., Insight into the Nanoscale Mechanism of Rapid H2o Transport within a Graphene Oxide Membrane: Impact of Oxygen Functional Group Clustering. *ACS Appl. Mater. Interfaces* **2015**, *8*, 321-332.

239. Ri, G.-C.; Kim, J.-S.; Yu, C.-J., Role of Water Molecules in Enhancing the Proton Conductivity on Reduced Graphene Oxide under High Humidity. *Phys. Rev. Appl.* **2018**, *10*, 034018.

240. Achtyl, J. L.; Unocic, R. R.; Xu, L.; Cai, Y.; Raju, M.; Zhang, W.; Sacci, R. L.; Vlassiouk, I. V.; Fulvio, P. F.; Ganesh, P., Aqueous Proton Transfer across Single-Layer Graphene. *Nature communications* **2015**, *6*, 1-7.

241. Ma, J.; Ping, D.; Dong, X., Recent Developments of Graphene Oxide-Based Membranes: A Review. *Membranes* **2017**, *7*, 52.

242. Wondimkun, Z. T.; Beyene, T. T.; Weret, M. A.; Sahalie, N. A.; Huang, C.-J.; Thirumalraj, B.; Jote, B. A.; Wang, D.; Su, W.-N.; Wang, C.-H., Binder-Free Ultra-Thin Graphene Oxide as an Artificial Solid

Electrolyte Interphase for Anode-Free Rechargeable Lithium Metal Batteries. *Journal of Power Sources* **2020**, *450*, 227589.

243. Wu, W.; Shi, Y.; Liu, G.; Fan, X.; Yu, Y., Recent Development of Graphene Oxide Based Forward Osmosis Membrane for Water Treatment: A Critical Review. *Desalination* **2020**, *491*, 114452.

244. Baskakov, S.; Baskakova, Y.; Lyskov, N.; Dremova, N.; Irzhak, A.; Kumar, Y.; Michtchenok, A.; Shulga, Y., Fabrication of Current Collector Using a Composite of Polylactic Acid and Carbon Nano-Material for Metal-Free Supercapacitors with Graphene Oxide Separators and Microwave Exfoliated Graphite Oxide Electrodes. *Electrochimica Acta* **2018**, *260*, 557-563.

245. Aziz, M. A.; Oh, K.; Shanmugam, S., A Sulfonated Poly (Arylene Ether Ketone)/Polyoxometalate–Graphene Oxide Composite: A Highly Ion Selective Membrane for All Vanadium Redox Flow Batteries. *Chemical Communications* **2017**, *53*, 917-920.

246. Park, S. H.; Lee, T. H.; Lee, Y. J.; Park, H. B.; Lee, Y. J., Graphene Oxide Sieving Membrane for Improved Cycle Life in High - Efficiency Redox - Mediated Li–O2 Batteries. *Small* **2018**, *14*, 1801456.

247. Lee, D. K.; Kim, S. J.; Kim, Y. J.; Choi, H.; Kim, D. W.; Jeon, H. J.; Ahn, C. W.; Lee, J. W.; Jung, H. T., Graphene Oxide/Carbon Nanotube Bilayer Flexible Membrane for High - Performance Li–S Batteries with Superior Physical and Electrochemical Properties. *Advanced Materials Interfaces* **2019**, *6*, 1801992.

248. Zheng, L.; Wang, H.; Niu, R.; Zhang, Y.; Shi, H., Sulfonated Poly (Ether Ether Ketone)/Sulfonated Graphene Oxide Hybrid Membrane for Vanadium Redox Flow Battery. *Electrochimica Acta* **2018**, *282*, 437-447.

249. Zhang, Y.; Wang, H.; Liu, B.; Shi, J.; Zhang, J.; Shi, H., An Ultra-High Ion Selective Hybrid Proton Exchange Membrane Incorporated with Zwitterion-Decorated Graphene Oxide for Vanadium Redox Flow Batteries. *Journal of Materials Chemistry A* **2019**, *7*, 12669-12680.

250. Wang, D.; Xu, F.; Hu, J.; Lin, M., Phytic Acid/Graphene Oxide Nanocomposites Modified Electrode for Electrochemical Sensing of Dopamine. *Materials Science and Engineering: C* **2017**, *71*, 1086-1089.

251. Jin, L.; Wang, Z.; Zheng, S.; Mi, B., Polyamide-Crosslinked Graphene Oxide Membrane for Forward Osmosis. *Journal of Membrane Science* **2018**, *545*, 11-18.

252. Zhang, M.; Guan, K.; Ji, Y.; Liu, G.; Jin, W.; Xu, N., Controllable Ion Transport by Surface-Charged Graphene Oxide Membrane. *Nature communications* **2019**, *10*, 1-8.

253. Huang, K.; Liu, G.; Lou, Y.; Dong, Z.; Shen, J.; Jin, W., A Graphene Oxide Membrane with Highly Selective Molecular Separation of Aqueous Organic Solution. *Angewandte Chemie* **2014**, *126*, 7049-7052.

254. Liu, T.; Liu, X.; Graham, N.; Yu, W.; Sun, K., Two-Dimensional Mxene Incorporated Graphene Oxide Composite Membrane with Enhanced Water Purification Performance. *Journal of Membrane Science* **2020**, *593*, 117431.

255. Liu, H.; Liu, X.; Zhao, F.; Liu, Y.; Liu, L.; Wang, L.; Geng, C.; Huang, P., Preparation of a Hydrophilic and Antibacterial Dual Function Ultrafiltration Membrane with Quaternized Graphene Oxide as a Modifier. *Journal of Colloid and Interface Science* **2020**, *562*, 182-192.

256. Lv, X.-B.; Xie, R.; Ji, J.-Y.; Liu, Z.; Wen, X.-Y.; Liu, L.-Y.; Hu, J.-Q.; Ju, X.-J.; Wang, W.; Chu, L.-Y., A Novel Strategy to Fabricate Cation-Cross-Linked Graphene Oxide Membrane with High Aqueous Stability and High Separation Performance. *ACS Applied Materials & Interfaces* **2020**.

257. Lim, M.-Y.; Choi, Y.-S.; Kim, J.; Kim, K.; Shin, H.; Kim, J.-J.; Shin, D. M.; Lee, J.-C., Cross-Linked Graphene Oxide Membrane Having High Ion Selectivity and Antibacterial Activity Prepared Using Tannic Acid-Functionalized Graphene Oxide and Polyethyleneimine. *Journal of Membrane Science* **2017**, *521*, 1-9.

258. Ying, W.; Cai, J.; Zhou, K.; Chen, D.; Ying, Y.; Guo, Y.; Kong, X.; Xu, Z.; Peng, X., Ionic Liquid Selectively Facilitates Co2 Transport through Graphene Oxide Membrane. *ACS nano* **2018**, *12*, 5385-5393.

259. Cheng, L.; Guan, K.; Liu, G.; Jin, W., Cysteamine-Crosslinked Graphene Oxide Membrane with Enhanced Hydrogen Separation Property. *Journal of Membrane Science* **2020**, *595*, 117568.

260. Liu, S.; Zeng, T. H.; Hofmann, M.; Burcombe, E.; Wei, J.; Jiang, R.; Kong, J.; Chen, Y., Antibacterial Activity of Graphite, Graphite Oxide, Graphene Oxide, and Reduced Graphene Oxide: Membrane and Oxidative Stress. *ACS nano* **2011**, *5*, 6971-6980.

261. Meguro, R.; Ishitobi, H.; Suto, R.; Mitsuyoshi, T.; Uehara, K.; Otsuka, Y.; Nakagawa, N., Study of Deep Oxidation and Sulfonation of Graphene Oxide as Low-Temperature Fuel Cell Electrolyte. *International Journal of Hydrogen Energy* **2020**.

262. Sy, S.; Jiang, G.; Zhang, J.; Zarrin, H.; Cumberland, T.; Abureden, S.; Bell, E.; Gostick, J.; Yu, A.; Chen, Z., A near-Isotropic Proton-Conducting Porous Graphene Oxide Membrane. *ACS nano* **2020**, *14*, 14947-14959.

263. Cai, Y.; Yue, Z.; Teng, X.; Xu, S., Phosphoric Acid Doped Crosslinked Polybenzimidazole/Modified Graphene Oxide Composite Membranes for High Temperature Proton Exchange Membrane Applications. *Journal of The Electrochemical Society* **2018**, *165*, F914.

264. Zhang, N.; Wang, B.; Zhang, Y.; Bu, F.; Cui, Y.; Li, X.; Zhao, C.; Na, H., Mechanically Reinforced Phosphoric Acid Doped Quaternized Poly (Ether Ether Ketone) Membranes Via Cross-Linking with Functionalized Graphene Oxide. *Chemical Communications* **2014**, *50*, 15381-15384.

265. Wang, H.; Sun, N.; Xu, X.; Wang, S.; Kang, W.; Zhuang, X.; Yin, Y.; Cheng, B., Adenosine Triphosphate@ Graphene Oxide Proton Channels for Proton Exchange Membranes Constructed Via Electrostatic Layer-by-Layer Deposition. *Journal of Membrane Science* **2020**, 118880.

266. Yang, P.; Wu, H.; Khan, N. A.; Shi, B.; He, X.; Cao, L.; Mao, X.; Zhao, R.; Qiu, M.; Jiang, Z., Intrinsic Proton Conductive Deoxyribonucleic Acid (DNA) Intercalated Graphene Oxide Membrane for High-Efficiency Proton Conduction. *Journal of Membrane Science* **2020**, 118136.

267. Maiti, J.; Kakati, N.; Woo, S. P.; Yoon, Y. S., Nafion® Based Hybrid Composite Membrane Containing Go and Dihydrogen Phosphate Functionalized Ionic Liquid for High Temperature Polymer Electrolyte Membrane Fuel Cell. *Composites Science and Technology* **2018**, *155*, 189-196.

268. Liu, Y.; Wang, J.; Zhang, H.; Ma, C.; Liu, J.; Cao, S.; Zhang, X., Enhancement of Proton Conductivity of Chitosan Membrane Enabled by Sulfonated Graphene Oxide under Both Hydrated and Anhydrous Conditions. *Journal of Power Sources* **2014**, *269*, 898-911.

269. Hatakeyama, K.; Islam, M. S.; Michio, K.; Ogata, C.; Taniguchi, T.; Funatsu, A.; Kida, T.; Hayami, S.; Matsumoto, Y., Super Proton/Electron Mixed Conduction in Graphene Oxide Hybrids by Intercalating Sulfate Ions. *Journal of Materials Chemistry A* **2015**, *3*, 20892-20895.

270. Jiang, Z.; Shi, Y.; Jiang, Z.-J.; Tian, X.; Luo, L.; Chen, W., High Performance of a Free-Standing Sulfonic Acid Functionalized Holey Graphene Oxide Paper as a Proton Conducting Polymer Electrolyte for Air-Breathing Direct Methanol Fuel Cells. *Journal of Materials Chemistry A* **2014**, *2*, 6494-6503.

271. Li, Z.; He, G.; Zhang, B.; Cao, Y.; Wu, H.; Jiang, Z.; Tiantian, Z., Enhanced Proton Conductivity of Nafion Hybrid Membrane under Different Humidities by Incorporating Metal–Organic Frameworks with High Phytic Acid Loading. *ACS applied materials & interfaces* **2014**, *6*, 9799-9807.

272. Vilčiauskas, L.; Tuckerman, M. E.; Bester, G.; Paddison, S. J.; Kreuer, K.-D., The Mechanism of Proton Conduction in Phosphoric Acid. *Nature chemistry* **2012**, *4*, 461-466.

273. Araya, S. S.; Zhou, F.; Liso, V.; Sahlin, S. L.; Vang, J. R.; Thomas, S.; Gao, X.; Jeppesen, C.; Kær, S. K., A Comprehensive Review of Pbi-Based High Temperature Pem Fuel Cells. *International Journal of Hydrogen Energy* **2016**, *41*, 21310-21344.

274. Kim, H. J.; Talukdar, K.; Choi, S.-J., Tuning of Nafion® by Hkust-1 as Coordination Network to Enhance Proton Conductivity for Fuel Cell Applications. *Journal of Nanoparticle Research* **2016**, *18*, 47.

275. Zhang, C.; Zhang, L.; Zhou, W.; Wang, Y.; Chan, S. H., Investigation of Water Transport and Its Effect on Performance of High-Temperature Pem Fuel Cells. *Electrochimica Acta* **2014**, *149*, 271-277.

276. He, R.; Li, Q.; Xiao, G.; Bjerrum, N. J., Proton Conductivity of Phosphoric Acid Doped Polybenzimidazole and Its Composites with Inorganic Proton Conductors. *Journal of Membrane Science* **2003**, *226*, 169-184.

277. Escorihuela, J.; Narducci, R.; Compañ, V.; Costantino, F., Proton Conductivity of Composite Polyelectrolyte Membranes with Metal - Organic Frameworks for Fuel Cell Applications. *Advanced Materials Interfaces* **2019**, *6*, 1801146.

278. Zhao, M.-Y.; Wang, Y.-D.; Cheng, D.; Liu, B.-L.; Wang, Y.-H.; Zang, H.-Y., A Highly Proton Conductive Membrane Based on Hydrolyzed Nbcl5 and Phytic Acid. *International Journal of Hydrogen Energy* **2020**.

279. Tang, F.; Wang, X.; Xu, X.; Li, L., Phytic Acid Doped Nanoparticles for Green Anticorrosion Coatings. *Colloids and Surfaces A: Physicochemical and engineering aspects* **2010**, *369*, 101-105.

280. Mao, X.; Cao, Z.; Chen, S.; Jia, J.; Li, X.; Yin, Y.; Yang, S., Facile Synthesis of N, P-Doped Hierarchical Porous Carbon Framework Catalysts Based on Gelatin/Phytic Acid Supermolecules for Electrocatalytic Oxygen Reduction. *International Journal of Hydrogen Energy* **2019**, *44*, 5890-5898.

281. Lehrfeld, J., Cation Exchange Resins Prepared from Phytic Acid. *Journal of applied polymer science* **1997**, *66*, 491-497.

282. Cai, K.; Sun, F.; Liang, X.; Liu, C.; Zhao, N.; Zou, X.; Zhu, G., An Acid-Stable Hexaphosphate Ester Based Metal–Organic Framework and Its Polymer Composite as Proton Exchange Membrane. *Journal of Materials Chemistry A* **2017**, *5*, 12943-12950.

283. Kouhestania, F.; Torangib, M. A.; Motavalizadehkakhkya, A.; Karazhyanc, R.; Zhianid, R., Enhancement Strategy of Polyethersulfone (Pes) Membrane by Introducing Pluronic F127/Graphene

Oxide and Phytic Acid/Graphene Oxide Blended Additives: Preparation, Characterization and Wastewater Filtration Assessment. *DESALINATION AND WATER TREATMENT* **2019**, *171*, 44-56.

284. Tanaka, M.; Takeda, Y.; Wakiya, T.; Wakamoto, Y.; Harigaya, K.; Ito, T.; Tarao, T.; Kawakami, H., Acid-Doped Polymer Nanofiber Framework: Three-Dimensional Proton Conductive Network for High-Performance Fuel Cells. *Journal of Power Sources* **2017**, *342*, 125-134.

285. Li, J.; Li, Y.; Song, Y.; Niu, S.; Li, N., Ultrasonic-Assisted Synthesis of Polyvinyl Alcohol/Phytic Acid Polymer Film and Its Thermal Stability, Mechanical Properties and Surface Resistivity. *Ultrasonics Sonochemistry* **2017**, *39*, 853-862.

286. Graf, E., Applications of Phytic Acid. *Journal of the American Oil Chemists' Society* **1983**, *60*, 1861-1867.

287. Graf, E.; Mahoney, J. R.; Bryant, R. G.; Eaton, J. W., Iron-Catalyzed Hydroxyl Radical Formation. Stringent Requirement for Free Iron Coordination Site. *Journal of Biological Chemistry* **1984**, *259*, 3620-3624.

288. Schlemmer, U.; Frølich, W.; Prieto, R. M.; Grases, F., Phytate in Foods and Significance for Humans: Food Sources, Intake, Processing, Bioavailability, Protective Role and Analysis. *Molecular nutrition & food research* **2009**, *53*, S330-S375.

289. Zhao, F.; Cheng, H.; Zhang, Z.; Jiang, L.; Qu, L., Direct Power Generation from a Graphene Oxide Film under Moisture. *Advanced Materials* **2015**, *27*, 4351-4357.

290. Zhou, X.; Huang, H.; Zhu, R.; Chen, R.; Sheng, X.; Xie, D.; Mei, Y., Green Modification of Graphene Oxide with Phytic Acid and Its Application in Anticorrosive Water-Borne Epoxy Coatings. *Progress in Organic Coatings* **2020**, *143*, 105601.

291. Dai, H.; Wang, N.; Wang, D.; Ma, H.; Lin, M., An Electrochemical Sensor Based on Phytic Acid Functionalized Polypyrrole/Graphene Oxide Nanocomposites for Simultaneous Determination of Cd (Ii) and Pb (Ii). *Chemical Engineering Journal* **2016**, *299*, 150-155.

292. Zhao, Q.; Zhang, Y.; Meng, Y.; Wang, Y.; Ou, J.; Guo, Y.; Xiao, D., Phytic Acid Derived Lifepo4 Beyond Theoretical Capacity as High-Energy Density Cathode for Lithium Ion Battery. *Nano Energy* **2017**, *34*, 408-420.

293. Song, X.; Chen, Y.; Rong, M.; Xie, Z.; Zhao, T.; Wang, Y.; Chen, X.; Wolfbeis, O. S., A Phytic Acid Induced Super - Amphiphilic Multifunctional 3d Graphene - Based Foam. *Angewandte Chemie International Edition* **2016**, *55*, 3936-3941.

294. Dimiev, A. M.; Alemany, L. B.; Tour, J. M., Graphene Oxide. Origin of Acidity, Its Instability in Water, and a New Dynamic Structural Model. *ACS nano* **2013**, *7*, 576-588.

295. Zhang, J.; Jiang, G.; Goledzinowski, M.; Comeau, F. J.; Li, K.; Cumberland, T.; Lenos, J.; Xu, P.; Li, M.; Yu, A., Green Solid Electrolyte with Cofunctionalized Nanocellulose/Graphene Oxide Interpenetrating Network for Electrochemical Gas Sensors. *Small Methods* **2017**, *1*, 1700237.

296. Ma, G.; Huang, K.; Ma, J.-S.; Ju, Z.; Xing, Z.; Zhuang, Q.-c., Phosphorus and Oxygen Dual-Doped Graphene as Superior Anode Material for Room-Temperature Potassium-Ion Batteries. *Journal of Materials Chemistry A* **2017**, *5*, 7854-7861.

297. Patil, P. N.; Roilo, D.; Brusa, R. S.; Miotello, A.; Checchetto, R., Influence of Nano-Level Molecular Packing on the Gas Transport Properties in Amine-Modified Epoxy Resins. *Polymer* **2015**, *58*, 130-138.

298. Cheng, L.; Wu, W.; Meng, W.; Xu, S.; Han, H.; Yu, Y.; Qu, H.; Xu, J., Application of Metallic Phytates to Poly (Vinyl Chloride) as Efficient Biobased Phosphorous Flame Retardants. *Journal of Applied Polymer Science* **2018**, *135*, 46601.

299. Onem, H.; Nadaroglu, H., Immobilization of Purified Phytase Enzyme from Tirmit (Lactarius Volemus) on Coated Chitosan with Iron Nanoparticles and Investigation of Its Usability in Cereal Industry. *Iranian Journal of Science and Technology, Transactions A: Science* **2018**, *42*, 1063-1075.

300. Jiang, G.; Qiao, J.; Hong, F., Application of Phosphoric Acid and Phytic Acid-Doped Bacterial Cellulose as Novel Proton-Conducting Membranes to Pemfc. *international journal of hydrogen energy* **2012**, *37*, 9182-9192.

301. Gao, X.; Zhao, C.; Lu, H.; Gao, F.; Ma, H., Influence of Phytic Acid on the Corrosion Behavior of Iron under Acidic and Neutral Conditions. *Electrochimica Acta* **2014**, *150*, 188-196.

302. Fan, X.; Xu, H.; Zuo, S.; Liang, Z.; Yang, S.; Chen, Y., Preparation and Supercapacitive Properties of Phosphorus-Doped Reduced Graphene Oxide Hydrogel. *Electrochimica Acta* **2020**, *330*, 135207.

303. Liu, R.; Zhang, G.; Cao, H.; Zhang, S.; Xie, Y.; Haider, A.; Kortz, U.; Chen, B.; Dalal, N. S.; Zhao, Y., Enhanced Proton and Electron Reservoir Abilities of Polyoxometalate Grafted on Graphene for High-Performance Hydrogen Evolution. *Energy & Environmental Science* **2016**, *9*, 1012-1023.

304. Yi, Y.; Wang, P.; Fan, G.; Wang, Z.; Chen, S.; Xue, T.; Wen, Y., Hierarchically Porous Carbon Microsphere Doped with Phosphorus as a High Conductive Electrocatalyst for Oxidase-Like Sensors and Supercapacitors. *ACS Sustainable Chemistry & Engineering* **2020**, *8*, 9937-9946.

305. García-Mateos, F.; Berenguer, R.; Valero-Romero, M.; Rodríguez-Mirasol, J.; Cordero, T., Phosphorus Functionalization for the Rapid Preparation of Highly Nanoporous Submicron-Diameter Carbon Fibers by Electrospinning of Lignin Solutions. *Journal of Materials Chemistry A* **2018**, *6*, 1219-1233.

306. Cai, Y.; Wu, C.; Liu, Z.; Zhang, L.; Chen, L.; Wang, J.; Wang, X.; Yang, S.; Wang, S., Fabrication of a Phosphorylated Graphene Oxide–Chitosan Composite for Highly Effective and Selective Capture of U (Vi). *Environmental Science: Nano* **2017**, *4*, 1876-1886.

307. Wang, C.; Zhou, Y.; Sun, L.; Wan, P.; Zhang, X.; Qiu, J., Sustainable Synthesis of Phosphorus-and Nitrogen-Co-Doped Porous Carbons with Tunable Surface Properties for Supercapacitors. *Journal of Power Sources* **2013**, *239*, 81-88.

308. Liu, Y.; Zhu, Y.; Shen, J.; Huang, J.; Yang, X.; Li, C., Cop Nanoparticles Anchored on N, P-Dual-Doped Graphene-Like Carbon as a Catalyst for Water Splitting in Non-Acidic Media. *Nanoscale* **2018**, *10*, 2603-2612.

309. Shimizu, M.; Tsushima, Y.; Arai, S., Electrochemical Na-Insertion/Extraction Property of Ni-Coated Black Phosphorus Prepared by an Electroless Deposition Method. *ACS omega* **2017**, *2*, 4306-4315.

310. Kreuer, K. D.; Rabenau, A.; Weppner, W., Vehicle Mechanism, a New Model for the Interpretation of the Conductivity of Fast Proton Conductors. *Angewandte Chemie International Edition in English* **1982**, *21*, 208-209.